3-22-2019

A Focal Plane Array and Electronics Model for CMOS and CCD Sensors in the AFIT Sensor and Scene Emulation Tool (ASSET)

Fernando D. Fernandez

A FOCAL PLANE ARRAY AND ELECTRONICS MODEL FOR CMOS AND CCD SENSORS IN THE AFIT SENSOR AND SCENE EMULATION TOOL (ASSET)

THESIS

Fernando D. Fernandez, Civilian, USAF

AFIT-ENG-MS-19-M-026

DEPARTMENT OF THE AIR FORCE
AIR UNIVERSITY

AIR FORCE INSTITUTE OF TECHNOLOGY

Wright-Patterson Air Force Base, Ohio

AFIT-ENG-MS-19-M-026

A FOCAL PLANE ARRAY AND ELECTRONICS MODEL FOR CMOS AND CCD SENSORS IN THE AFIT SENSOR AND SCENE EMULATION TOOL (ASSET)

THESIS

Presented to the Faculty

Department of Electrical and Computer Engineering

Graduate School of Engineering and Management

Air Force Institute of Technology

Air University

Air Education and Training Command

In Partial Fulfillment of the Requirements for the

Degree of Master of Science in Electrical Engineering

Fernando D. Fernandez, B.S., B.A.

Civilian, USAF

March 2019

AFIT-ENG-MS-19-M-026

A FOCAL PLANE ARRAY AND ELECTRONICS MODEL FOR CMOS AND CCD SENSORS IN THE AFIT SENSOR AND SCENE EMULATION TOOL (ASSET)

Fernando D. Fernandez, B.S., B.A.

Civilian, USAF

Committee Membership:

Dr. B. J. Steward
Chair

Dr. K. C. Gross
Member

Dr. S. C. Cain
Member

Abstract

Electro-optical and infrared (EO/IR) sensor models are useful tools that can facilitate understanding a system's behavior without expensive and time-consuming testing of an actual system. EO/IR models are especially important to the military industry where truth data is required but is sometimes impractical to obtain through experimentation due to expense or difficulties in procuring hardware. This work describes implementation of a focal plane array (FPA) model of charge-coupled device (CCD) and complementary metal-oxide semiconductor (CMOS) photodetectors as a component in the Air Force Institute of Technology (AFIT) Sensor and Scene Emulation Tool (ASSET). The FPA model covers conversion of photo-generated electrons to voltage and then to digital numbers. It incorporates sense node, source follower, and analog-to-digital converter (ADC) components contributing to gain non-linearities and includes noise sources associated with the detector and electronics such as shot, thermal, 1/f, and quantization noise. This thesis describes the higher fidelity FPA and electronics model recently incorporated into ASSET, and it also details validation of the improved model using EO/IR imager data collected with laboratory measurements. The result is an improved model capable of generating realistic synthetic data representative of a wide range of systems for use in new algorithm development and data exploitation techniques supporting a broad community of academic, commercial, and military researchers.

Acknowledgments

To my parents I am particularly grateful for the many years of support and encouragement which have led me to where I am today. I wish to express my deep appreciation to my advisor, Dr. Bryan Steward, who provided the opportunity to continue my education, for his support and guidance that kept me pushing towards the goal, and for the countless hours he put into mentoring and working with me on my research goals. Special thanks go out to my committee members, Dr. Kevin Gross and Dr. Stephen Cain, for all their guidance and support in this research as well as my academic program. I would also like to thank my flight chief, Mark Bellott, and my team members, Charles Watson and Justin McCarthy, for their support and encouragement throughout my academic program. Finally, I would like to thank, Dr. Michael Hawks, Dr. Andrew Kondrath and Dr. Jay Patel, for their technical support.

This research was sponsored by the Space and Missile Systems Center, Remote Sensing Exploitation Division (SMC/RSX) and the National Air and Space Intelligence Center, Ballistic Missile Analysis Squadron (NASIC/SMB). I am grateful to both organizations for their support and collaboration.

Fernando D. Fernandez

Table of Contents

List of Figures

Page

List of Tables

Page

A FOCAL PLANE ARRAY AND ELECTRONICS MODEL FOR CMOS AND CCD SENSORS IN THE AFIT SENSOR AND SCENE EMULATION TOOL (ASSET)

1 Introduction

Advances in solid-state technology have increased image quality in recent years. Reductions in photodetector (also called *detector* interchangeably in this thesis) sizes have enabled an increase in the number of elements in a pixel array of constant area, allowing proportional increases in the resolution of the system [1]. However, this decrease in pixel size has also reduced the collection area available to convert incident photons to photoelectron signal, which often results in a reduced signal to noise ratio (SNR). This makes it increasingly difficult to sense dim signals or distinguish radiometric characteristics from noise [1, 2]. New and better algorithms for signal processing are one way to compensate for the potential loss in sensitivity and noise performance [3].

The AFIT Sensor and Scene Emulation Tool (ASSET) was created to produce synthetic data representative of real electro-optic and infrared (EO/IR) sensors [4]. Its development was driven by the need for realistic data under controlled conditions without the expense of conducting field or laboratory experiments. ASSET can produce data suitable for signal processing and algorithm development for both real and hypothetical systems by accurately modeling scene and sensor characteristics. The latter is especially important, as military researchers increasingly use modeling for assessing theoretical system performance to keep pace with sensor technology development, without the need to build an entire sensor system. This thesis describes the implementation of a focal plane

array (FPA) and electronics model for CCD and CMOS EO/IR photodetectors as a component of ASSET.

1.1 Problem Statement

Many modern image sensors use charge-coupled device (CCD) or complementary metal-oxide semiconductor (CMOS) solid-state photosensors to convert light into a digital signal. Due to imperfections of photosensors, such a conversion is not ideal and leads to noise in the measured signal. Therefore, one can either estimate and reduce the impact of noise from the image sensor, or simulate and predict what the performance of a given sensor will be in terms of image appearance, given the device specifications and key design parameters.

The high-level simulation of noise in photosensors, however, is still an area of active research. The main problem is that photosensors are affected by many different sources of noise, some of which cannot be modeled effectively using only Gaussian noise. The growing use of new pixel architectures, especially staring focal plane array (FPA) technology, introduces new parameters affecting system performance that are not adequately addressed by current models (e.g. offset FPN due to pixel's transistors). There is a need of high-level image sensor system modeling tools that allow engineers to see realistic visual effects of noise where the user can change individual design or process parameters to quickly see the resulting effects on image quality. This work attempts to address the issue of the lack of high-level photosensor modeling tools that enable the user to simulate realistic effects of noise on CCD and CMOS image sensors.

This effort describes the higher fidelity modeling of the FPA behavior recently added to ASSET, expanding on Konnik's [5] and Willers' [6] work which are partly based on the *Photon Transfer* model described by Janesick [7]. It also details validation of the improved model using FPA data collected in laboratory measurements, including examples from a high-speed Phantom v12.1 camera to demonstrate ASSET's ability to emulate real sensors.

The improved FPA and electronics model was implemented in MATLAB as part of the baseline ASSET model and improves the detector response and read-out electronics by (1) replacing the baseline linear conversion gain from electrons to counts with an electronics component-based model that emulates the physics of CMOS and CCD pixels; (2) including non-linear effects observed in real sensors such as change in capacitance with signal level and gains associated with each electrical component; (3) implementing fixed-pattern noise (FPN) based on FPA architecture (e.g. discrete number of ADCs, column level amplifier, etc.) to replace baseline random model.

The FPA model covers conversion of photo-generated electrons to voltage (or current) and finally to digital numbers. It incorporates sense node and source follower components contributing to gain non-linearities. It also includes noise sources associated with the detector and electronics such as shot, thermal, 1/f, reset, fixed-pattern, and quantization noise. The model aims to provide realistic noise characteristics and sensor artifacts to predict the performance of real imaging systems for given device specifications and design parameters. The additional input sensor information provided to ASSET gives the user full control over sensor FPA and electronics characteristics.

1.2 Overview

The remainder of this thesis is outlined as follows. Chapter 2 discusses the physics basis of the ASSET model, including a description of the approximations used for the detector and read-out circuitry in the original model. Chapter 3 presents the theoretical background on CCD and CMOS image sensors that are the basis of the improved model, discussing the basics of photodetection, CCD and CMOS photodiodes, and their respective pixel architectures. Furthermore, a description of the end-to-end process of modeling the image sensor from photon irradiance at the detector to electrons, voltage, and then digital numbers is discussed. Chapter 4 presents the laboratory experiments conducted using the Phantom camera, describes configuration of the ASSET model used to generate synthetic test data for validation against measured CMOS data, and discusses the process of generating a photon transfer curve (PTC) and a dark transfer curve (DTC) that are used to analyze the results. Chapter 5 compares the performance of ASSET with the improved FPA model to data collected in the laboratory measurements, and the validation results are analyzed.

2 ASSET

This chapter provides an overview of ASSET, including a description of the approximations used for the detector and read-out circuitry. The model described here is that of the baseline ASSET model (sometimes referred to as *baseline* for brevity) only and does not include the improvements implemented as part of this thesis; these enhancements are discussed in Chapter 3. Because ASSET includes physics spanning the generation of scene radiance, atmospheric radiation transfer, effects of the optical system and detector array, and ultimate conversion of scene signal to digital units; it is not practical to provide a detailed description of the ASSET model. Instead, an overview is given that is sufficient for understanding the end-to-end process of photons to digitized signal data, and a more through description can be found in the Appendix and citations.

2.1 ASSET Overview

Currently available high-fidelity modeling tools are generally intended for small fields of view (FOV) [4, 8]. Even though some simulators may be used to cover larger areas (e.g. wide FOV, WFOV), they can become computationally expensive. ASSET was designed to emulate sensor response to at-aperture irradiance, generate synthetic EO/IR sensor data suitable for algorithm development and testing, and to allow investigation of sensor configurations in a way that is computationally efficient and easily accessible to the user. Therefore, ASSET generates synthetic data sets with realistic radiometric, noise, and sensor properties representative of a broad range of scenes and sensors operating in the visible through thermal infrared wavelengths.

ASSET is a physics-based, image-chain model [4]. The principal inputs include a *source image* and a *configuration file*. The latter contains all parameters necessary to specify characteristics of the sensor (e.g. wavelength band, integration time, instantaneous field of view, etc.) and scene (e.g. solar geometry, atmospheric model, etc.) that define a scenario as well as tuning of model fidelity versus computational speed. The source image (uncalibrated or calibrated imagery, certain types of video files, or MATLAB arrays) represents the scene viewed by a sensor and is used to generate photon radiance at the sensor's aperture by: (1) directly specifying scene radiance, (2) applying calibration metadata, or (3) calculating apparent radiance from scene reflectivity and emissivity coupled with solar geometry and atmospheric conditions. In both (1) and (3) the source image is treated as a texture map that is scaled to radiance, reflectivity, or emissivity bounds.

At-aperture irradiance is propagated through the sensor in a series of steps that emulate blurring by the optical system's point spread function (PSF), attenuation by optical and filter components, and addition of radiance contributed from thermal emissions by the sensor itself (called *self-emission*). The model includes appropriate sensor and atmospheric response data for operation in the visible and infrared regions of the electromagnetic spectrum. Figure 1 shows a high-level overview of the steps in baseline ASSET model. See [4] for a more detailed description.

This work improves the *Detector Response and Read-out & Electronics* blocks depicted in Figure 1. The photon flux incident at each detector is converted to a number of digital counts in the baseline model as follows. Photon radiance from the scene is imaged onto the FPA and spatially integrated over discrete detector areas, yielding the

total rate of photons incident on each detector (the input to the *Detector Response* block). The result is multiplied by the system integration time and quantum efficiency to generate the per-detector number of photo-electrons generated during an integration time. Dark current and various noise sources (e.g. read, shot, thermal) are then added. The resulting total number of electrons is divided by the *conversion gain* [electrons / count] to obtain fractional counts, which are then rounded down to integer counts, representing digitization and the introduction of quantization error. The digital output of the entire FPA is referred to as a *frame* of sensor data.

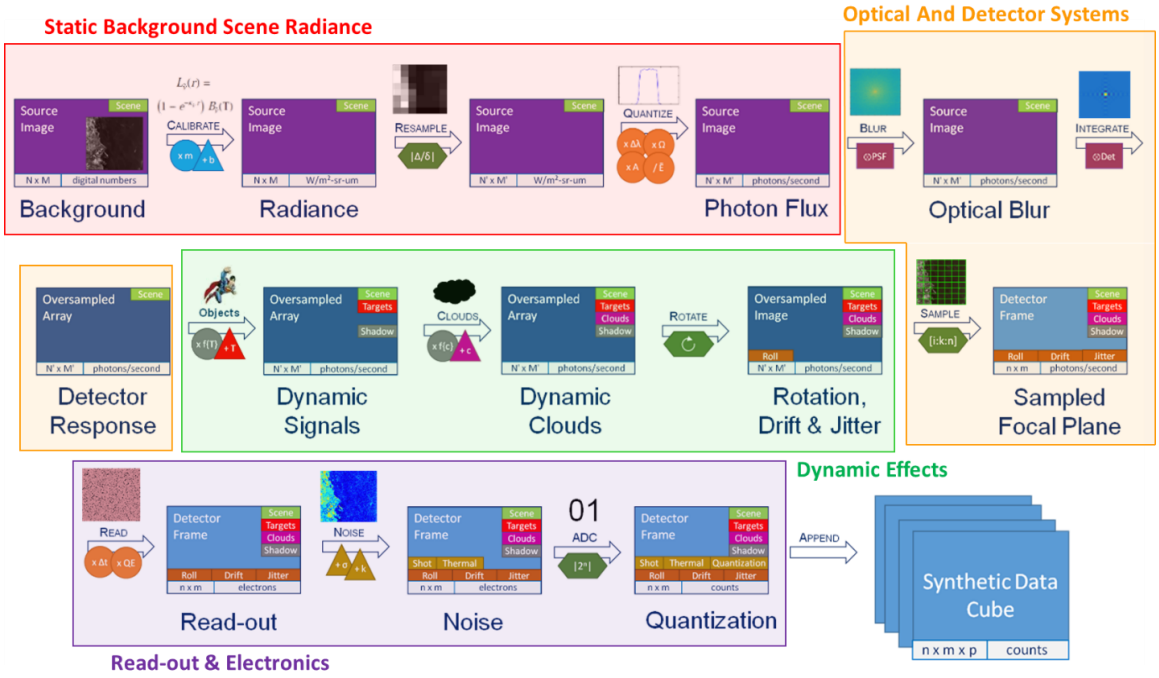

Figure 1. High-level overview of the physics-based image-chain process in the baseline ASSET model. The diagram is notional based on version 1.0 of ASSET [4].

ASSET begins with a high-resolution source image which provides the basis for the background scene [9]. Characteristics of the sensor, scene, source, viewing geometry, and noise are specified with an ASCII text configuration file containing all user-provided

parameters and the location of various support files. The baseline model then uses the source image to generate the spectral scene radiance in units of photons/s-m^2-sr-µm. Figure 2 illustrates how reflected, emitted, and path radiance contribute to the total spectral radiance incident at the sensor's aperture. In ASSET, for both reflected and emitted components, spectral radiance is attenuated by the atmosphere and path radiance is then added to obtain the total apparent spectral radiance at the aperture,

$$L_{app}(\lambda) = \left[L_{ref}(\lambda) + L_{ems}(\lambda, T) \right] \tau_{atm}^{sns}(\lambda) + L_{pth}(\lambda) \quad \text{[photons / s-m}^2\text{-sr-µm]}, \qquad (1)$$

where $L_{ref}(\lambda)$, $L_{ems}(\lambda)$, and $L_{pth}(\lambda)$ are the reflected, emitted, and path radiance, respectively; and $\tau_{atm}^{sns}(\lambda)$ is the atmospheric transmission from scene-to-sensor.[1]

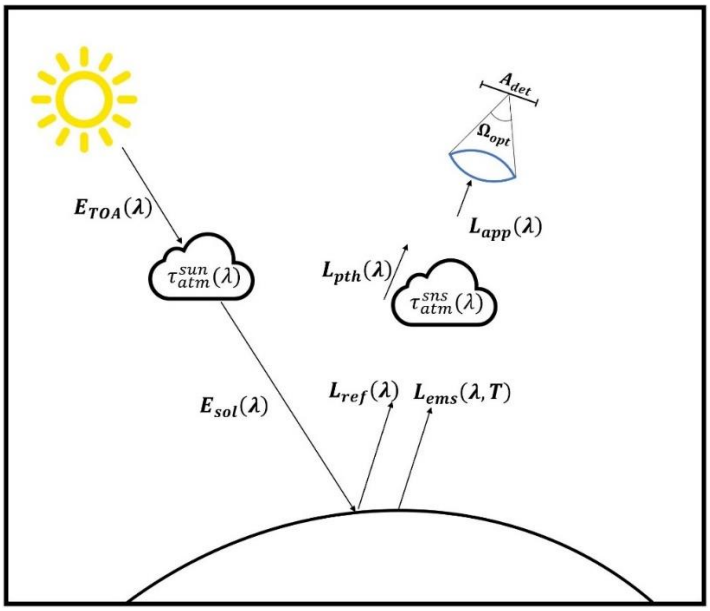

Figure 2. Contributions to total spectral radiance at the sensor's aperture. Top of the atmosphere (TOA) irradiance, $E_{TOA}(\lambda)$, is attenuated by the atmosphere to obtain the solar incident irradiance, $E_{sol}(\lambda)$. The spectral radiance for both reflected and emitted components is attenuated by the atmosphere and path radiance is then added to obtain the total spectral radiance at the aperture.

[1] Calculation of $L_{ref}(\lambda)$, $L_{ems}(\lambda)$, and $L_{pth}(\lambda)$ using radiometric and atmospheric properties is shown in Appendix A and B.

The optical components in the imaging system will introduce some limitations that will affect the efficiency of the system, and consequently the amount of signal measured by the sensor [3]. The transmission of the optics, among other sensor characteristics, will play a key role in defining the overall efficiency of the system. The spectral transmission of the optics $\tau_o(\lambda)$ reduces the amount of energy that arrives at the detector from the total energy captured by the receiver's aperture because secondary mirrors, lenses, and filters will block and attenuate some of the incoming radiation. Furthermore, self-emission from each individual component of the optical system will also contribute to the total radiation measured at the detector array [10], which is important when imaging in the MWIR through LWIR.

Given that a scene is viewed by a sensor with a certain spectral bandwidth, the total radiance is computed in ASSET by integrating the spectral radiance over the band of interest. If the sensor is only responsive to certain wavelengths, which are usually specified by the sensor's relative spectral response (RSR), we can generally integrate within the specified spectral band. The total scene radiance incident at a detector within a spectral band is given by

$$L_{det}^{scene} = \tau_{sys} \int_{\lambda} L_{app}(\lambda) R(\lambda) d\lambda \quad \text{[photons / s-m}^2\text{-sr]}, \tag{2}$$

where $R(\lambda)$ is the peak-normalized relative spectral response of the system, $L_{app}(\lambda)$ is the apparent spectral radiance, and τ_{sys} is the peak transmission through the optical system; the product of τ_{sys} and $R(\lambda)$ represents the unnormalized, wavelength-dependent transmission through the system that includes both optical system losses and filter attenuation: $\tau_o(\lambda) = \tau_{sys} R(\lambda)$. Here, L_{det}^{scene} is the total scene radiance imaged onto the

detector and does not include self-emission from the optical system (discussed next), which will also contribute to the total radiance at the detector. A more detailed description of the approximations used to model the radiometry and effects of the atmosphere can be found in appendices A and B, respectively.

To account for the imaging effects of the optical system, the optical point spread function (PSF) is convolved with the spatially resolved apparent spectral scene radiance, $L_{app}(X,Y,\lambda)$, where (X, Y) are horizontal and vertical coordinates in the detector plane. The PSF of an imaging system is the spatial impulse response of a system that accounts for diffraction (and potentially aberration) effects by the optics. A more detail description of the approximations used to model the PSF can be found in Appendix C.

A typical imaging system may contain several optical components such as lenses, mirrors, and filters, and it can become increasingly complicated to model the actual self-emission for these types of optical systems. We therefore make two simplifying assumptions. The first assumption is that the temperature is uniform along the optical path from the first lens (or mirror) to the detector. This assumption is reasonable since temperature changes across the optical path can be made negligible with good thermal controls. We further assume the sides of the optical path to have zero reflectivity so that light hitting the walls will not bounce back into the detector. Hence, a single optical transmission and an overall self-emission radiance can be used that accounts for all components in the optical system.[2] The baseline ASSET model generates the spectral

[2] ASSET does have the ability to model self-emission with both a cold stop and warm optics, but only the simpler one-temperature model is considered here.

self-emission produced by the optical system which is then band-integrated to obtain the total self-emission:

$$L_{SE}(X,Y) = \int_{\lambda} L_{SE}(X,Y,\lambda)d\lambda \quad \text{[photons / s-m}^2\text{-sr]}, \tag{3}$$

where $L_{SE}(X,Y,\lambda)$ is the spectral self-emission as a function of focal plane coordinate. The band-integrated radiance measured at the detector is therefore given by

$$L_{det}(X,Y) = L_{det}^{scene}(X,Y) + L_{SE}(X,Y) \quad \text{[photons / s-m}^2\text{-sr]}. \tag{4}$$

and additional details of these calculations can be found in Appendix C.

Since the detectors emulated in ASSET respond directly to photons, the total per-pixel radiance at the detector is converted to photon flux. Throughput, $A\Omega$, also known as etendue, is used to convert from photon radiance to photon flux falling on the detector, where Ω is the solid angle subtended at the source by an area A. In ASSET, the $A_{det}\Omega_{opt}$ product is used, since the detector size and the solid angle subtended by the optics at the detector are nearly constant and easy to determine for any imaging system. Thus, the total photon-flux at the detector is given by

$$\phi_{det}(X,Y) = L_{det}(X,Y)A_{det}\Omega_{opt} \quad \text{[photons / s]}, \tag{5}$$

where Ω_{opt} is the solid angle subtended by the optics at the detector with area A_{det}.

2.2 Focal Plane Array

The focus of this research is on the end-to-end process of modeling CCD and CMOS FPAs and read-out circuitry, thus a more in-depth description of the approximations used for the FPA and read-out circuitry will be presented in Sections 2.2 and 2.3. Again, the

model described here is of the baseline only and does not include the improvements implemented as part of this thesis; these enhancements will be discussed in Section 3.3.

The detector in an imaging system converts an optical signal (measured in photons) into an electrical signal (measured as current, voltage, or capacitance). This electrical signal is proportional to incident radiation arriving at the detector [1]. The detector in the imaging system will introduce some limitations that will affect the performance of the system, for example, the quantum efficiency of an imaging system is used to describe the fraction of incident photons converted to electrons, which affects the amount of signal measured by the sensor [3], and detector size places a limit on the spatial resolution of the imaging system.

To account for the effects of the optical system and sampling by the detectors, the image is convolved with the point spread function (PSF) of the optics and also with a detector response function (DRF). The PSF was described previously in Section 2.1. The DRF, $h_{det}(X,Y)$, represents the effects of spatial integration and sampling by the finite-size detectors and is convolved with the photon flux at the detector to determine the total photon flux incident in each pixel, $\phi_{det}(x,y) = \phi_{det}(X,Y) \otimes h_{det}(X,Y)$.[3] A more detail description of the approximations used to model the DRF can be found in Appendix C.

A detector does not directly measure photon flux. Rather, a fraction of photons incident on a pixel are converted to electrons over a finite duration referred to as the *integration time*. ASSET assumes mean photon flux is constant during an integration time, allowing the integral of photon flux with respect to time to be approximated as the

[3] Note that we have chosen the convention that (X,Y) are sub-pixel coordinates in the FPA and (x,y) are the subset of coordinates corresponding to pixel centers; (X,Y) is fixed but (x,y) may change from frame to frame as the focal plane move across the scene due to drift, jitter, or other pointing motion.

product of the photon flux and integration time Δt. This yields the mean number of photons incident during an integration time. The actual number of photons collected by a detector over an integration time follow Poison statistics, and the per-pixel value in ASSET is obtained as a random draw from a Poisson distribution whose mean is proportional to the expected number of photons [3]. Only a fraction of photons incident on a detector are converted to electrons; this fraction is referred to as the quantum efficiency, which is a wavelength-dependent quantity. In ASSET, the total number of photoelectrons generated in the detector by the incident photon flux is given by

$$n_{pe} = \mathrm{P}(\eta \Delta t \phi_{\mathrm{det}}) \ [\mathrm{e}], \tag{6}$$

where ϕ_{det} is the mean photon-flux measured by a single pixel, Δt is the integration time, P(μ) represents a random draw from a Poisson distribution with mean μ, and η is the band-average quantum efficiency of the detector. In order to capture the wavelength dependence of quantum efficiency in ASSET, it is separated into a constant term η and a relative term whose wavelength dependency is incorporated as part of the system's relative spectral response $R(\lambda)$.

Per Equation (6), the numbers of photoelectrons for all pixels in the FPA, $n_{pe}(x,y)$, are calculated identically. However, all pixels do not respond identically, and pixel-to-pixel non-uniformities must be applied to the detector array, resulting in fixed pattern noise (FPN) [1]. There are two primary components to non-uniformities in the detector frame: (1) dark signal non-uniformity (DSNU), $D(x,y)$, and (2) photo response non-uniformity (PRNU), $P(x,y)$; the term FPN usually refers to these two components and is due to material imperfections in the detector [4]. Fixed-pattern noise is not temporal and is spatially fixed with respect to the focal plane.

PRNU refers to variations in how a pixel responds to incident radiance and is a multiplicative factor of the photo-generated electrons. In ASSET, $P(x,y)$ is a user-defined relative non-uniformity centered on unity, thus representing minor differences in net generation of electrons in each pixel (deviations from the average quantum efficiency).

DSNU refers to the pixel-to-pixel variations in the offset (generally due to dark current) of the pixel values when no light is present at the detector surface and does not depend on signal [11]. In ASSET, DSNU is included as normally distributed variations in the dark signal as

$$n_{dark}^{DSNU}(x,y) = n_{dark} + \Delta t \sigma_{dark} X(x,y) = n_{dark} + D(x,y) \text{ [e]}, \quad (7)$$

where σ_{dark} is the user-specified RMS dark current (in electrons per second), $X(x,y)$ is an array of random draws from a normal distribution with mean $\mu = 0$ and variance $\sigma^2 = 1$, and $D(x,y)$ is the net variation in DSNU across the FPA. Thus, to account for perturbations due to the non-uniformities in the detector, the number of electrons in a detector frame is multiplied by the PRNU and DSNU is added,

$$n_{signal}^{FPN}(x,y) = n_{pe}(x,y)P(x,y) + n_{dark}^{DSNU}(x,y) \text{ [e]}, \quad (8)$$

where $P(x,y)$ accounts for FPN due to PRNU, n_{dark}^{DSNU} is the dark signal with DSNU included, and n_{signal}^{FPN} is the total signal in the detector with FPN included. Figure 3 shows an example of how non-uniformities are calculated in the baseline ASSET model.

Shot noise is caused by fluctuations in signal due to the discrete arrival of photons at the detector and discrete arrival of electrons in electrical components. Shot noise due to the time of arrival of photons (often referred to as *photon noise*) was accounted for in

Equation (6). The number of electrons counted during an integration time also follows a Poisson distribution with variance proportional to the mean number of electrons collected (photo-generated electrons and dark signal) during the interval, and the per-pixel value in ASSET is obtained as a random draw from a Poisson distribution whose mean is proportional to the expected number of electrons. In addition, since photo-generated shot noise is dependent on signal, and because FPN affects the number of collected electrons, FPN should be included before the shot noise calculations.

ASSET returns the detector frame with random samples of shot noise, n_{signal}^{shot}, drawn from an approximation of the Poisson distribution with a mean proportional to the sum of photo-generated signal plus the dark signal,

$$n_{signal}^{shot} = \mathrm{P}(n_{signal}^{FPN}) \quad [\mathrm{e}], \tag{9}$$

where n_{signal}^{FPN} is the signal in electrons with FPN included and P(μ) represents a random draw from a Poisson distribution with mean μ. Note that (*x*,*y*) have been dropped for conciseness but are implied, i.e. n_{signal}^{shot} and future quantities represent per-pixel values for the entire FPA where all pixel's noise values are independent and identically distributed (i.i.d.).

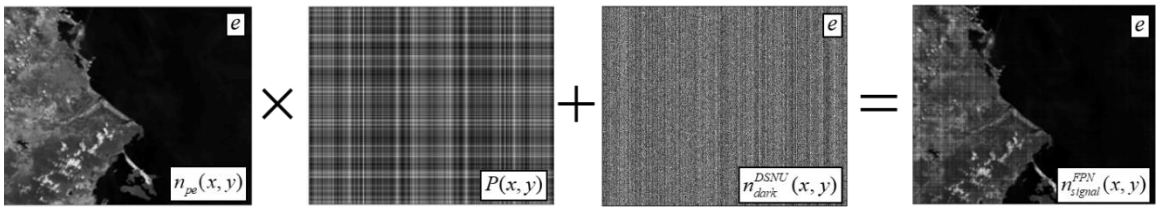

Figure 3. Examples of non-uniformities in ASSET; PRNU is multiplied by the photogenerated signal and electrons due to dark signal are added to obtain the detector frame with FPN. To account for perturbations due to the non-uniformities in the detector, the detector frame is multiplied by the PRNU and electrons due to dark signal are added.

The detector frame with shot noise (left) alongside an image of net fluctuation due to shot noise (right), obtained by subtracting n_{signal}^{FPN} from n_{signal}^{shot}, are displayed in Figure 4. From the figure it should now be evident that shot noise is dependent on signal since shot noise is larger in areas where the signal incident on the detector is larger. In other words, the signal coming from the ground generates more electrons than the signal coming from the water, and therefore, more shot noise is generated by the ground radiance.

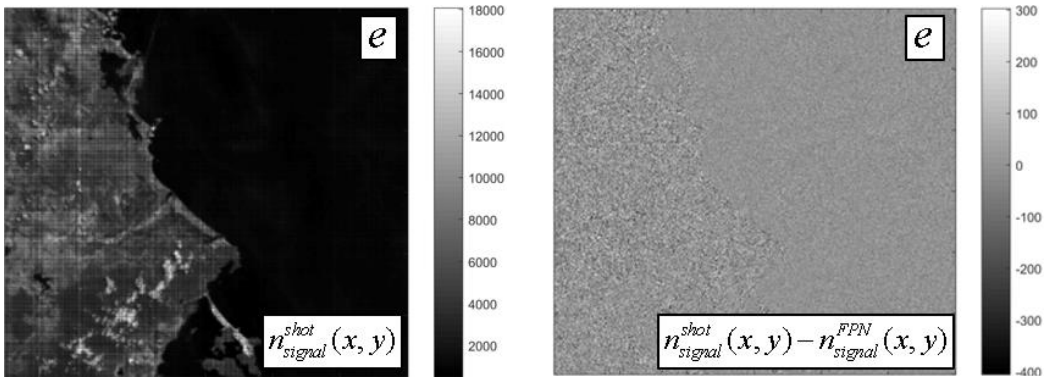

Figure 4. The signal image with shot noise (left) along an image of shot noise (right) obtained by subtracting n_{signal}^{FPN} from n_{signal}^{shot}. From the figure it is evident that shot noise is dependent on signal since shot noise is larger in areas where the signal incident on the detector is larger (e.g. signal coming from the ground generates more electrons than the signal coming from the water.

2.3 Electronics

The electronics in an imaging system transforms an analog signal in electrons into a digital signal in counts, also referred to as *digital numbers* (DNs). This digital signal is proportional to incident radiation arriving at the detector [1]. The electronics in the imaging system will introduce noise that will affect the performance of the system. Several of the noise components associated with the electronics are thermal, read, flicker,

and quantization noise. In addition to noise, we have additional offsets (or biases) due to the system's electronics.

Thermal noise, or *white* noise, arises from the random motion of carriers in any electrical conductor; any material that is not at 0 K produces electrons in the conduction band, resulting in thermal noise. Since the detector and electronics materials are not at 0 K, they will generate noise [3]. In ASSET, thermal noise is added as random draws from a time-dependent normal distribution with user-defined RMS $\sigma_{thermal}$,

$$n_{thermal} = \sigma_{thermal} X \sqrt{\Delta t} \quad \text{[e]}, \tag{10}$$

in the equation, $\sigma_{thermal}$ is the time-dependent RMS thermal noise (with units e/s$^{1/2}$), Δt is the integration time, and X is the array of i.i.d. random draws from a normal distribution with zero mean and unit variance. The product $\sigma_{thermal}\sqrt{\Delta t}$ scales the time-dependent RMS to units of electrons, which in turn scales the normal distribution's variance based on the specified integration time.

Read noise is the variance associated with *reading out* the signal collected by the detector and is similarly *white* noise. It is characterized as the noise measured with zero incident signal and zero integration time, and it comprises the noise added by the read-out electronics. As each pixel is read, some electrons are randomly lost or gained from the signal. In ASSET, read noise is added from a time-independent normal distribution with user-defined RMS σ_{read} (in units of electrons),

$$n_{read} = \sigma_{read} \; X \quad \text{[e]}, \tag{11}$$

where X is an array of i.i.d. random draws from a normal distribution with zero mean and unit variance. Unlike thermal noise, read noise is independent of integration time.

Regardless of how long the sensor integrates, there will be read noise of a fixed magnitude in every frame, but a long enough integration time will ensure the measured signal to be well above the read noise [12].

Flicker noise, also known as $1/f$ noise, is present in the electronics and is related to the mean current traveling through the detector. Flicker noise occurs in almost all electronic devices, and it results from a variety of effects, although these are usually related to the flow of direct current [13]. In ASSET, flicker noise is added as random draws from a distribution whose power spectrum is inversely proportional to frequency. The magnitude of the flicker noise is scaled to a user-defined RMS $\sigma_{1/f}$ (with units of electrons) and frequency dependence,

$$n_{1/f} = \sigma_{1/f} Y(f) \quad \text{[e]}, \tag{12}$$

where $\sigma_{1/f}$ is the RMS flicker noise and $Y(f)$ is an array of i.i.d. random draws from a $1/f$ (pink) noise distribution. In ASSET, the *pink* noise distribution is implemented using a distribution that goes as f^{β} where the argument β shapes the frequency characteristics of the distribution; this allows for other noise distributions to be add (for example, *brown* when $\beta = -2$).

Thermal, read, and flicker noise are then added to the detector frame to obtain the total analog signal in electrons. The total analog signal in the system with noise included is given by

$$n_{signal}^{total} = n_{signal}^{shot} + n_{thermal} + n_{read} + n_{1/f} \quad \text{[e]}, \tag{13}$$

where $n_{thermal}$, n_{read}, and $n_{1/f}$ are signals in electrons generated by thermal, read, and flicker noise and n_{signal}^{shot} is the total signal after shot noise. Furthermore, values for all

noise sources per pixel and per frame can be output independently. It is generally assumed n_{signal}^{shot} is much greater than the noise sources so that negative electrons do not occur. If the resulting signal value in electron units is negative, ASSET sets the negative values to zero. Figure 5 shows an example of how the total analog signal is obtained in ASSET with images of each noise.

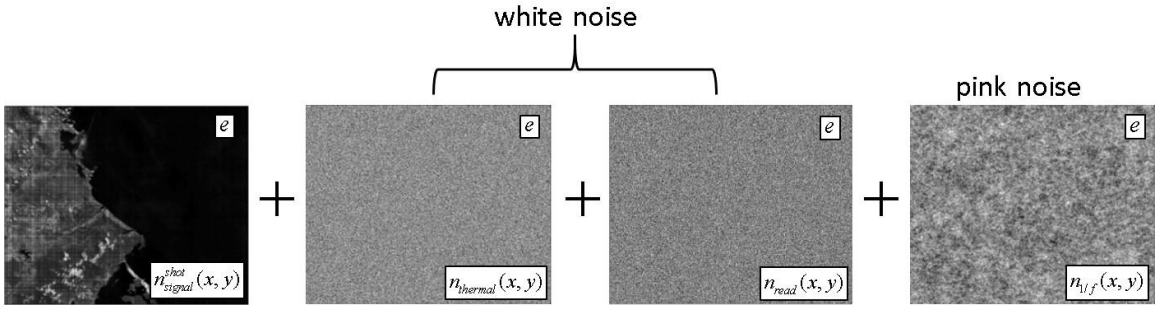

Figure 5. Example on how the total signal is obtained in ASSET. Noise components are added to the detector frame n_{signal}^{shot} to obtain the total analog signal in electrons. From left to right: Total signal after shot noise, thermal noise, read noise, and flicker noise. Also shown are the units and the distribution used for each noise.

The detector frame, n_{signal}^{total}, whose signal is in units of electrons and includes most noise sources, is quantized by dividing the signal by the conversion gain *CG* derived in ASSET from user-defined well-depth *w*, number of bits, and analog gain factor γ,

$$CG = \frac{w}{\gamma(2^{bits}-1)} \quad \text{[e/counts]}, \tag{14}$$

then,

$$DN = \frac{\gamma}{w}(2^{bits}-1)n_{signal}^{total} \quad \text{[counts]}. \tag{15}$$

The resulting count values are rounded down, introducing quantization error (*noise*) [4]. Quantization noise is directly proportional to the number of bits used: given *n* bits,

the signal can be separated into 2^n quantization levels. In ASSET, quantization noise is implemented by directly converting the electron signal to integer counts based on user-defined number of bits.

In ASSET, a hardware offset (DN_{offset}) represents an offset (or bias) of the system due to the system's electronics (*hardware*). It is included in ASSET to add a bias term that does not contribute to photon or electron noise, for example, a voltage bias resulting in a minimum count value greater than zero. Like *CG*, hardware offset is a term used to represent more complicated underlying physics. In ASSET hardware offset (DN_{offset}) is added directly to the digital number computed from signal and noise,

$$DN = \min\left\{ \left\lfloor \frac{\gamma}{w}(2^{bits}-1)n_{signal}^{total} \right\rfloor + DN_{offset},\ 2^{bits}-1 \right\} \text{ [counts]}, \tag{16}$$

where n_{signal}^{total} is the analog signal and *CG*. If the resulting count value is greater than the maximum allowed based on number of bits then the signal is capped at (2^{bits}-1).

Some sensors will collect a certain number of frames and then instead of outputting all the frames at once, the sensor co-adds (or sums) all those frames and sends only one co-added frame. This is generally done due to limited bandwidth (i.e. cannot download all frames) and is a means of increasing signal-to-noise at a reduced frame and data rate. This onboard co-add is be computed in ASSET by summing over a specified number of frames (called *subframes*). Depending on the system, the co-added frame may have a larger dynamic range (number of bits) than the individual subframes. In this case, *bits* refer to the subframe and *BITS* is used for the co-added frame.

Another parameter affecting the co-added frame is the digital gain. Digital gain is used in cases where 2^{BITS} -1 is also greater than the download bandwidth and is usually

used to prevent saturation in the output frame. Digital gain is expressed by 2^{-d}, where d is the digital gain coefficient, and it is multiplied with the sum of all subframes in counts:

$$DN(x,y) = 2^{-d}\sum_{j=1}^{N} DN_j(x,y) \quad \text{[counts]}. \tag{17}$$

In the equation, if d is zero, we get $2^0 = 1$ and the signal will remain unchanged, but if d is one, we get $2^{-1} = 1/2$ and the signal is reduced by half (as a bit shift). Since the digital gain can be used to decrease the number of counts it allows for larger signals to be encoded in the output frame, and then the gain can be undone in post-processing to restore the signal. However, this is at the cost of reduced signal resolution due to the loss of one or more least significant bits. Thus, digital gain trades least significant bits for most significant bits.

2.4 End-to-End Equation

In this model we considered the electromagnetic spectrum, radiometry, atmospheric transmission, the optical path, the detector, noise associated with the detector and electronics, and finally the analog-to-digital conversion from electrons to counts. Combining each of the pieces discussed in this section results in a complete analysis approach to a final end-to-end sensor process. Sensor output from processes modeled in ASSET can be represented as:

$$\begin{aligned} DN(x,y) &= 2^{-d}\sum_{j=1}^{n}\left\lfloor \frac{\gamma}{w}\left(2^{bits}-1\right)n_j(x,y) + DN_{offset}\right\rfloor \\ n_j(x,y) &= \Delta t\left(\eta P(x,y)\left[\phi_j(X,Y)\otimes h_{det}(X,Y)\right] + i_{dark}D(x,y)\right) \\ \phi_j(X,Y) &= A_{det}\Omega_{opt}\int\left[\tau_{sys}L_j^{app}\left(X,Y,\lambda\right)\otimes h_{opt}(X,Y) + L_{SE}\left(X,Y,\lambda\right)\right]R(\lambda)d\lambda \end{aligned} \tag{18}$$

where

A_{det} = Detector area [m^2]

A_{opt}/f_{eff}^2 = Solid angle subtended by the optics at the focal plane [sr]

d = Digital gain coefficient [unitless]

$D(x,y)$ = Dark Signal Non-Uniformity (DSNU) [unitless]

$DN(x,y)$ = Total number of counts [counts]

DN_{offset} = Hardware offset [counts]

$h_{det}(X,Y)$ = Detector response function (DRF)

$h_{opt}(X,Y)$ = Point spread function (PSF)

i_{dark} = Average dark current [e/s]

j = Subframe index [unitless]

$L_{app}(X,Y,\lambda)$ = Source radiance at the aperture [ph/s-m^2-sr-µm]

$L_{SE}(X,Y,\lambda)$ = Radiance from self-emission in the optics [ph/s-m^2-sr-µm]

n = Total number of electrons, including noise [e]

$P(x,y)$ = Photo Response Non-Uniformity (PRNU) [unitless]

$R(\lambda)$ = Spectral relative response [unitless]

w = Full-well number of electrons [e]

γ = Analog gain [unitless]

η = Average quantum efficiency [e/ph]

Δt = Integration time [s]

τ_{sys} = System's transmission [unitless]

$\phi(X,Y)$ = Band-integrated photon irradiance incident on the focal plane [ph/s]

(x,y) = FPA pixel indices [unitless]

(X,Y) = FPA sub-pixel coordinates [unitless]

ASSET is not intended to simulate a scene with absolutely correct radiance values, but rather is meant to emulate real data with the goal of modeling radiometrically realistic scenes and sensor response data quickly and realistically [4]. Thus, some physical effects and processes are not included here (e.g. sky shine). Some terms are approximations, and some are global representations of more complex processes.

Although ASSET provides many realistic noise, detector, and electronics properties, the focal plane model needs significant improvement in order to have full control over pixel read-out characteristics. As already described, all calculations from photons incident at the detector through to digital numbers are treated as linear processes in the baseline model. However, as each component in the system introduces a non-linearity, the output signal cannot be simplified as the input in electrons multiplied by a linear conversion gain *CG*. For example, in CCD and CMOS image sensors, conversion gain from electrons to voltage is given by q/C. In CCDs this term is relatively constant, but in CMOS devices the bias voltage across a photodiode's capacitor is small, causing a large change in capacitance from zero signal to high full-well performance, leading to a non-linear conversion gain for some CMOS image sensors. The model described above does not include the improvements implemented as part of this thesis; these enhancements will be discussed next.

3 Theoretical Background

The previous chapter provided an overview of the baseline ASSET model, including a description of the approximations used for detector and read-out circuitry. The model described does not include the improvements implemented as part of this thesis; these enhancements will be discussed in this chapter. This chapter presents the theoretical background on CCD and CMOS image sensors that will be modeled, discusses the basics of photodetection, and the CCD and CMOS photodiodes and their respective pixel architectures.

This research focuses on adding higher fidelity modeling of the FPA behavior to ASSET to more accurately reproduce a sensor's detector response to incident irradiance. Currently in ASSET, the input electrons are multiplied by the conversion gain in counts to convert from electrons to a digital signal. However, other processes need to be modeled in order to obtain realistic visual and statistical effects, representative of real data. Some of these processes include: conversion from electrons to voltage in the sense node, source follower gain, introduction of fixed-pattern noise (FPN) due to the electronics, correlated double sampling, and analog-to-digital converter (ADC) conversion from voltage to counts.

The FPA model covers conversion of photo-generated electrons to voltage (or current) and finally to digital numbers. It incorporates sense node and source follower gain non-linearity. It also includes noise sources associated with the detector and electronics such as shot, thermal, 1/f, reset, fixed-pattern, and quantization noise. The model aims to provide realistic noise characteristics and sensor artifacts to predict the performance of real imaging systems for given device specifications and design

parameters. The additional input sensor information provided to ASSET gives the user much more control over sensor FPA and electronics characteristics.

3.1 Photodiodes

Photodiodes operate on the principle that the absorption of photons creates a voltage difference or current proportional to incident photon flux. Although several kinds of detectors fall in this category, the common example is the basic photodiode. Photodiodes are not bidirectional but can be used in forward-biased (photovoltaic) or reverse-biased (photoconductive) modes. Photoconductive detectors measure the change in current as the photodetector's conductivity changes with the absorption of photons creating a depletion region in the n-type and p-type regions [14]. In a p-n junction diode, the diffusion dark current i_{dark} is expressed as

$$i_{dark} = i_0 \left(1 - e^{\frac{qV_{bias}}{kT}} \right) \text{ [e/s]}, \tag{19}$$

where V_{bias} is the bias voltage of the photodiode, T is the temperature in Kelvin, q is the electron charge, k is the Boltzmann's constant, and i_0 is the dark saturation current.

The total output current in the photodiode is equal to the sum of the photocurrent and dark current and is expressed as

$$i_{PD} = i_{pe} + i_{dark} = i_{pe} + i_0 \left(1 - e^{\frac{qV_{bias}}{kT}} \right) \text{ [e/s]}, \tag{20}$$

where i_{pe} is the photogenerated electron current. The plot in Figure 6, reproduced from [1, 15], illustartes the photodiode *I*-*V* curve of the current (*I*) vs bias voltage (*V*).

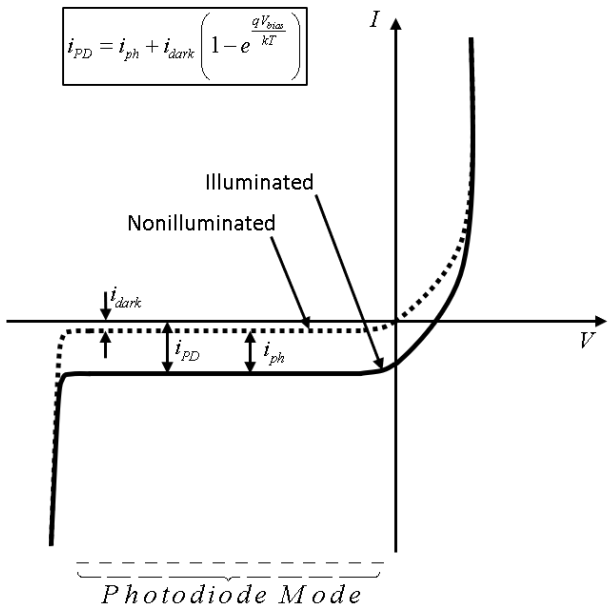

Figure 6. Bias voltage of photodiode versus current [1, 15].

When the photodiode is in reverse-biased mode, the exponential term in Equation (20) is neglected and the total output current becomes

$$i_{PD} = i_{pe} + i_{dark} = i_{pe} + i_0 \quad \text{[e/s]}, \tag{21}$$

and the total number of electrons collected by the photodiode is given by

$$n_{PD} = \Delta t\left(i_{pe} + i_{dark}\right) \quad \text{[e]}, \tag{22}$$

where Δt is the integration time.

The photodiode acts as a capacitor and is pre-charged to a reference voltage. As electrons are collected, the capacitance starts to discharge linearly with the number of electrons, n_{PD}. A photodiode can be represented by a current source i_{pe} in parallel with the photodiode's capacitance (C_{SN}) and resistance (R_{SN}). The circuit shown in Figure 7, based on [16], shows the photodiode and its equivalent circuit. The difference in voltage between the discharged value and the reference voltage is then amplified and further

processed by the electronics. In CCD arrays, the charge is transferred outside the pixel and then converted to a voltage. In CMOS arrays, the charge-to-voltage conversion process is done inside each pixel. In this thesis, the total pixel area is the photo-detector area and electronics combined. For example, in a CMOS sensor inside the pixel we have the detector, the sense node, and the source follower, whereas on a CCD sensor only the detector is inside the pixel. In other words, the detector is only the photo-sensitive part of the pixel. Section 3.2 discusses the key differences between CCD and CMOS sensors and describes their functionality according to their array architecture.

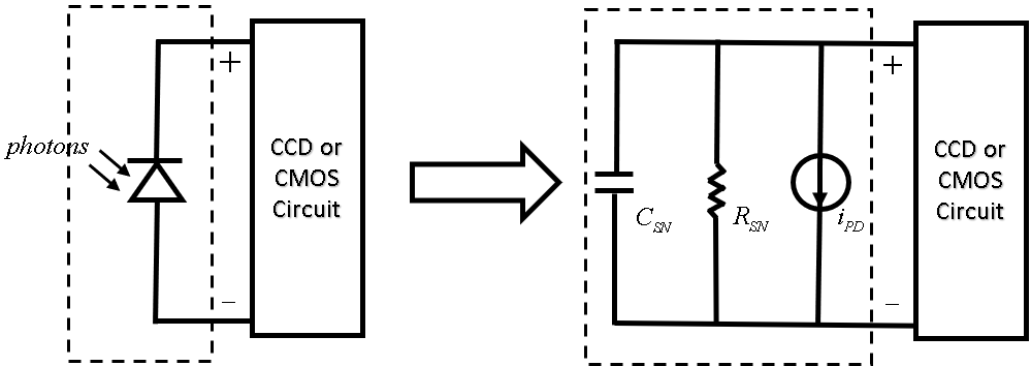

Figure 7. Photodiode and its equivalent circuit [16].

3.2 CCD and CMOS Read Out Technologies

In CCD and CMOS arrays, an image is produced from photons collected in the FPA's detectors. Each detector converts the incident photon flux into photoelectron flux at a rate determined by the quantum efficiency. Photoelectrons collected in the photodiode are converted to a voltage that is then amplified and converted to a digital signal. Both CMOS and CCD sensors are operated with a p-n or p-i-n junction photodiode with a reverse bias that produces a depletion region in the junction [14, 17, 18]. The primary difference between CCD and CMOS arrays is the readout architecture.

Figure 8 illustrates the differences between a CCD and CMOS image sensor array. This research is architecture agnostic in an effort to keep the model applicable to a large range of systems.

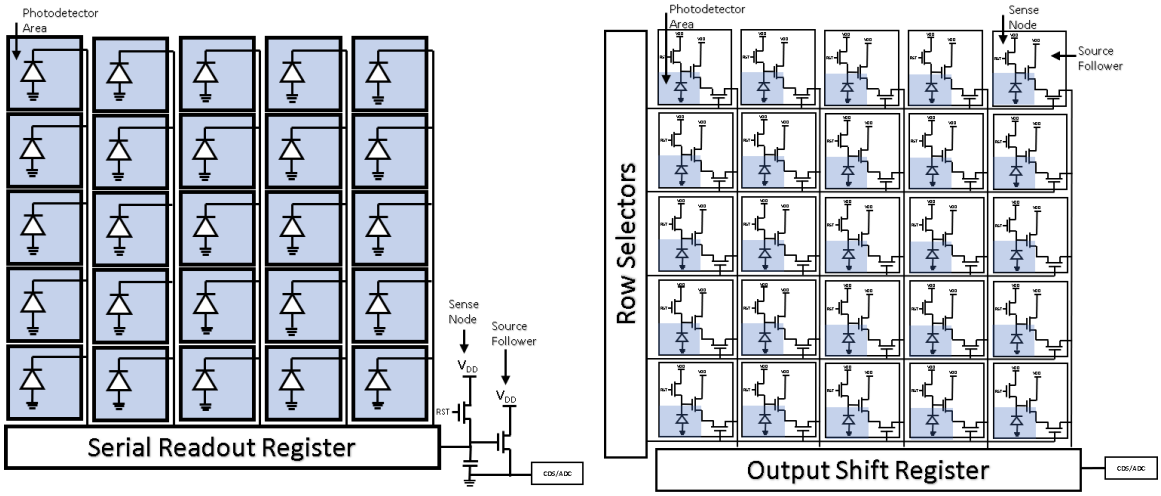

Figure 8. FPA Architectures of (left) CCD image sensors and (right) CMOS image sensors.

Converting a signal from photons to a digital signal is very similar in CCD and CMOS sensors, but storing, moving and reading out the signal are different [6]. In CCD sensors, charge is collected in the detector and transferred along columns to the serial readout register, where charge is again transferred to the sense node to be converted into a voltage or current signal. In CCD arrays, all pixels share the same sense node, source follower and output amplifier. As a result, differences in gain and offset are mainly due to variations in the photodetector and dark current, which exhibit as fixed pattern noise (FPN). Since the pixel output values are uncorrelated, a white noise model can characterize the FPN in CCD sensors [19]. In CMOS sensors, the pixel area is shared by the photodetector, sense node, and source follower. The FPN is mainly due to threshold

voltage differences between pixels. These differences are caused by variations in photodetectors, dark current, and mismatches of pixels' transistors. In addition, variations in CMOS column amplifiers cause a column-to-column FPN, which is very different to the noise observed in CCD sensors.

3.2.1 Pixel Circuit

CCDs provide the conversion of photons into a measurable voltage or current signal and refer to a semiconductor device in which charge is read out of the pixel into storage areas. In CCD image sensors, charge in the pixels is shifted out column-by-column (or row-by-row) and is stored in the sense node's capacitance outside the pixel (shown in Figure 8).

Once charge is collected in the pixel, electrons are transferred to the readout registers one column at a time, and the charge is transported to the sense node to be converted into a measurable signal in volts. The sense node creates a voltage proportional to the number of electrons collected. A simple CCD pixel circuit is shown in Figure 9.

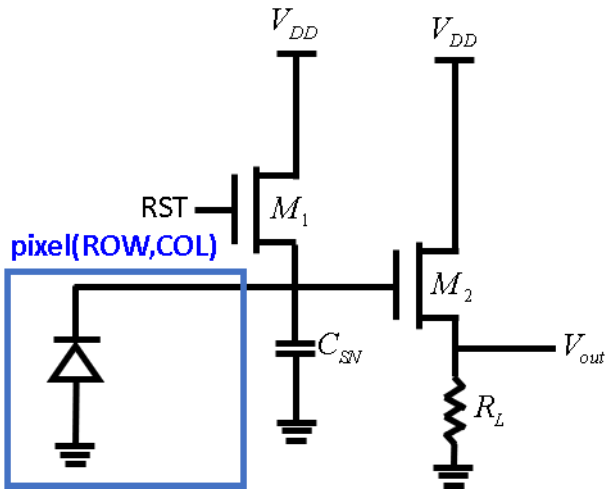

Figure 9. Schematic of a CCD sensor.

For CMOS image sensors the pixel area is shared by the photodiode, sense node, and source follower. Consequently, the charge-to-voltage conversion happens inside the pixel before it is read out. This is shown in Figure 8, where each pixel is comprised of the sense node and source follower. There are two types of CMOS pixel architectures: Passive Pixel Sensor (PPS) and Active Pixels Sensors (APS). The architecture of a PPS is simple. The pixel is composed only of one transistor for switching rows and the photodiode to convert photons into electrons (see Figure 10). Although a PPS has a large fill factor and consumes very low power, the signal-to-noise ratio can be very low. Since PPS cannot satisfy the high-performance requirements needed for most applications, they have been replaced by APS [15].

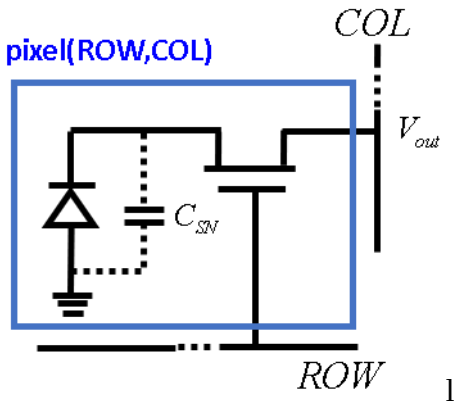

Figure 10. Schematic of a CMOS Passive Pixel Sensor (PPS).

CMOS APS are named after the number of transistors found inside the pixel (i.e. 3T-APS, 4T-APS, 5T-APS, etc.). As the number of transistors increases, the fill factor decreases but the noise is significantly reduced. 3T- and 4T- APS are the most used pixel circuits for imaging applications [15]. In contrast to the PPS circuit, in a 3T-APS two additional transistors are added, one to reset the signal in the photodiode and another to

read out the loading circuit (e.g. CDS and ADC circuits). The addition of the transistors significantly improves the performance compared to the PPS circuit. In a 4T-APS circuit and additional transistor is included to remove the reset noise from the reset transistor. Although the fill factor is reduced with the addition of the transistor, it also reduces the noise and extends the dynamic range of the system.

When the reset transistor is switched from the ground level to reference level the sense node capacitance is reset to the reference voltage. When the reset transistor is switched back to the ground level, integration time begins. During integration time, the pixel is selected using the transistor M_3 and the capacitor starts to discharge at a rate that depends on the number of electrons collected by the photodiode. Figure 11 shows the circuit of a 3T- and a 4T-APS. More complex pixel sensor architectures integrate correlated double sampling (CDS) and ADC inside the pixel to enhance image and noise performance. However, these additional features will reduce the fill factor in the pixel.

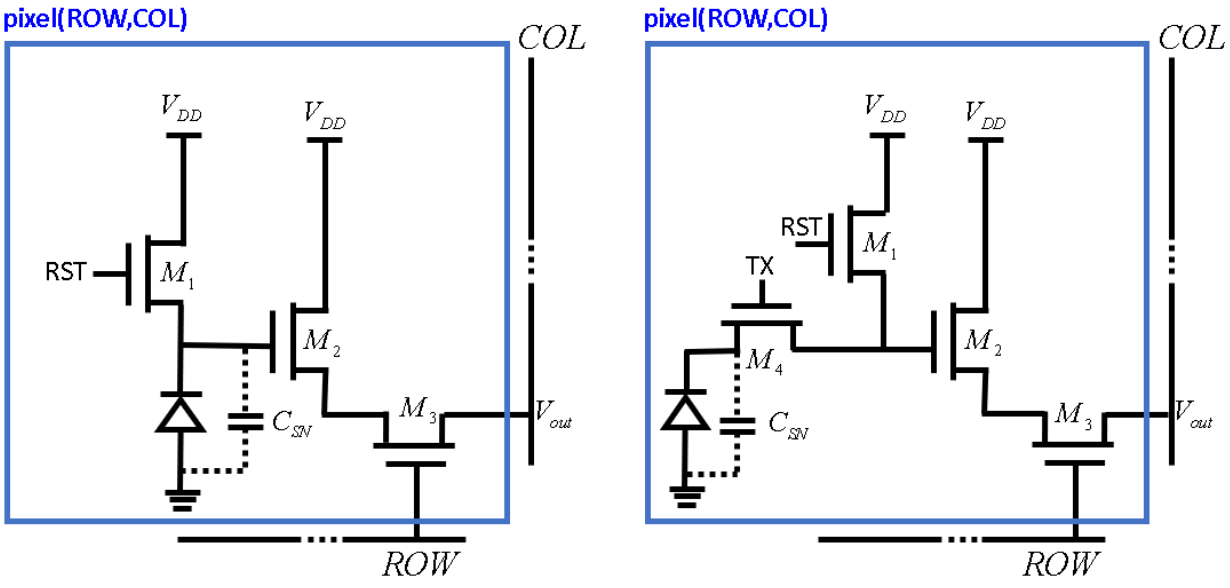

Figure 11. Schematics of (a) a CMOS 3T Active Pixel Sensor (3T-APS) and (b) a CMOS 4T-APS.

3.3 Sensor Model Description

Using a single model to represent the two different FPA architectures can be difficult because of differences in the charge to voltage conversion process and noise performance. However, the circuit shown in the schematic in Figure 12, based on Konnik's and Willers' models [5, 6], can be used to model both CCD and CMOS architectures with the correct set of parameters. The major difference between CCD and CMOS sensors is that the components from blocks 1-3 are contained inside the pixel for CMOS sensors, whereas a CCD pixel contains only the photodetector, making all other effects common to all pixels.

The system shown in Figure 12 is described by five blocks. (1) The input in units of photons per second is converted into electron current at a rate determined by the quantum efficiency. (2) The sense node integrates the electron current in the capacitor for a specified integration time and provides a voltage signal proportional to the electrons accumulated in the capacitor. The signal has a finite voltage capacity, constrained by the full-well capacity and the finite voltage swing of the sensor. The full-well capacity is the maximum number of electrons that can be stored in the capacitor and depends on detector size and the applied voltage on the capacitor [11]. (3) The source follower is used to readout the sense node's output signal to the loading circuit. (4) The correlated double sampling (CDS) circuit measures the source follower output (in either voltage or current, depending on circuit architecture) before and after integration time and removes pixel-to-pixel offset differences and reset noise. Finally, (5) the analog-to-digital converter (ADC) converts the analog signal to a digital signal in counts. The photon flux input to the imaging system should ideally be linearly proportional to the output digital signal.

However, as each component in the circuit introduces non-linearity, scaling the input signal will not produce the output signal over the entire dynamic range of the sensor. This is an important characteristic for image sensors, especially CMOS sensors, where non-linearity can be as high as 200% for some pixel architectures [7]. For CCD sensors, non-linearity is usually negligible and all processes, from charge conversion to signal digitization, are assumed to be linear.

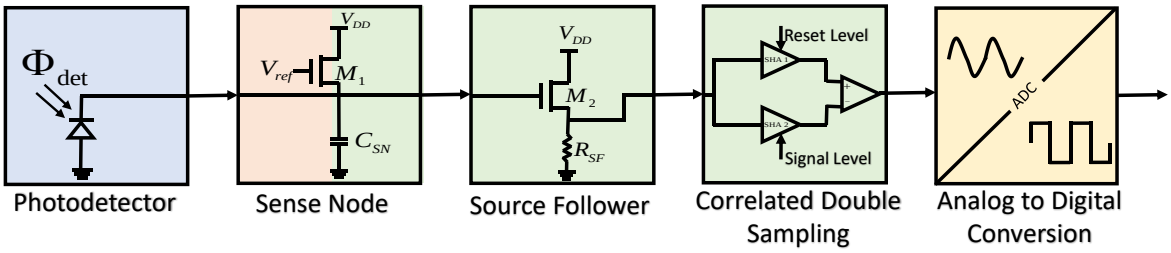

Figure 12. Block diagram for a typical CCD and CMOS image sensor [5, 6].

The improved FPA and electronics model based on Konnik's and Willers' work [5, 6] was implemented in MATLAB as part of the ASSET model discussed in Chapter 2, replacing the baseline linear conversion gain. The user can simulate CCD/CMOS sensors with switchable options that let the user turn on and off noise parameters and effects that are only applicable to either CCD or CMOS sensors. To start, the photon flux incident at the FPA (the *detector frame*), ϕ_{det}, is calculated from the total photon radiance (which includes all incorporated optical effects and scene content) incident at each detector (L_{det}), photo-sensitive detector area (A_{det}), and the solid angle subtended by the optics at the detector (Ω_{opt}):

$$\phi_{det} = \Omega_{opt} A_{det} L_{det} = \frac{A_{opt}}{f_{eff}^2} A_{det} \int \left[\tau_{sys} L_{app}(\lambda) + L_{SE}(\lambda) \right] R(\lambda) d\lambda \quad \text{[photons / s]}. \qquad (23)$$

The fill factor is the ratio of a detector's photo-sensitive area (i.e. detector area) to its total area, $FF = A_{det} / A_{pix}$. The fill factor in CMOS sensors can vary between 20-50%. Depending on the array architecture with CCD sensors, it can approach 100%. The detector frame is multiplied with the integration time and quantum efficiency to obtain the total number of electrons collected per frame, emulating the detector response to the total incident photon flux. The detector frame, now in units of electrons, is converted into a voltage signal by the sense node and is further processed into digital counts as shown in Figure 13. The block diagram depicted in Figure 13 is based on Konnik's [5] and Willers' [6] work and shows the FPA behavior recently added to ASSET.

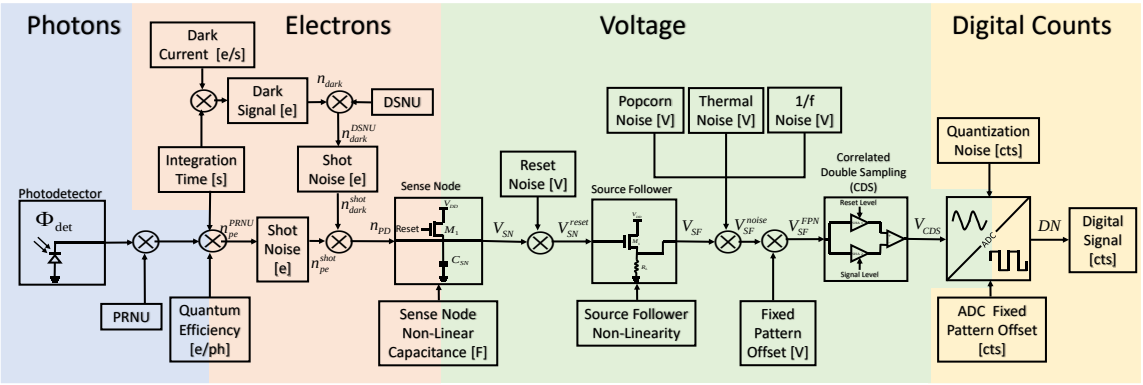

Figure 13. Process diagram of a CCD and CMOS image sensor [5, 6].

Realistic representations of real data require an accurate model of CCD/CMOS sensors with precise noise models. All noise sources appear as variations in the pixel output, but they can affect the output image differently. Noise sources are usually classified as spatial or temporal noise. Spatial noise, also referred to as FPN, is any noise with pixel-to-pixel variations that do not change from frame-to-frame (for constant incident irradiance). Spatial noise sets a limit on image sensor performance for most of

the dynamic range, especially for CMOS sensors, where each pixel exhibits a different offset level due to voltage differences between detectors. Temporal noise is often measured in individual pixels and is primarily due to shot, reset, thermal, $1/f$, and quantization noises. Unlike spatial noise, temporal noise changes from frame to frame and sets a limit on image performance under low illumination.

The improved FPA and electronics sub-model implemented in ASSET includes the components described above, shown in Figure 13. A more detailed description of the improved model follows, and a comparison of the model to experimental results for CMOS sensors is provided in Chapter 5.

3.4 Detector: Photon to Electron Conversion

A detector does not directly measure photon flux. Rather, a fraction of photons incident on a detector are converted to electrons over a finite duration. This time duration is referred to as the *integration time*. ASSET assumes mean photon flux is constant during an integration time, allowing the integral of photon flux with respect to time to be approximated as the product of the photon flux and integration time, Δt. This yields the mean number of photons incident during an integration time (or *frame*). The actual number of photons collected by a detector during a frame follows Poison statistics, and the per-detector value is obtained as a random draw from a Poisson distribution whose mean is proportional to the expected number of detected photons [3]. Only a fraction of photons incident on a detector are converted to electrons; this wavelength-dependent quantity is referred to as the quantum efficiency. In ASSET, the total number of photoelectrons generated in the detector by the incident photon flux is given by

$$n_{pe} = \eta \Delta t \phi_{det} \quad [\text{e}]. \tag{24}$$

where ϕ_{det} is the mean photon-flux incident on the detector array, Δt is the integration time, and η is the band-average quantum efficiency of the detector. In order to capture the wavelength dependence of quantum efficiency in ASSET, it is separated into a constant term η and a relative term whose wavelength dependency is accounted for as part of the system's relative spectral response $R(\lambda)$.

3.4.1 PRNU and Photoelectron Shot Noise

Photo response non-uniformity (PRNU) is a type of FPN and is mainly due to pixel-to-pixel variations in quantum efficiency, fill factor, and dopant concentration [5]. PRNU refers to variations in how a detector responds to incident irradiance under uniform illumination and is a multiplicative factor of the photo-generated electrons. PRNU for CCD and CMOS sensors is modeled as normally distributed with a standard deviation proportional to the incident photon flux and is usually expressed as a percentage of input incident photon flux:

$$n_{pe}^{PRNU} = n_{pe}\left(1 + P_N X\right) \quad [\text{e}]. \tag{25}$$

X is a random variable from a normal distribution with zero mean and unit variance, n_{pe} is the number of photo-electrons in the detector, and P_N is the PRNU quality factor (fraction of input signal), which varies from 0.01-0.05 (1-5%) for CCD and CMOS sensors [7]. n_{pe}^{PRNU} is then the signal in electrons with PRNU included.

PRNU will dominate shot and read noise over most of the dynamic range. Ideally the percentage of PRNU should be linear until reaching a full-well on the sense node capacitance. Although this is approximately true for CCD sensors, due to the non-linear

capacitance found on CMOS sensors, PRNU will decrease as the signal on the capacitor approaches saturation level in a CMOS array. Therefore, in order to accurately model PRNU for CMOS sensors non-linear effects need to be included in the model. This is different from the baseline ASSET model in that the baseline model calculates the shot noise only for photogenerated electrons and not for PRNU electrons.

Electrons arriving in the sense node at discrete increments create fluctuations in electrical current that can be modeled as a Poisson process. During an integration time, the actual number of electrons collected is a random variable from a Poisson distribution P(μ) with mean μ equal to the expected number of photoelectrons as follows:

$$n_{pe}^{shot} \sim P\left(n_{pe}^{PRNU}\right) \text{ [e].} \tag{26}$$

The difference between the actual and expected signal is known as shot noise, and n_{pe}^{shot} represents the photo-generated electron signal with shot noise included.

3.4.2 Dark Current, DSNU and Dark Shot Noise

Dark current is referred to as the current that is present in every pixel when there is no illumination on the photodetector. Although there are many types of dark current, dark current is mainly due to thermally generated photo-electrons. These electrons are collected in the sense node's capacitor and are included as signal. Consequently, when there are no incident photons on the detector, the pixel will still measure a signal and will contribute to the read noise floor. This will set a lower limit in the dynamic range, since that dark current is using space in the capacitance that could otherwise be used for photo-generated electrons. Dark current changes exponentially with temperature and increases by a factor of two every 6-8^{o} C [11, 5]. This means that at very low temperatures, dark

current is negligible and will be on the order of one electron for most applications. This is important, especially for MWIR and LWIR, where dark current noise can be as high as the photo-generated current if the FPA is not cooled [1]. The average dark current signal in electrons is given by [5, 6, 7]

$$n_{dark} = 2.55 \cdot 10^{15} \Delta t A_{pix} D_{FM} T^{3/2} e^{-E_g/2kT} \quad \text{[e]}, \tag{27}$$

where A_{det} is a pixel's photo-sensitive area [cm^2], T is the temperature [K], E_g is the bandgap energy of the semiconductor [eV], k is Boltzmann's constant, and D_{FM} is the dark current figure-of-merit [nA/cm^2]. The bandgap energy E_g is given by

$$E_g(T) = E_{g0} - \frac{\alpha T^2}{T + \beta} \quad \text{[eV]}, \tag{28}$$

where E_{g0} [eV], α [eV/K], and β [K] are all material constants. For the silicon bandgap energy $E_{g0} = 1.1557$ [eV], $\alpha = 7.021x10^{-4}$ [eV/K] and $\beta = 1108$ [K]. This model replaces the arbitrary dark signal from the baseline model in Equation (7) with a physics-based dark signal dependent on temperature, pixel area, and detector material.

Two sources of dark current noise are present in CCD and CMOS sensors: dark signal non-uniformity (DSNU) and dark shot noise. DSNU refers to an offset under dark conditions due to variations of the dark current from pixel-to-pixel. Small differences in the detector area and the substrate material during manufacturing create these variations. Thus, the mean dark signal will have non-uniformities exhibiting as FPN [5]. Most FPN models assume that the non-uniformities in PRNU and DSNU can be described using normal distributions. However, DSNU is caused by different processes than PRNU,

creating different statistics. This is driven by the outliers (or *hot pixels*) which generate much larger dark signal than the average dark current mean value.

The DSNU model presented in Konnik [5] shows that in the case of short integration times (0-100 s), the log-normal distribution should be used to obtain the *hot pixels* that are usually present in CMOS sensors. However, for long exposure times (longer than 100 s), the log-normal distribution does not describe the DSNU correctly [5, 6]. Konnik argues [5] that the log-normal distribution can be used for long exposure times if it is superimposed with other probability distributions (e.g. normal). In the improved ASSET model, DSNU for CCD and CMOS sensors is modeled as log-normally distributed proportional to the dark signal and is expressed as a percentage of dark electrons:

$$n_{dark}^{DSNU} = n_{dark}\left(1+Y\left(0, D_N^2\right)\right)[\mathrm{e}], \tag{29}$$

where $Y(\mu,\sigma^2)$ is a random variable from a log-normal distribution with zero mean and unit variance D_N^2; n_{dark} is the average dark signal generated in the photodiode, and D_N is DSNU quality factor (fraction of dark signal), which varies from 0.1-0.4 (10-40%) for CCD and CMOS sensors. Note that DSNU (D_N) is approximately 10-40 times larger than PRNU (P_N) [7]. Figure 14 shows a histogram of a log-normal distribution with $D_N = 0.4$, one can observe from the figure that the DSNU has only positive values and is positively skewed with a long tail (corresponding to *hot pixels*). Experimental results comparing the log-normal distribution to real data is shown in Chapter 5. The improved model differs from the baseline model in that the improved model replaces the Gaussian process by a log-normal distribution that accounts for *hot pixels* in the image sensor. Furthermore, dark current RMS is now calculated based on the DSNU quality factor D_N and the

physics-based dark signal, which depends on temperature, pixel area, and detector material.

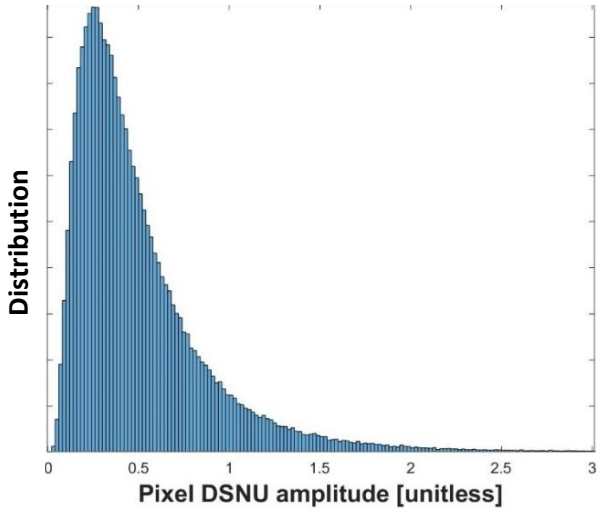

Figure 14. Histogram of a log-normal distribution with $D_N = 0.4$.

The photodetector randomly generates electrons due to dark current, creating dark shot noise. Similar to photo-generated shot noise, randomly generated electrons also cause fluctuations in electrical currents, creating dark shot noise. It follows a Poisson distribution, with variance proportional to the mean number of dark electrons generated by the photodetector. In ASSET, the electron signal with dark shot noise included is also a random variable drawn from a Poisson distribution, P(μ) with mean μ as:

$$n_{dark}^{shot} \sim P\left(n_{dark}^{DSNU}\right) \text{ [e]}, \tag{30}$$

where n_{dark}^{DSNU} is the mean dark signal in electrons. The total output signal in the photodiode that will be collected by the sense node capacitance can be determined by adding the mean dark signal, n_{dark}^{shot},and the mean photogenerated signal, n_{pe}^{shot}. The sense node will be discussed in the next section.

3.5 Sense Node: Charge to Voltage

Combining photo-electrons and dark current as described in Section 3.4 results in the total output signal from the photodiode that will be collected by the sense node capacitor. This signal is converted to a voltage signal, which is further processed and converted to digital counts. The total output signal from the photodiode is given as

$$n_{PD} = n_{pe}^{shot} + n_{dark}^{shot} \quad [\text{e}]. \tag{31}$$

In the sensor configurations shown in Figure 15, when the reset transistor is switched from the ground voltage level to the source voltage level, V_{DD}, the sense node capacitance is reset to the reference voltage V_{ref}, where $V_{ref} = V_{DD} - V_{th}$ or V_{DD} depending on the type of reset used (discussed in section 3.5.2).

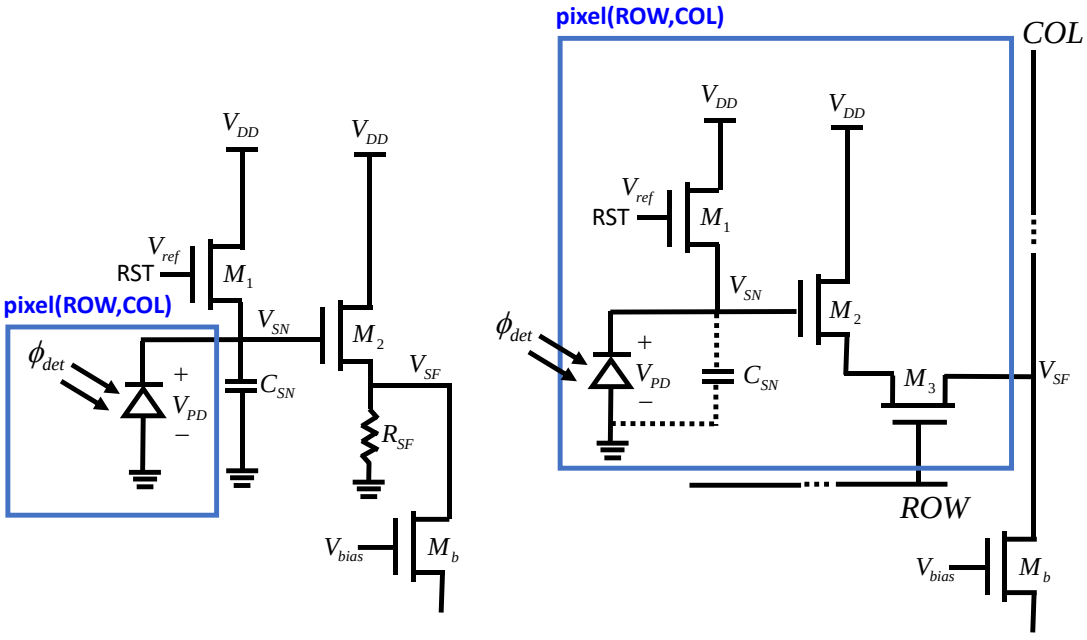

Figure 15. Pixel circuits for CCD (left) and CMOS (right) image sensor.

When the reset transistor is switched back to the ground level, integration time begins. The sense node integrates the electron signal, n_{PD}, in the capacitor for a specified

integration time and provides a voltage signal, V_{PD}, proportional to the electrons accumulated in the capacitor. For a capacitor with constant capacitance, the voltage is inversely proportional to the capacitance, C_{SN}. Thus, $V_{PD} = qn_{PD}/C_{SN}$. Both CCD and CMOS may exhibit non-linearity in the sense node. However, because CCDs operate in high reverse biased voltages (ranges from 4-10V), the sense node capacitance dependency on sense node voltage, V_{SN}, is negligible and is assumed to be linear. Whereas CCDs sense node capacitance is linearly proportional to the sense node voltage, CMOS operate at low reverse biased voltages and sense node capacitance non-linearity can be as high as 200% for some pixel architectures [7]. This is illustrated in Figure 16.

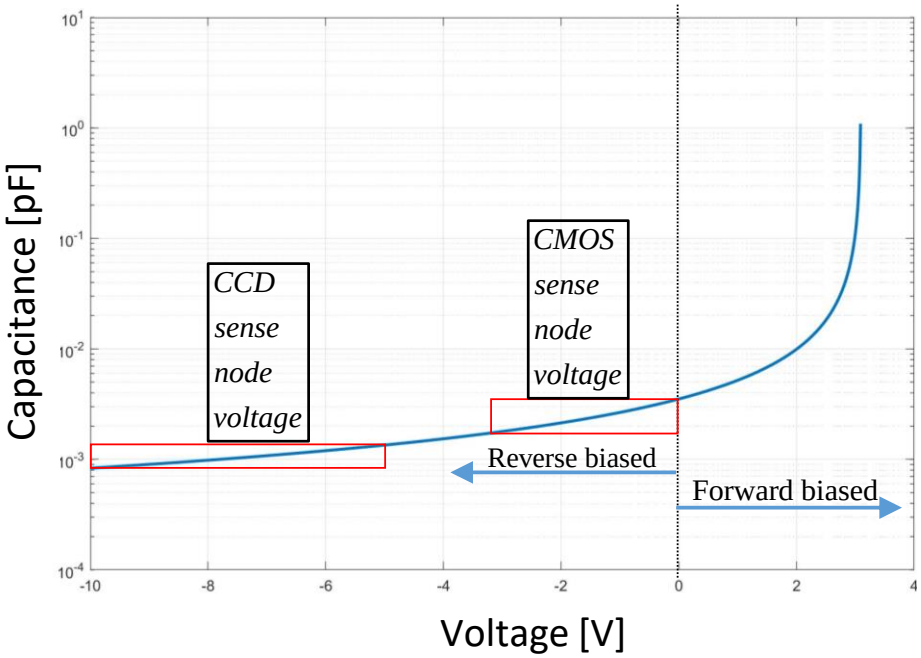

Figure 16. Sense node capacitance as a function of the voltage signal in the photodiode.

During the CCD sensor integration time, the sense node capacitor, C_{SN}, discharges linearly at a rate that depends on the number of electrons collected by the photodiode, n_{PD}, causing voltage in the sense node, V_{SN}, to drop by:

$$V_{SN} = V_{ref} - V_{PD} = V_{ref} - \frac{qn_{PD}}{C_{SN}} \text{ [V].} \quad (32)$$

V_{ref} is the reference voltage, V_{PD} is the voltage signal proportional to the electrons accumulated in the capacitor (n_{PD}), C_{SN} is the sense node capacitance, and q is the elementary charge of an electron. The conversion gain for a CCD sensor from electrons to voltage is $A_{SN} = q/C_{SN}$. The signal has a finite voltage capacity, constrained by the full-well capacity n_{fw} and the finite voltage swing of the sensor. The finite voltage swing in the pixel is $V_{swing} = V_{ref} - V_{bias}$, where V_{bias} is the bias voltage in the system (also called *hardware offset* when converted to digital counts). Note that the sense node voltage from Equation (32) is linear and is only used to model CCD sensors. A non-linear model is used for CMOS sensors. The non-linear model will be discussed next.

3.5.1 Non-Linear Model

Sense node non-linearity is due to the sense node capacitance C_{SN} [6, 7, 5]. During a CMOS sensor's integration time, the sense node capacitor, C_{SN}, discharges non-linearly at a rate that depends on the number of electrons collected by the photodiode. C_{SN} depends on the voltage across the capacitor, V_{SN}, therefore, the voltage signal in the photodiode may be non-linear. The non-linear capacitance is modeled in ASSET by a modified form of Tian's [20] model for CMOS sensors. The model starts linearly and introduces non-linear behavior as voltage signal, V_{PD}, increases. Tian's model introduces a non-linear capacitance, $C_{SN}^{nl}(V_{SN})$, which is also a function of the total number of electrons accumulated in the photodiode:

$$C_{SN}^{nl}\left(V_{SN}\right)=C_{SN}^{nl}\left(V_{SN_0}\right)\left(1-\frac{qn_{PD}}{2C_{SN}^{nl}\left(V_{SN_0}\right)\left(V_{SN_0}+V_{jp}\right)}\right)^{-1}\ \text{[F]}, \tag{33}$$

where V_{jp} is the built-in junction potential in the photodiode and V_{SN_0} is the initial voltage across the sense node capacitor, C_{SN}. Note that at the beginning of *integration time* ($\Delta t = 0$) the signal in the photodiode, n_{PD}, is equal to zero and from Equation (32) we get that the sense node voltage, V_{SN_0}, is equal to the reference voltage, V_{ref}. In addition, because the sense node capacitance is linear at the beginning of integration time, the initial non-linear sense node capacitance, $C_{SN}^{nl}(V_{SN_0})$, can be substituted with the linear sense node capacitance, C_{SN}. Consequently, the non-linear sense node capacitance in Equation (33) becomes

$$C_{SN}^{nl}\left(V_{SN}\right)=C_{SN}\left(1-\frac{qn_{PD}}{2C_{SN}\left(V_{ref}+V_{jp}\right)}\right)^{-1}\ \text{[F]}, \tag{34}$$

where C_{SN} is linear sense node capacitance and V_{ref} is the reference voltage. This equation is substituted into Equation (32) to obtain the non-linear sense node voltage, V_{SN}, that is measured by the source follower transistor M_2. The conversion gain for a CMOS sensor from electrons to voltage is $A_{SN}^{nl} = q/C_{SN}^{nl}(V_{SN})$. Figure 17 shows a plot of the sense node capacitance as a function of the sense node voltage; and a plot of the sense node voltage as a function of electrons for the linear and non-linear models. Note that for small signals the non-linear capacitance conveniently provides a higher gain A_{SN} and lower gain for large signals.

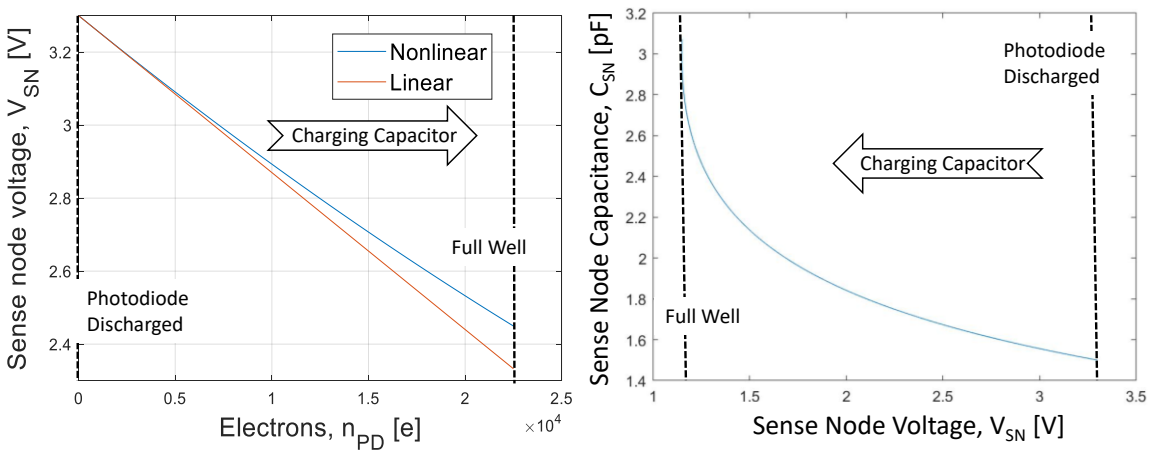

Figure 17. Plots of sense node voltage as a function of sense node capacitance (left) and electrons accumulated in the photodiode as a sense node voltage (right) showing sense node capacitance and sense node voltage non-linearity, respectively.

3.5.2 Reset Noise

During reset, the sense node transistor M_1 is set to the source voltage level, V_{DD}, and the sense node capacitance is reset to the reference voltage, V_{ref}. Resetting the sense node capacitor causes reset noise, which is called kTC noise. kTC noise is thermal noise due to current fluctuations in the M_1 transistor. The sense node reset noise voltage also depends on the type of reset used: *soft* or *hard reset*. In a hard reset, the reset gate (M_1) voltage is $> V_{DD} + V_{th}$ and $V_{ref} = V_{DD}$, where V_{th} is the threshold voltage in M_1. If the sense node's resistance is in parallel with the capacitor, the reset noise root-mean-square (RMS) voltage can be expressed as

$$\sigma_{reset}^{hard} = \sqrt{k_B T / C_{SN}} \quad [\text{V}], \tag{35}$$

where C_{SN} is the sense node capacitance. In a soft reset, the reset gate (M_1) voltage is set to V_{DD}, and $V_{ref} = V_{DD} - V_{th}$ reduces reset noise by a factor of $\sqrt{2}$. The soft reset noise is

$$\sigma_{reset}^{soft} = \sqrt{k_B T / 2C_{SN}} \quad [\text{V}]. \tag{36}$$

In CMOS sensors, reset noise behaves as additive, non-symmetric random variations in the reference voltage. Therefore, the noise distribution depends on whether the sensor is CCD or CMOS and whether a hard or soft reset technique is implemented. An inverse Gaussian distribution is used to model the hard-reset technique. The log-normal distribution is used to model the soft reset noise. In ASSET, reset noise is computed as

$$V_{reset} \sim N^{-1}\left(0, \sigma_{hard}^2\right) \quad [\text{V}] \tag{37}$$

or

$$V_{reset} \sim Y\left(0, \sigma_{soft}^2\right) \quad [\text{V}] \tag{38}$$

for a hard and soft reset, respectively. In these equations, $N^{-1}(\mu,\sigma^2)$ is the inverse Gaussian distribution and $Y(\mu,\sigma^2)$ is the log-normal distribution, both with mean μ and variance σ^2. In ASSET, the sense node reset noise voltage is added to the reference voltage in Equation (32) to account for the sense node reset voltage fluctuations

$$V_{SN}^{reset} = \left(V_{ref} + V_{reset}\right) - \frac{qn_{PD}}{C_{SN}^{nl}(V_{SN})} \quad [\text{V}]. \tag{39}$$

Next, the source follower reads out the sense node voltage V_{SN}^{reset} to the loading circuit. The readout is scaled by the source follower gain, A_{SF} [V/V]. In the next section the proposed source follower model will be presented. Note that the new model replaced the user-defined thermal noise with a physics-based model that accounts for reset noise in the sense node and is dependent on temperature and sense node capacitance.

3.6 Source Follower

In the CCD pixel configuration shown in Figure 15 (left), the source follower transistor M_2 is used to read out the sense node voltage signal V_{SN} to the loading transistor M_b (found at the column level for CMOS sensors), which is used outside the pixel in a CCD sensor and inside the pixel for a CMOS sensor. Both CCD and CMOS sensors use a source follower to transfer the voltage from the sense node to the loading circuit to be amplified and processed by the CDS. The linear source follower gain, A_{SF}, is expressed as

$$A_{SF} = \frac{g_m R_{SF}}{g_m R_{SF} + 1} \text{ [V/V].} \tag{40}$$

R_{SF} is the resistance in the source follower and g_m is the source follower field-effect transistor transconductance. For a CCD sensor, the output voltage in the source follower is expressed as

$$V_{SF} = A_{SF} V_{SN} + V_{SF}^{noise} = A_{SF}\left(V_{ref} - \frac{qn_{PD}}{C_{SN}}\right) + V_{SFnoise} \text{ [V],} \tag{41}$$

where $V_{SN}$is the sense node voltage and $V_{SFnoise}$ is noise added by the source follower (described in Section 3.6.2). A CCD sensor can have non-linearity of less than 1% over a sensor dynamic range because in CCD sensors $g_m R_{SF} >> 1$ and $A_{SF} \approx 1$. However, because CMOS sensors operate at lower reverse bias voltages (values less than 3.3V [21]), the source follower gain non-linearity can be significant and should be included in the CMOS sensor model [22].

3.6.1 Non-Linear Model

Like the sense node, the non-linear source follower will degrade the linearity of the CMOS sensor as it changes with the input signal in the pixel. The source follower gain, A_{SF}, varies with the sense node voltage, V_{SN}, and is approximated by Willers' [6] model

$$A_{SF}^{nl} = A_{SF}\left[1-(\gamma-1)\left(\frac{V_{ref}-V_{SN}}{V_{ref}-V_{fW}}\right)\right] \text{ [V/V]}, \tag{42}$$

where A_{SF} is the linear source follower gain, A_{SF}^{nl} is the non-linear source follower gain, V_{ref} is the reference voltage, V_{SN} is the sense node voltage, and γ is the non-linear error, which varies between 0.95-1.00 for increasing signals and 1.00-1.05 for decreasing signals [6]. Figure 18 shows a plot of the source follower gain, A_{SF}^{nl}, as a function of the sense node voltage, V_{SN}. Note that for small signals $A_{SF}^{nl} = A_{SF}$. In CMOS sensors a row select transistor M_3 is placed between the source follower and the load transistor. In this model we treat the select transistor M_3 as an ideal switch, since its resistance is approximately zero and will not have any effect on the output signal.

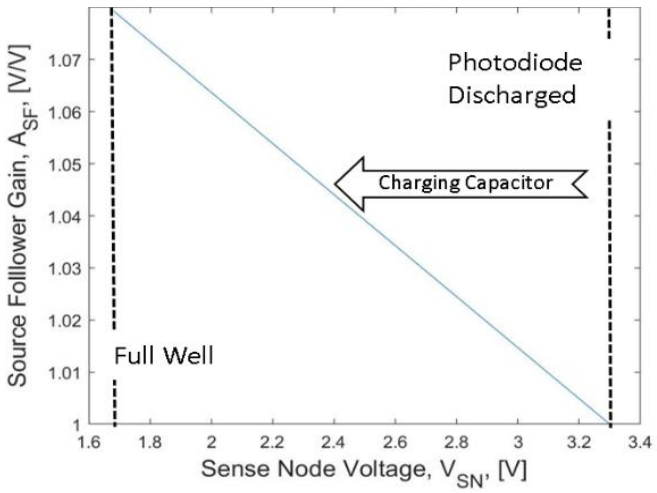

Figure 18. Source follower gain as a function of sense node voltage showing how the source follower gain increases with signal.

3.6.2 Source Follower Noise

There are three sources of noise associated with the source follower: thermal, flicker, and popcorn. These noises are usually the limiting factor in read noise for CCD and CMOS sensors. Like reset noise, thermal noise (called *white noise*), arises from the random motion of charge carriers in any electrical conductor that is not at 0 Kelvin. Charge carrier thermal motion in the source follower resistance component, R_{SF}, causes thermal noise [13].

Flicker noise, also known as $1/f$ noise, is present in the electronics and its power spectral density (PSD) is inversely proportional to its frequency bandwidth. The power spectral density of $1/f$ noise decreases as frequency increases and is only significant below 1 MHz [1]. Defects in the metal-oxide semiconductor cause the capture and release of mobile charge carriers, creating flicker noise.

Popcorn noise, like flicker noise, is due to random capture and release of mobile charge carriers. However, when the source follower transistor is small, as in CMOS sensors, this random capture and release of charge carriers becomes discrete and flicker noise turns into discrete random telegraph signals (RTS), also known as *popcorn noise* [5, 6].

In CCD sensors, source follower noise is limited by flicker noise while popcorn noise is negligible. In CMOS sensors, the source follower is limited by the popcorn noise. This is because the source follower's transistor in CMOS sensors is used inside the pixel and is much smaller than the source follower used in CCD sensors. An approximation of the source follower noise standard deviation is given by [5]

$$\sigma_{SF} = \frac{1}{A_{SF}\left(1-e^{-t_s/\tau_D}\right)}\left[\int_0^{\infty} S_{SF}(f)H_{CDS}(f)df\right]^{1/2} \quad [\text{V}], \tag{43}$$

where A_{SF} is the linear source follower gain, t_s is the correlated double sampling (CDS) sample-to-sample time in seconds, $\tau_D = t_s/2$ is the CDS dominant time constant, f is the electrical frequency in Hz, $S_{SF}(f)$ is the source follower's noise power spectrum, and $H_{CDS}(f)$ is the CDS transfer function.

The source follower's power spectrum is comprised of all three sources and can be expressed as

$$S_{SF}(f) = \sigma_{thermal}^2\left(1+\frac{f_c}{f}\right) + S_P(f) \quad [\text{V}^2/\text{Hz}], \tag{44}$$

where $\sigma_{thermal}$ is the RMS thermal noise $[V/\sqrt{Hz}]$, f_c is the flicker noise corner frequency in Hz, and $S_P(f)$ is the popcorn noise power spectrum [V^2/Hz]. Since the popcorn noise power spectrum is only noticeable at low frequencies, as in CMOS sensors, $S_P(f) \approx 0$ for CCD sensors [5].

The popcorn noise power spectrum is given by

$$S_P(f) = \frac{2\Delta I^2 \tau_P}{4+\left(2\pi f \tau_P\right)^2} \quad [\text{V}^2/\text{Hz}], \tag{45}$$

where τ_P is the popcorn noise characteristic time constant in seconds and ΔI is the source follower current modulation induced by popcorn noise.

The CDS transfer function $H_{CDS}(f)$ is given by

$$H_{CDS}(f) = \frac{\left[2-2\cos\left(2\pi f t_s\right)\right]}{1+\left(2\pi f \tau_D\right)^2}. \tag{46}$$

The parameters used to evaluate this equation are usually provided in the specifications for the sensor, and equations (44), (45) and (46) should be evaluated for each frequency, $f = 1,2,\ldots,f_{clock}$ [5]. Source follower noise with variance σ_{SF}^2 is computed in ASSET as

$$V_{SFnoise} = \sigma_{SF} X \quad [\text{V}]. \tag{47}$$

where X is a normally distributed random variable with zero mean and unit variance. This noise value is then added as shown in Equation (41) to yield the output source follower voltage, V_{SF}.

3.6.3 Fixed Pattern Offset

The process to convert a signal from photons to a digital signal is very similar in CCD and CMOS sensors, but the methods used to store, move and read out the signal differ [6]. Recall from Section 3.2 that in CCD sensors, charge is collected in each detector and then transferred along columns to the serial readout register where charge is again transferred to the sense node to be converted into a voltage or current signal. In CCD arrays, all pixels share the same sense node, source follower and output amplifier. As a result, differences in gain and offset are mainly due to variations in the photodetector, exhibiting as PRNU and DSNU. Since the pixel output values are uncorrelated, a white noise model can be used to characterize the FPN in CCD sensors [19].

In addition to PRNU and DSNU, CMOS sensors have a pixel-to-pixel offset FPN due to threshold voltage differences between each pixel's transistors in the sense node and source follower because the pixel area is shared by the photodetector, sense node and

source follower. Furthermore, variations in column amplifiers will cause a column-to-column offset FPN which is very different from the noise seen in CCD sensors. Therefore, CMOS modeling requires an additional pixel-to-pixel and column-to-column offset FPN component that is not present in CCD sensors. In the CMOS circuit shown in Figure 15 (right), the pixel architecture includes several transistors, some of which are shared by pixels and some are not. Variations in these transistor's threshold voltages will introduce an additional pixel and column offset FPN. Pixel FPN is caused by variations in threshold voltages in M_1, M_2, and M_3, whereas column FPN is caused by variations in bias voltage in M_b and offset variations in the column amplifier. To model the offset FPN in CMOS sensors, we express V_{FPN} as the sum of a column FPN component, V_{FPN}^{col}, and an individual pixel FPN component, V_{FPN}^{pix}. Thus,

$$V_{FPN}(i, j) = V_{FPN}^{col}(j) + V_{FPN}^{pix}(i, j) \quad [\text{V}], \tag{48}$$

where V_{FPN}^{col} and V_{FPN}^{pix} are defined below, and *i* and *j* are row and column indices.

Gammal introduces a statistical model for FPN in CMOS sensors which sums the pixel and column FPN components [19]. In this model, two assumptions are made. The first is that the column FPN random process and the pixel FPN random process are uncorrelated. This assumption is valid because the pixel and column FPN are caused by different processes in the CMOS circuit. The second assumption is that column and pixel FPN processes are isotropic, and the autocorrelation functions for both processes are space invariant. The model parameters characterize the standard deviation of a pixel and column FPN component and the spatial correlation between pixels and columns for the entire FPA. Spatial correlation means that there is a signal dependency between a pixel

(or columns) and its neighboring pixels (or columns), also referred to as pixel and electronic cross-talk [23]. Short pixel and column separation increase the spatial correlation as adjacent pixels or columns will have similar signal components [19].

In this model, an autoregressive process simulates column and pixel FPN, since their mean and variance can be estimated from image sensor data [19]. Column offset FPN is modeled as a first order isotropic autoregressive process and is given by

$$V_{FPN}^{col}(j) = a\left[V_{SF}(j-1) + V_{SF}(j+1)\right] + \sigma_{FPN}^{col} X(j) \quad \text{[V]}, \tag{49}$$

where X is an array of i.i.d. normal random variables with zero mean and unit variance, and $0 \leq a \leq 0.5$ characterizes the dependency of V_{FPN}^{col} on its two neighboring columns. The RMS column offset FPN noise is given by

$$\sigma_{FPN}^{col} = V_{fW} D_N^{col} \quad \text{[V]}, \tag{50}$$

where D_N^{col} is the column offset FPN quality factor (percentage of full-well voltage signal, V_{fw}) and $V_{fw} = qn_{fw}/C_{sn}$ is the voltage signal corresponding to full-well. The voltage signal $V_{FPN}^{col}(j)$ is replicated for every row to obtain an array of the appropriate size.

Pixel offset FPN, V_{FPN}^{pix}, is modeled as a two-dimensional autoregressive process and is given by

$$V_{FPN}^{pix}(i,j) = b\left[V_{SF}(i-1,j) + V_{SF}(i+1,j) + V_{SF}(i,j-1) + V_{SF}(i,j+1)\right] + X(i,j)\sigma_{FPN}^{pix} \quad \text{[V]}, \tag{51}$$

where again X is an array of i.i.d. normal random variables with zero mean and unit variance, and $0 \leq b \leq 0.25$ characterizes the dependency of V_{FPN}^{pix} on its four neighboring pixels. The RMS pixel offset FPN noise is given by

$$\sigma_{FPN}^{pix} = V_{fW} D_N^{pix} \quad [\text{V}] \tag{52}$$

and D_N^{pix} is the pixel offset FPN quality factor (percentage of full-well voltage signal V_{fw}). The total voltage signal after offset FPN is expressed as

$$V_{SF}^{FPN} = V_{SF} + V_{FPN} = A_{SF} V_{SN} + V_{SF}^{noise} + V_{FPN} \quad [\text{V}], \tag{53}$$

where V_{SF} is the total voltage signal from Equation (41), V_{FPN} is the sum of the pixel and column offset FPN given in Equation (48), and row and column indices have been dropped for conciseness. This offset FPN will be partly or completely removed from the output signal if a correlated double sampling (CDS) circuit is used. Currently in ASSET, a CDS compensation factor is used to reduce the reset noise in CMOS sensors, or the user can disable the noises (in the ASSET configuration file) that would have been removed by the CDS instead. This model deviates significantly from the baseline model in that the new model adds a pixel-to-pixel and a column-to-column offset FPN component that is present in CMOS sensors.

3.7 Correlated Double Sampling (CDS)

Correlated double sampling (CDS) is a method for measuring voltage signals that removes undesired noise and offsets [6, 7, 5, 24]. In this method the source follower's output is measured twice: once before integration time starts when the pixel is in reset mode (t = 0) and once after integration time ends when charge has been completely transferred to the CDS ($t = \Delta t$). By subtracting two samples of the signal, if the noise components are correlated to each other, the noise will be removed or reduced depending on how correlated they are. The main sources of noises in CCD and CMOS sensors, which are present in the raw output signal are [25]:

- Shot noise due to random arrival of electrons in the sense node and electrons being generated randomly by the photodetector (dark shot noise).
- PRNU due to small pixel-to-pixel variations in the detector area and in the substrate material during manufacturing.
- DSNU, caused by variation under dark conditions due to variations on the dark current from pixel-to-pixel.
- Reset noise in the sense node transistor (M_1), caused by thermally generated electrons in the sense node.
- Source follower noise, caused by thermally generated electrons, flicker noise, and popcorn noise.
- Offset FPN, due to voltage threshold variations in transistors M_1, M_2, M_3, M_b. and signal mismatches between column-level ADCs.

The offset FPN and reset noise are the only sources of noise, from those described above, which can be removed or reduced by implementing CDS. In addition, if the time between the two measurements is small, the source follower noise will also be reduced. Noise sources that happen before the sense node (e.g. shot noise, DSNU, and PRNU), cannot be removed by the CDS.

This first signal stored in the CDS circuit occurs when the image sensor is in reset mode before integration time begins. This signal is the sum of the reference voltage signal (V_{ref}), noise, and offset FPN. Before integration time begins, the reset transistor M_1 is switched from the ground level to the source voltage level, V_{DD}, and the sense node

capacitance is reset to the reference voltage, V_{ref}. The reset noise is then added as shown in Equation (39), repeated here for convenience,

$$V_{SN}^{reset}(0) = V_{ref} + V_{reset}(0) - \frac{qn_{PD}(0)}{C_{SN}^{nl}(V_{SN})} = V_{ref} + V_{reset}(0) \quad [\text{V}]. \tag{54}$$

Note that in reset mode, $n_{PD}(0) = 0$ and the last term in the equation goes away. The source follower reads out the sense node voltage, $V_{SN}^{reset}(0)$, to the loading circuit and in the process is multiplied by the source follower gain, A_{SF}. The reset noise and offset FPN is then added as shown in Equation (53), yielding the output source follower voltage at zero integration time:

$$V_{SF}^{FPN}(0) = A_{SF}(0)\left(V_{ref} + V_{reset}(0)\right) + V_{SFnoise}(0) + V_{FPN} \quad [\text{V}], \tag{55}$$

where $A_{SF}(0)$, $V_{reset}(0)$ and $V_{SFnoise}(0)$ are the source follower gain, reset noise, and source follower noise, respectively, at zero integration time. Note that the reference voltage, V_{ref}, and the offset FPN, V_{FPN}, do not depend on signal and will be constant for all integration times [24]. When the reset sample-and-hold transistor, M_{SHR} (shown in Figure 19), is turned on, the reset transistor, M_1, is switched from the ground level to the V_{DD} level and the voltage signal in reset mode, $V_{SF}^{FPN}(0)$, is stored in capacitor C_R to be later subtracted from the voltage signal at the specified integration time, Δt.

When integration time begins, the capacitor starts to discharge at a rate that depends on the number of electrons collected by the photodiode. Per Equation (39), the voltage in the sense node is expressed as

$$V_{SN}^{reset}(\Delta t) = V_{ref} + V_{reset}(\Delta t) - V_{PD}(\Delta t) \quad [\text{V}], \tag{56}$$

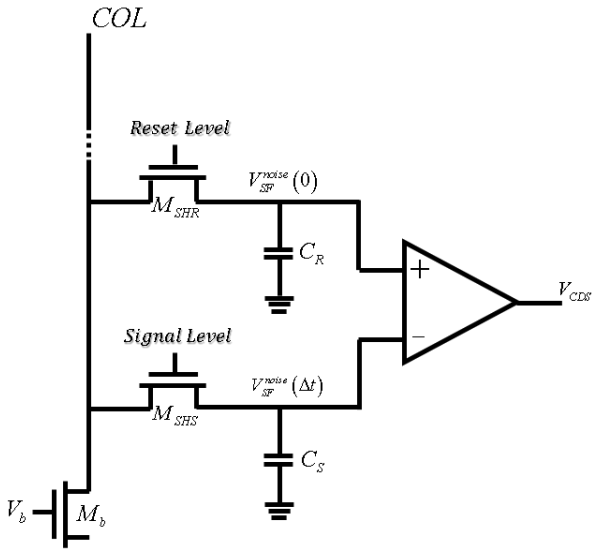

Figure 19. Schematic diagram of a CDS circuit.

where $V_{PD}(\Delta t) = qn_{PD}(\Delta t)/C_{SN}(V_{SN})$ is the voltage signal in the photodiode at integration time $t = \Delta t$. Similar to the reset signal, the source follower reads out the sense node voltage, $V_{SN}^{reset}(\Delta t)$, to the loading circuit and in the process is multiplied by the source follower gain, A_{SF}. The reset noise and offset FPN are also added as shown in Equation (53), yielding the output source follower voltage at the specified integration time, Δt,

$$V_{SF}^{FPN}(\Delta t) = A_{SF}(\Delta t)\left(V_{ref} + V_{reset}(\Delta t) - V_{PD}(\Delta t)\right) + V_{SFnoise}(\Delta t) + V_{FPN} \quad [\text{V}], \qquad (57)$$

where $A_{SF}(\Delta t)$, $V_{reset}(\Delta t)$, and $V_{SFnoise}(\Delta t)$ are the source follower gain, reset noise and source follower noise, respectively, at the specified integration time, Δt. When the sample-and-hold transistor, M_{SHS}, is turned on, the source follower signal, $V_{SF}^{FPN}(\Delta t)$, is stored in capacitor C_S.

Once both the reset and voltage signal have been stored, the reset signal, $V_{SF}^{FPN}(0)$, is subtracted from the voltage signal, $V_{SF}^{FPN}(\Delta t)$, to remove the undesired signals. The total output signal, V_{CDS}, from the CDS circuit is expressed as

$$\begin{aligned} V_{CDS} &= A_{CDS}\left(V_{SF}^{FPN}(0) - V_{SF}^{FPN}(\Delta t)\right) \\ &= A_{CDS}\begin{pmatrix} A_{SF}(0)\left(V_{ref} + V_{reset}(0)\right) + V_{SFnoise}(0) + V_{FPN} \\ -\left[A_{SF}(\Delta t)\left(V_{ref} + V_{reset}(\Delta t) - V_{PD}(\Delta t)\right) + V_{SFnoise}(\Delta t) + V_{FPN}\right] \end{pmatrix} \\ &= A_{CDS}\begin{pmatrix} V_{ref}\left[A_{SF}(0) - A_{SF}(\Delta t)\right] + \left[A_{SF}(0)V_{reset}(0) - A_{SF}(\Delta t)V_{reset}(\Delta t)\right] + \\ \left[V_{SFnoise}(0) - V_{SFnoise}(\Delta t)\right] + A_{SF}(\Delta t)V_{PD}(\Delta t) \end{pmatrix} \\ &= A_{CDS}\left(V_{ref}\Delta A_{SF} + \Delta V_{reset} + \Delta V_{SFnoise} + A_{SF}(\Delta t)V_{PD}(\Delta t)\right) \text{ [V]}, \end{aligned} \tag{58}$$

where ΔA_{SF}, ΔV_{reset} and $\Delta V_{SFnoise}$ are the difference in source follower gain, reset noise, and source follower noise, respectively, before and after integration time, and A_{CDS} is the CDS gain. Currently in ASSET, a CDS compensation factor, α, is used to reduce the reset noise and source follower noise, or the user can disable the noises (in the ASSET configuration file) that would have been removed by the CDS instead (e.g. offset FPN). In ASSET, the total output voltage in the CDS circuit for CMOS sensors is modeled by a modified form of Willers' [6] model as

$$V_{CDS}^{CMOS} = A_{CDS}\left(V_{ref}\Delta A_{SF}^{nl} + \alpha\left(V_{reset} + V_{SFnoise}\right) + A_{SF}^{nl}\frac{qn_{PD}}{C_{SN}^{nl}}\right) \text{ [V]}, \tag{59}$$

where $qn_{PD}/C_{SN}^{nl} = V_{PD}$, α is the CDS compensation factor, A_{SF} is the source follower gain, and Δt has been dropped for conciseness. Depending on the pixel architecture some of the noise values will be increased, some will be reduced, and some will be canceled out. See [26] for more information on how the CDS circuit deals with different noise sources for different CMOS pixel architectures.

If the source follower gain is linear, as in the case of CCD sensors, the difference in source follower gain, ΔA_{SF}, is equal to zero and as a result the reference voltage, V_{ref}, goes away. In CCD sensors, the output voltage from the CDS circuit is expressed as

$$V_{CDS}^{CCD} = A_{CDS}\left(\alpha\left(V_{reset} + V_{SFnoise}\right) + A_{SF}\frac{qn_{PD}}{C_{SN}}\right) \text{ [V].} \tag{60}$$

3.8 Analog to Digital Conversion (ADC)

The image frame, whose signal is now in units of voltage and includes most noise sources, is quantized by multiplying the signal by the ADC conversion gain, A_{ADC}. In ASSET, the user provides the number of bits, *bits*, which defines the conversion gain as:

$$A_{ADC} = \frac{2^{bits} - 1}{V_{\max}} \text{ [counts / V].} \tag{61}$$

The maximum quantifiable voltage is obtained as $V_{max} = A_{CDS}A_{SF}qn_{fw}/C_{SN}$where n_{fw} is the full-well capacity in the sense node capacitor, C_{SN}, A_{SF} is the linear source follower gain, and A_{CDS} is the CDS gain. In the case of CMOS, the non-linear gains and sense node capacitance are necessary to estimate the maximum quantifiable voltage by the ADC. The resulting voltage signal from the CDS is multiplied by the ADC gain, A_{ADC}, and rounded down to obtain the digital signal in counts:

$$DN_{ADC} = \left\lfloor \left(V_{CDS} + V_{bias}\right) A_{ADC} \right\rfloor = \left\lfloor \frac{\left(V_{CDS} + V_{bias}\right)}{V_{\max}}\left(2^{bits} - 1\right) \right\rfloor \text{ [counts].} \tag{62}$$

Rounding the fractional count values down introduces quantization error (or *quantization noise*) [4]. In ASSET, quantization noise is implemented by directly converting the voltage signal to integer counts based on user-defined number of bits. In

addition, real systems will typically have a bias voltage, V_{bias}, that results in an equivalent count value referred to as *hardware offset*. In ASSET, the hardware offset represents this offset (or bias) of the system due to the system's electronics (i.e. *hardware*). It is included in ASSET as a bias term that does not contribute to photon or electron noise.

3.8.1 ADC Fixed Pattern Offset

CMOS image sensors originally operated with a single chip-level ADC when pixel arrays were small, and ADCs did not require much speed [27]. However, as pixel count continues to increase, this approach is too slow to be useful. For this reason, newer CMOS image sensors employ column-level ADCs where multiple ADCs operate in parallel and sometimes each share multiple columns. This results in lower power consumption, since each ADC can read the voltage signal at a lower speed [27]. Mismatches between column-level ADCs will cause a column-to-column offset FPN, which will also degrade the image sensor output signal. Therefore, CMOS modeling requires an additional column offset FPN component associated with the ADC circuit of the sensor. Similar to column offset FPN, ADC offset FPN is modeled as Gaussian process and is described by

$$DN_{FPN}(k) = X(k)\sigma_{FPN}^{ADC} \quad \text{[counts]}, \tag{63}$$

where X is an array of i.i.d. normal random variables with zero mean and unit variance, and k is the set of shared columns (or rows) index. The RMS ADC offset FPN noise is given by

$$\sigma_{FPN}^{ADC} = DN_{fW} D_N^{ADC} \quad \text{[counts]}, \tag{64}$$

where D_N^{ADC} is the column offset FPN quality factor (percentage of full-well digital signal DN_{fw}) and $DN_{fw} = 2^{bits} - 1$ is the digital signal corresponding to a full-well. The digital signal $DN_{FPN}(k)$ is replicated for every row to obtain an array of the appropriate size. ADC offset FPN is added and the output digital signal is

$$DN = \lfloor DN_{ADC} + DN_{FPN} \rfloor \text{ [counts].} \tag{65}$$

3.9 Improved Model Summary

The improved FPA and electronics model was implemented in MATLAB as part of the baseline ASSET model and improves the detector response and read-out electronics by replacing the baseline linear conversion gain from electrons to counts with an electronics component-based model based on Konnik's, Welsh's, and Willers' work [5, 6]; including non-linear effects observed in real sensors; and by implementing fixed-pattern noise (FPN) based on FPA architecture. These improvements are illustrated in the block diagram from Figure 13, illustrated again in Figure 20 (bottom) for convenience.

The improved FPA model covers conversion of photo-generated electrons to voltage and finally to digital numbers, whereas the baseline model directly converts the signal from electrons to counts using a linear conversion gain. It incorporates CDS, sense node and source follower components contributing to gain non-linearities.

Combining each of the pieces discussed in this chapter results in a complete analysis approach to a final end-to-end sensor process for the improved FPA model. Sensor output from processes modeled in the improved ASSET model can be represented as:

$$DN = \left\lfloor \frac{\left(2^{bits}-1\right)}{V_{\max}} \left(A_{CDS} \left(V_{SF}(\Delta t = 0) - \left(A_{SF}^{nl}\left(V_{SN}\right) \left(V_{ref} - \frac{qn_{PD}}{C_{SN}^{nl}\left(V_{SN}\right)} + \sigma_{reset} \right) + \sigma_{SF} + V_{FPN} \right) \right) + V_{bias} \right) + DN_{FPN} \right\rfloor \tag{66}$$

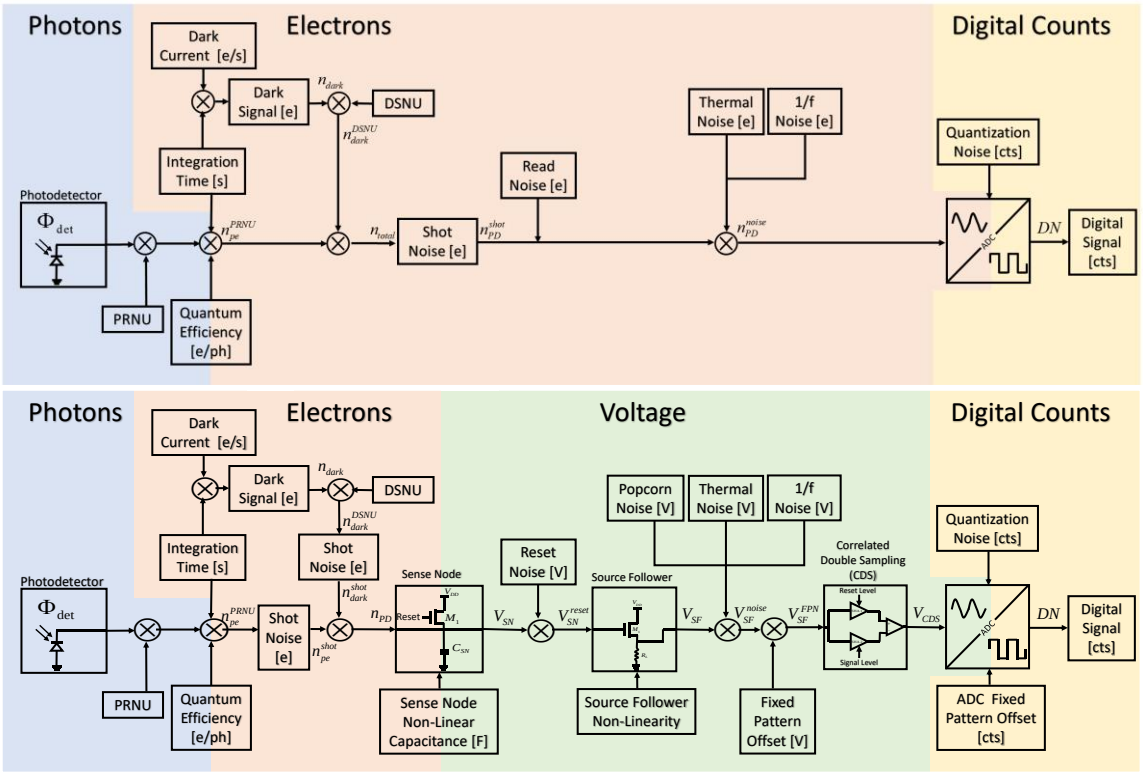

Figure 20. Process diagrams of the baseline (top) and improved (bottom) FPA models for a CCD and CMOS image sensor based on models by Konnik, Welsh, and Willers [5, 6].

for CMOS sensors and

$$DN = \left\lfloor \frac{\left(2^{bits}-1\right)}{V_{\max}} \left(A_{CDS} \left(V_{SF}(\Delta t = 0) - \left(A_{SF} \left(V_{ref} - \frac{q n_{PD}}{C_{SN}} + \sigma_{reset} \right) + \sigma_{SF} \right) \right) + V_{bias} \right) \right\rfloor \tag{67}$$

for CCD sensors, where

$$n_{PD} = \Delta t \left[P\left(\eta \phi_{\det} \left[1 + P_N N(0,1)\right]\right) + P\left(i_{dark} \left[1 + e^{D_N N(0,1)}\right]\right) \right]. \tag{68}$$

Table 6 contains a summary of all sensor parameters of the improved model and gives a brief description of each of the sensor parameters used indicating which parameters are used for either CCD, CMOS, or both. The additional input sensor parameters shown in Tables 1 through 5 contrast the improved model with the baseline

model by comparing the model parameters used for the detector, sense node, source follower, CDS, and ADC for the improved and the baseline model.

Table 1. Detector Model Parameters.

Baseline Model	**New Model**	**Significance**	**Comments**
Photon flux ϕ_{det} (Eq 5)	Photon flux ϕ_{det} (Eq 23)	No change	Total photon flux incident on the detector array
Quantum efficiency η (Eq 6)	Quantum efficiency η (Eq 24)	No change	Wavelength-independent quantum efficiency
Photoelectrons n_{pe} (Eq 6)	Photoelectrons n_{pe} (Eq 24)	No change	Electrons generated from incident photon flux during an integration time
PRNU $P(x,y)$ (Eq 8)	PRNU n_{pe}^{PRNU} (Eq 25)	No change	Photogenerated electrons with photo response non-uniformity (PRNU) included
Signal shot noise n_{signal}^{shot} (Eq 9)	Photon shot noise n_{pe}^{shot} (Eq 26)	Photo-generated shot noise is now computed separately from dark shot noise	In the new model, shot noise now depends on PRNU
Dark signal n_{dark} (Eq 7)	Dark signal n_{dark} (Eq 27)	Replaced arbitrary dark signal with physics-based model	Dependent on temperature, pixel area and detector material
DSNU n_{dark}^{DSNU} (Eq 7)	DSNU n_{dark}^{DSNU} (Eq 29)	Replaced Gaussian model with log-normal process	The log-normal model randomly introduces hot pixels in the sensor
Dark current RMS σ_{dark} (Eq 7)	Dark current RMS $\sigma_{dark} \equiv n_{dark} D_N$ (Eq 29)	Replaced arbitrary dark current RMS with model dependent on DSNU quality factor and dark current	Useful when the DSNU quality factor is known and it now depends on temperature and pixel size
Signal shot noise n_{signal}^{shot} (Eq 9)	Dark shot noise n_{dark}^{shot} (Eq 30)	Dark shot noise is now computed separately from photoelectron shot noise	Gives shot noise for dark signal only

Table 2. Sense Node Model Parameters.

Baseline Model	New Model	Significance	Comments
None	Sense node (Sec. 3.5)	New model includes conversion from electrons to volts, sense node non-linearity and reset noise	Useful when sensor is non-linear or when a voltage output is needed
None	Sense node non-linearity (Sec. 3.5.1)	New model includes sense node non-linearities caused by the sense node capacitance	CMOS sensor non-linearity can be as high as 200%
None	Reference voltage V_{ref} (Sec. 3.5)	In the new model the sense node is reset to V_{ref} before each measurement	Before integration time starts, the sense node is reset to a reference voltage V_{ref} in CCD and CMOS sensors
None	Sense node conversion gain A_{SN} (Sec. 3.5)	Added sense node conversion gain [V/e] to convert signal from electrons to counts	Linear in CCD sensors and non-linear in CMOS sensor
None	Sense node capacitance C_{SN} (Eq 32 & 34)	New model includes a linear and non-linear sense node capacitance	Linear in CCD sensors and non-linear in CMOS sensor; dependent on voltage signal and read-out circuitry
None	Sense node voltage V_{SN} (Eq 32)	Provides a voltage output from the sense node proportional to the total number of electrons	Linear in CCD sensors and non-linear in CMOS sensor; dependent on reference voltage, gain, well capacitance, and type of sensor
Thermal noise $\sigma_{thermal}$ (Eq 10)	Reset noise V_{SN}^{reset} (Eq 37 & 38)	Replaced arbitrary thermal noise with physics-based model	Dependent on temperature and sense node capacitance

Table 3. Source Follower Model Parameters.

Baseline Model	New Model	Significance	Comments
None	Source follower (Sec. 3.6)	New model includes source follower gain, non-linearities, and noise dependent on read-out circuitry	Used to transfer the voltage from the sense node to the loading circuit to be further amplified and processed by the CDS
None	Source follower gain A_{SF} (Eq 40)	New model includes a linear and non-linear gain based on read-out circuit	Linear in CCD sensors and non-linear in CMOS sensor; dependent on sense node voltage
None	Source follower non-linearity (Sec. 3.6.1)	New model includes sense node non-linearity caused by the sense node capacitance	Only CMOS sensors
None	Source follower output voltage V_{SF} (Eq 41)	Provides a voltage output from the source follower proportional to the sense node voltage	Linear in CCD sensors and non-linear in CMOS sensor; dependent on gain and sense node voltage
Thermal noise $\sigma_{thermal}$ (Eq 10)	Source follower noise $V_{SFnoise}$ (Eq 43-47)	Replaced arbitrary thermal noise with physics-based model	Dependent on temperature and source follower resistance
Flicker noise $\sigma_{1/f}$ (Eq 12)	Source follower noise $V_{SFnoise}$ (Eq 43-47)	Replaced arbitrary flicker noise with physics-based model	Dependent on frequency and read-out circuitry; new model accounts for thermal, flicker and popcorn noise
None	Offset fixed pattern noise V_{FPN} (Eq 48)	Adds pixel-to-pixel and column-to-column offset FPN component	Only present in CMOS sensors; due to differences in threshold voltages and column amplifiers

Table 4. Correlated Double Sampling Model Parameters.

Baseline Model	New Model	Significance	Comments
None	Correlated double sampling (CDS) (Sec. 3.7)	Adds implementation of the CDS method used on CCD and CMOS image sensor	Used to remove or reduce offset FPN and reset noise
None	CDS gain A_{CDS} (Eq 59 & 60)	Added new gain associated with the CDS circuit	Linear in both CCD and CMOS sensors
None	CDS output voltage V_{CDS} (Eq 59 & 60)	Provides an output voltage from the CDS dependent on CDS gain	If CDS is implemented, the offset FPN and reset noise will be reduced

Table 5. Analog-to-Digital Conversion (ADC) Model Parameters.

Baseline Model	New Model	Significance	Comments
ADC conversion gain CG [DN/e] (Eq 14)	ADC conversion gain A_{ADC} [DN/V] (Eq 61)	Replaced by conversion gain from volts to counts	New model accounts for non-linearities present in CMOS sensors
Digital signal DN (Eq 15 & 16)	Digital signal DN (Eq 65)	Digital signal is now obtained from a voltage signal	Dependent on read-out circuitry
None	ADC offset FPN DN_{FPN} (Eq 63)	Adds column-to-column offset FPN	Due to mismatches in column-level ADC channels
Hardware offset DN_{offset} (Eq 16)	Bias Voltage V_{bias} (Eq 62)	Bias voltage is now converted to counts and added as a hardware offset	Added before introducing quantization noise into the signal

Table 6. Summary of Model Parameters for the Improved Model.

Variable	Name	Units	Description	Sensor	
				CCD	CMOS
ϕ_{det} (Eq 23)	Detector photon flux	[ph/s]	Total photon flux incident on the detector array	✓	✓
Δt (Eq 24)	Integration time	[s]	Length of time during which detector is exposed to light	✓	✓
η (Eq 24)	Quantum efficiency	[e/ph]	Average fraction of photons that are converted to electrons by the detector	✓	✓
n_{pe} (Eq 24)	Photo-generated electrons	[e]	Electrons generated from incident photon flux during an integration time	✓	✓
n_{pe}^{PRNU} (Eq 25)	Photo-generated electrons after PRNU	[e]	Photogenerated electrons with photo response non-uniformity (PRNU) included	✓	✓
n_{pe}^{shot} (Eq 26)	Photo-generated electrons including shot noise	[e]	Photogenerated electrons with PRNU and shot noise included	✓	✓
n_{dark} (Eq 27)	Average dark signal	[e]	Average number of electrons present in every pixel when there is no illumination of the photodetector	✓	✓
n_{dark}^{DSNU} (Eq 29)	Dark signal after DSNU	[e]	Dark signal with dark signal non-uniformity (DSNU) included	✓	✓
n_{dark}^{shot} (Eq 30)	Dark signal including shot noise	[e]	Dark signal with DSNU and shot noise included	✓	✓
n_{PD} (Eq 31)	Photodiode electrons	[e]	The total number of electrons collected in the photodiode	✓	✓
V_{ref} (Eq 32)	Reference voltage	[V]	Voltage the sense node is reset to before an integration time	✓	✓
V_{bias} (Eq 65)	Bias voltage	[V]	Voltage applied to the bias transistor (M_b)	✓	✓
V_{PD} (Eq 32)	Photodiode Voltage	[V]	Voltage signal proportional to the electrons collected in the photodiode	✓	✓
C_{SN} (Eq 32)	Sense node capacitance	[F]	Linear sense node capacitance	✓	×
C_{SN}^{nl} (Eq 34)	Non-linear sense node capacitance	[F]	Non-linear sense node capacitance dependent on the sense node voltage (V_{SN})	×	✓
A_{SN}	Sense node conversion gain	[V/e]	Conversion gain from electrons to volts (q/C_{SN}) at the sensor node	✓	×
A_{SN}^{nl}	Non-linear sense node gain	[V/e]	Non-linear conversion gain from electrons to volts (q/C_{SN}^{nl})	×	✓

Variable	Name	Units	Description	Sensor	
				CCD	CMOS
V_{SN} (Eq 32)	Sense node voltage	[V]	Voltage across the sense node capacitor and is discharged from V_{ref} to some lower value	✓	✓
V_{reset} (Eq 37 & 38)	Reset noise voltage	[V]	Noise introduced when the sense node capacitor is reset	×	✓
V_{SN}^{reset} (Eq 39)	Sense node voltage with reset noise included	[V]	Sum of the sense node voltage and the reset noise voltage	×	✓
A_{SF} (Eq 40)	Source follower gain	[V/V]	Linear source follower gain used for CCD sensors (usually equal to one)	✓	×
A_{SF}^{nl} (Eq 42)	Non-linear source follower gain	[V/V]	Non-linear source follower gain used for CMOS sensors that depends on the sense node voltage (V_{SN})	×	✓
V_{SF} (Eq 41)	Source follower voltage	[V]	Output voltage from the source follower	✓	✓
$V_{SFnoise}$ (Eq 47)	Source follower noise	[V]	All noise associated with the source follower. These include thermal, flicker and popcorn noise.	✓	✓
V_{FPN}^{col} (Eq 49)	Column-to-column offset fixed pattern noise (FPN)	[V]	Column offset FPN due to variations in bias current in the bias transistor (M_b)	×	✓
V_{FPN}^{pix} (Eq 51)	Pixel-to-pixel offset FPN	[V]	Pixel offset FPN due to variations in threshold voltages in M_1, M_2, and M_3.	×	✓
V_{FPN} (Eq 48)	Offset FPN voltage	[V]	Sum of the column and pixel offset FPN components	×	✓
V_{SF}^{FPN} (Eq 53)	Source follower voltage signal with noise and offset FPN	[V]	Sum of the output source follower voltage with noise and the offset FPN voltage	×	✓
A_{CDS} (Eq 59 & 60)	Correlated double sampling (CDS) gain	[V/V]	Gain associated with the CDS circuit	✓	✓
V_{CDS} (Eq 59 & 60)	CDS voltage signal	[V]	Output voltage from the CDS circuit	✓	✓
A_{ADC} (Eq 61)	Analog-to-digital converter (ADC) gain	[counts/V]	Gain associated with the ADC circuit	✓	✓
DN (Eq 65)	Digital signal	[counts]	Output digital signal from the ADC circuit	✓	✓
DN_{FPN} (Eq 63)	ADC Offset FPN signal	[counts]	Shared columns offset FPN	×	✓

4 Experiment Methodology

This chapter presents the laboratory experiments conducted using a Phantom camera, describes configuration of the ASSET model used to generate synthetic test data for validation against measured CMOS data, and discusses the process of generating a photon transfer curve (PTC) and a dark transfer curve (DTC) that are used to analyze the results. Chapter 5 compares the performance of ASSET with the improved FPA model to data collected in the laboratory measurements, and the validation results are analyzed.

4.1 Experimental Setup

The sensor model described in Chapter 3 has been validated using a Vision Research Phantom v12.1 high-speed camera with a 1280 x 800 CMOS technology FPA with a 20 µm pixel. The camera is designed for high speed operation and is capable of taking 1,000,000 frames-per-second (fps). The parameters used in the model of the CMOS sensor were taken in part from the specifications provided by the manufacturer, and the remainder were derived from photon transfer curves (PTCs) and dark transfer curves (DTCs) obtained in the lab (see Table 7). In PTC and DTC plots, the RMS noises are plotted as a function of signal level. These plots can be used to estimate the read noise, shot noise, FPN (DSNU, PRNU, and offset FPN components), and saturation level for an image sensor directly from the data. Read noise is defined here as the collection of noise terms (reset and source follower) that contribute random fluctuations to output signal at zero integration time. Noise measurements are obtained in digital units (counts) and converted to electrons for use as parameters in ASSET.

During a PTC measurement, the image sensor is exposed to a uniform light source which provides a uniform illumination field, also called flat frame, as shown in Figure 21. The uniform light source is obtained by using an integrating sphere. The integrating sphere provides a 99% uniform field at the output port so that the photons collected by the image sensor are uniform across the FPA [28]. The averaged dark frame is subtracted from the flat frames to remove dark current noise such as DSNU, offset FPN, and the hardware offset. Subtracting the averaged dark from the flat frames yields the signal frames equivalent to the input photon-flux. The averaged dark frame is determined from several dark frames that are averaged to reduce read and shot noise. During a dark frame measurement, the image sensor is completely covered using the lens cap.

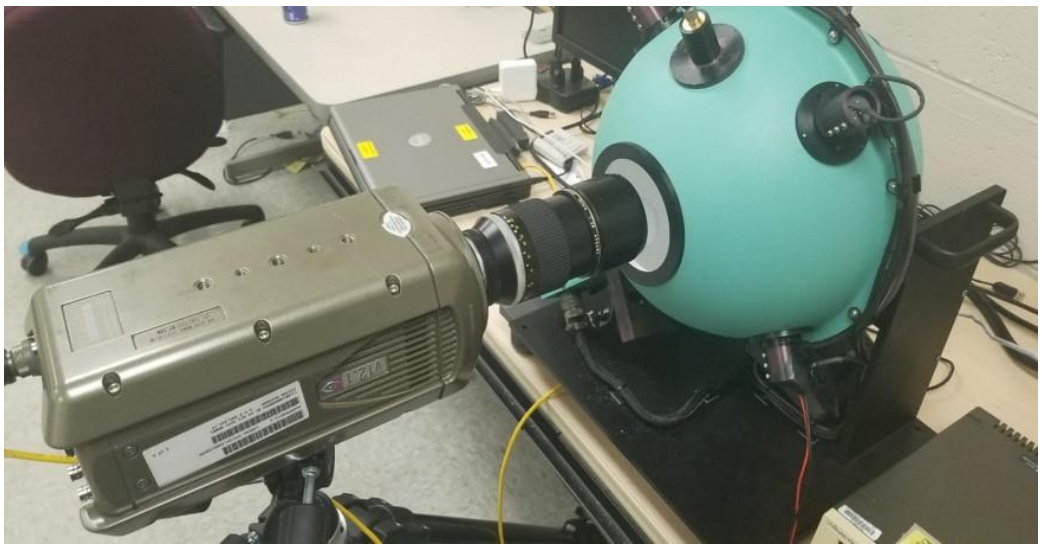

Figure 21. Phantom v12.1 experimental setup

These measurements were made over a range of integration times to cover the whole dynamic range of the image sensor. A grid of 512x512 pixels comprises each frame. We took 500 frames and averaged them to reduce temporal noise. The mean and standard deviation of each measurement were calculated and plotted to obtain the PTC. The PTC

can be used to determine the shot noise, PRNU, read noise, full-well capacity, and the conversion gain from electrons to counts, *CG*. Conversion gain, *CG*, is defined here as the combined product of the sense node, source follower, CDS, and ADC gains: $CG = A_{SN}A_{SF}A_{CDS}A_{ADC}$ [e / counts]. The methods and procedures of the measurement were the same for the measured and the simulated sensor. For example, for the image sensor, an integrating sphere forms a flat-field scene of incident light. For the modeled data, a uniform image was used to represent a flat-field scene.

During a DTC measurement, only the dark frames are used, and the dark signal is varied by changing the integration time of the image sensor. The DTC can be used to determine the dark shot noise, DSNU, offset FPN, read noise, the dark current figure of merit, D_{FM}, and the conversion gain from electrons to counts. These measurements were conducted at room temperature (25^{o}C) and the sensor and camera were kept at a temperature of 35^{o}C and 42^{o}C, respectively. The following sections discuss the procedures on how to generate a PTC and a DTC, and how to interpret the curves to obtain noise and detector characteristics.

4.2 Dark and Flat Frames

A dark frame is an image captured when there is no incident light on the image sensor, hence the name *dark frame*. During a dark frame measurement, the image sensor is completely covered. To obtain the dark frame, we measure the pixel output values for an image sensor array of N_{pix} pixels under constant temperature with the lens cap on. The dark frame will contain the dark current, DSNU, dark shot noise, offset FPN, read noise, and hardware offset. We repeated this measurement N_F times to obtain N_F dark frames

and averaged them to reduce read and shot noise from the output values as shown in Figure 22. That is,

$$DARK_{ij}(DN) = \frac{1}{N_F}\sum_{k=1}^{N_F} dark_{ijk}(DN)\ [\text{counts}], \tag{69}$$

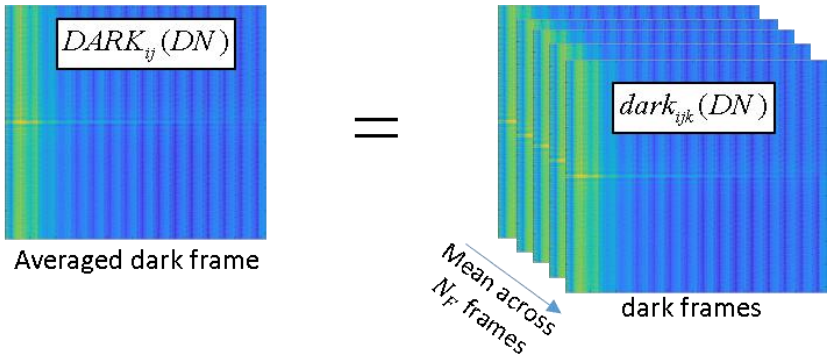

Figure 22. Illustration showing how the averaged dark frame is obtained by averaging 500 frames.

where $DARK_{ij}(DN)$ is the averaged dark signal value of pixel (i,j) in the dark frame, which is based on N_F dark frames of N_{pix} pixels, and $dark_{ijk}(DN)$ is the kth dark signal value of pixel (i,j), where the full set of N_{pix} pixels is the kth dark frame.

A flat frame is an image captured when the image sensor is exposed to a uniform light source, which provides a uniform illumination frame. To obtain the flat frame we measure the pixel output values for an image sensor array of N_{pix} pixels under uniform illumination. The flat frame will contain photogenerated shot noise, PRNU, read noise and dark current noise and offsets such as DSNU, dark shot noise, offset FPN, and hardware offset. Similar to dark frames, we repeat this measurement N_F times to obtain N_F flat frames and averaged them to reduce read and shot noise as shown in Figure 23. The averaged flat frame value in pixel (i,j) is given by,

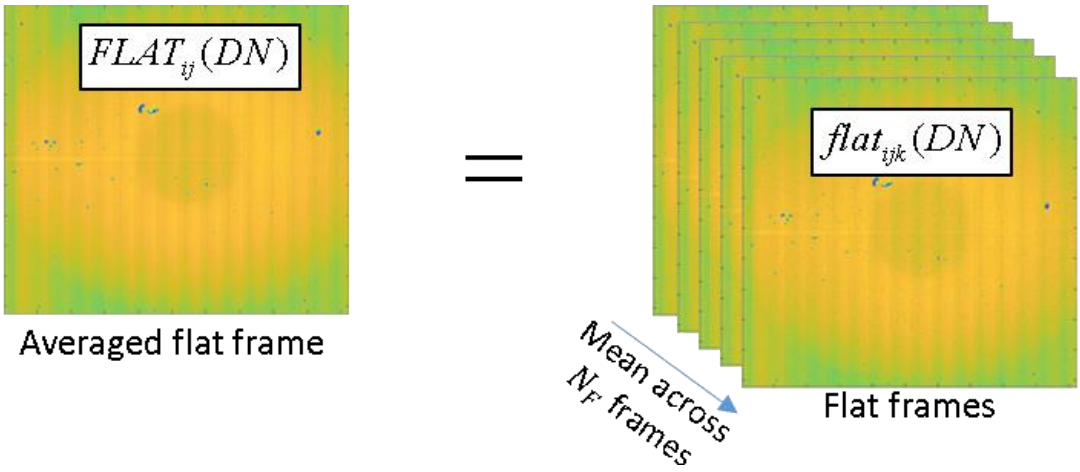

Figure 23. Illustration showing how the averaged flat frame is obtained by averaging 500 flat frames.

$$FLAT_{ij}(DN) = \frac{1}{N_F}\sum_{k=1}^{N_F} flat_{ijk}(DN) \quad \text{[counts]}, \tag{70}$$

where $FLAT_{ij}(DN)$ is the averaged flat frame pixel value of pixel (i,j) in the flat frame, which is based on N_F flat frames of N_{pix} pixels, and $flat_{ijk}(DN)$ is the kth flat signal value of pixel (i,j), where the full set of N_{pix} pixels is the kth flat frame. For comparison, Figure 24 shows an averaged dark frame (left) and an averaged flat frame (right) from the Phantom v12.1 camera.

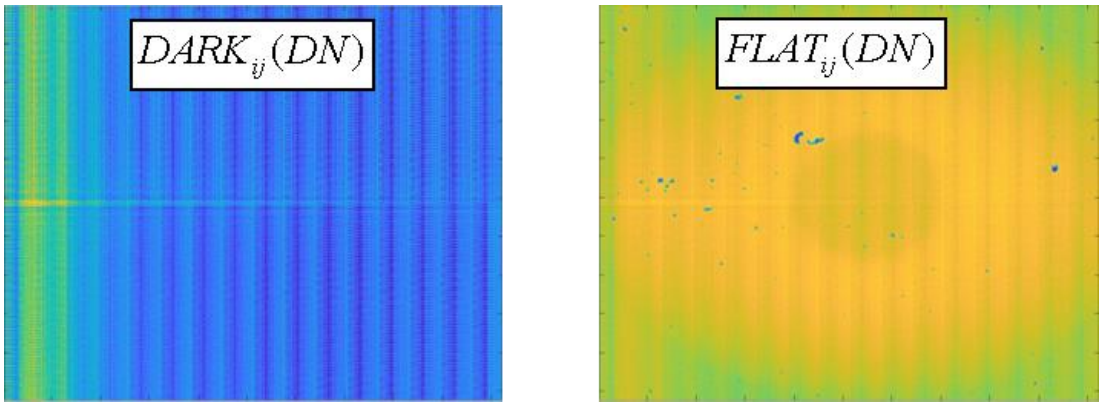

Figure 24. Measured dark frame (left) and measured flat frame (right) at Δt = *3* ms.

4.3 Photon Transfer Curve (PTC)

The PTC is a log-log plot of the noise standard deviation versus signal used to determine parameters of an image senor's response to uniform illumination. These parameters are: photoelectron shot noise, PRNU, read noise, conversion gain, and full-well capacity. Figure 25 shows an ideal PTC from an image sensor exposed to uniform illumination. In the plot, noise is plotted as a function of the mean average signal at different exposure times (or signal levels) [7]. Janesick identifies four different regimes in a PTC plot: read noise, shot noise, FPN, and full-well regime [7].

For very low signal, the read noise dominates, which is the random noise measured in dark conditions. In a PTC log-log plot, read noise is often characterized by a line with a slope of zero. As the signal increases, the photoelectron shot noise dominates and is characterized by a slope of one-half, since the shot noise is equal to the one-half power of the average number of photoelectrons. The third regime, FPN, represents the PRNU produced by photoelectrons, which is characterized with a slope of one since signal and FPN increase at the same rate. Finally, in the fourth regime, as the signal approaches full-well, noise starts to decrease exponentially. This is because photoelectrons start to spill into neighboring pixels and as a result the number of noise electrons starts to decrease.

To determine the average digital signal corresponding to the input photon-flux, the dark signal is removed from the flat frame values by subtracting pixel by pixel the averaged dark signal frame from the flat frames. By subtracting the averaged dark frame from the flat frames, you are basically removing the DSNU, offset FPN, and hardware offset as shown in Figure 26. Thus,

$$S_{ijk}(DN) = flat_{ijk}(DN) - DARK_{ij}(DN) \quad \text{[counts]}, \tag{71}$$

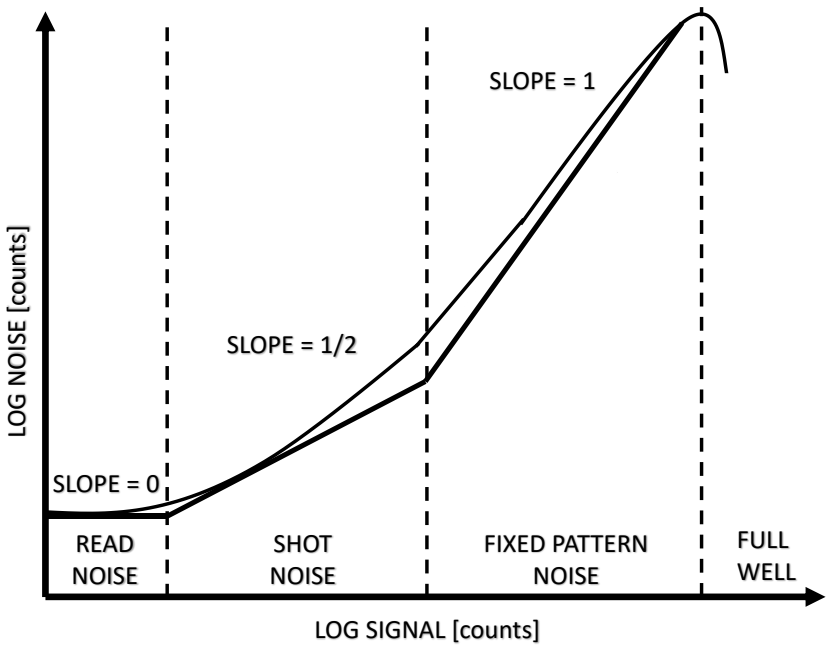

Figure 25. Ideal PTC plot illustrating the four noise regimes [7, 29].

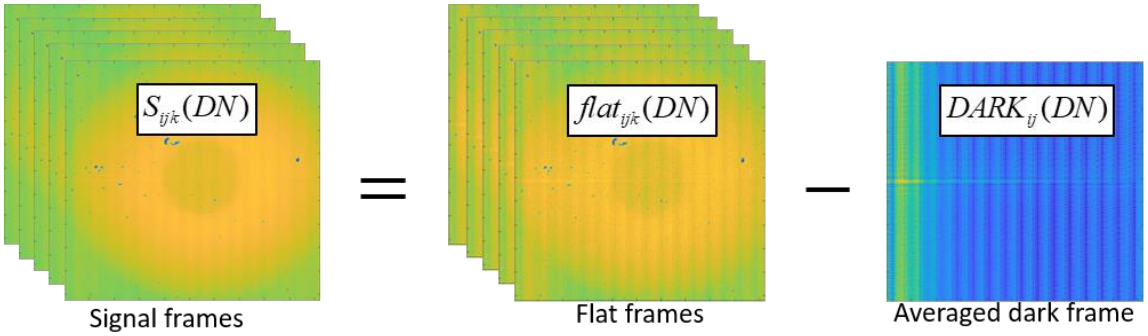

Figure 26. Illustration showing how the signal frames are obtained by subtracting an averaged dark frame from the flat frames.

where $S_{ijk}(DN)$ is the kth signal of the (i,j)th pixel in the frame of N_{pix} pixels. Each set of dark and flat frames is obtained for the same integration time, but the integration time is varied from set to set to cover the whole dynamic range of the image sensor. After removing the DSNU and offset FPN, the mean average signal is calculated for each integration time to obtain the true photogenerated signal:

$$S(DN) = \frac{1}{N_{pix} N_F} \sum_{ij=1}^{N_{pix}} \sum_{k=1}^{N_F} S_{ijk}(DN) \quad \text{[counts]}, \tag{72}$$

where $S(DN)$ is the mean average signal based on N_{pix} pixels and N_F frames. The total noise is obtained by calculating the standard deviation of the pixel values from the signal frames calculated in Equation (71). Thus,

$$\sigma_{total}(DN) = \left(VAR\left[S_{ijk}(DN)\right]\right)^{1/2} = \left\{\frac{1}{N_{pix} N_F} \sum_{ij=1}^{N_{pix}} \sum_{k=1}^{N_F} \left[S_{ijk}(DN) - S(DN)\right]^2\right\}^{1/2} \quad \text{[counts]}, \tag{73}$$

where $\sigma_{total}(DN)$ is the total noise (shot noise, PRNU, and read noise) and $S_{ijk}(DN)$ is the kth signal of pixel (i,j). This is repeated at several integration times spanning the full dynamic range of the image sensor. An ideal PTC response from an image sensor is illustrated in Figure 27.

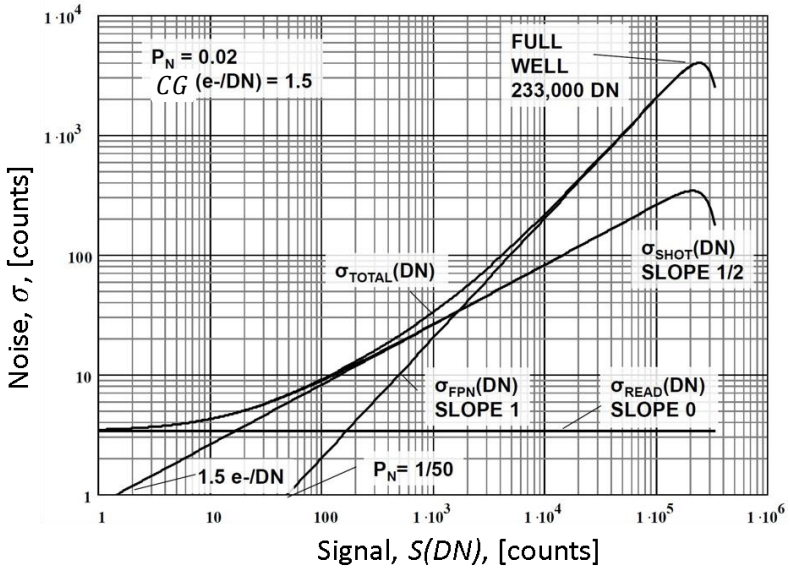

Figure 27. Ideal PTC plotted in counts [7].

In the plot the noise is plotted as a function of the mean average signal $S(DN)$ at different signal levels (or integration times). The total noise is also found by the

quadrature sum of read noise, shot noise, and PRNU. Therefore, the total noise is also given by

$$\sigma_{total}(DN) = \left[\sigma_{read}^2(DN) + \sigma_{shot}^2(DN) + \sigma_{PRNU}^2(DN)\right]^{1/2} \text{ [counts].} \quad (74)$$

To calculate the shot and read noise we first must remove the FPN from the array of pixels. This is done by differencing two identical frames taken back-to-back at the same integration time as illustrated in Figure 28. The shot plus read noise frames are given by

$$S_{ijk}^{shot+read}(DN) = flat_{ijk}(DN) - flat_{ij(k+1)}(DN) \text{ [counts],} \quad (75)$$

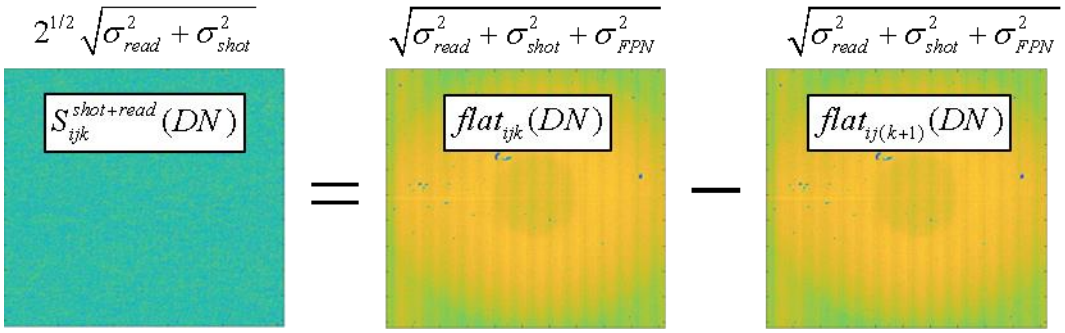

Figure 28. Illustration showing how fixed-pattern noise is removed by subtracting two back-to-back frames.

where $S_{ijk}^{shot+read}(DN)$ is the kth shot plus read noise frame pixel (i,j) pixels. By subtracting identical frames taken back-to-back, the PRNU, DSNU and offset FPN are removed from the output signal. The total shot plus read noise is obtained by calculating the standard deviation of the shot plus read noise frames from Equation (75) [7]. In addition, the result should be divided by $2^{1/2}$ because random noise increases by this amount when either adding or subtracting two identical frames with random noise [7]. Thus, the shot plus read noise is given by

$$\sigma_{shot+read}(DN)=\frac{\left\{\frac{1}{N_{pix}N_F}\sum_{ij=1}^{N_{pix}}\sum_{k=1}^{N_F}\left(S_{ijk}^{shot+read}(DN)-E\left[S_{ijk}^{shot+read}(DN)\right]\right)^2\right\}^{1/2}}{2^{1/2}} \text{ [counts]}, \quad (76)$$

where $\sigma_{\text{shot+read}}(DN)$ is the standard deviation of the shot plus read noise frames, $S_{ijk}^{shot+read}(DN)$, divided by $2^{1/2}$. If the read noise is known, the two components from Equation (76) can be isolated by subtracting the read noise from the shot plus read noise, $\sigma_{\text{shot+read}}(DN)$.

The read noise can be obtained from bias frame analysis. To capture a bias frame, images need to be obtained at zero integration time (or as close as possible) with the lens cap on. Furthermore, the read noise can also be estimated from the PTC and is determined from the read noise regime where the slope is equal to zero. Since noise sources are added in quadrature, shot noise is simply obtained by subtracting the read noise from the read plus shot noise. Therefore, the shot noise is given by

$$\sigma_{shot}(DN)=\left[\sigma_{shot+read}^2(DN)-\sigma_{read}^2(DN)\right]^{1/2} \text{ [counts]}. \quad (77)$$

Once the shot noise has been calculated, the conversion gain from electrons to counts can be determined. The conversion gain from electrons to counts can be calculated from the shot noise curve shown in Figure 27 and is given by

$$CG=\frac{S(DN)}{\sigma_{shot}^2(DN)} \text{ [}e\text{/counts]}, \quad (78)$$

where $S(DN)$ is the mean average signal.

PRNU can be calculated by subtracting the read and shot noise, $\sigma_{\text{shot+read}}(DN)$, from the total noise, $\sigma_{total}(DN)$. The PRNU quality factor, P_N, is found from a single

data point in the PRNU curve by dividing the PRNU noise with the mean average signal, $S(DN)$. The PRNU quality factor is given by

$$P_N = \frac{\sigma_{PRNU}(DN)}{S(DN)} \quad \text{[counts]}. \tag{79}$$

Furthermore, if the PRNU quality factor, P_N, and the conversion gain, CG, are known, individual PTCs for shot noise and PRNU can be calculated. For example, by applying Equation (79), the PRNU noise is given by

$$\sigma_{PRNU}(DN) = P_N S(DN) \quad \text{[counts]}, \tag{80}$$

and from Equation (78), shot noise is given by

$$\sigma_{shot}(DN) = \left[\frac{S(DN)}{CG}\right]^{1/2} \quad \text{[counts]}. \tag{81}$$

Once the conversion gain has been calculated, the noise and signal can be converted into electron units. It should be noted that for non-linear sensors the shot noise and FPN will not follow a slope of one-half and one, respectively, indicating that the conversion gain is non-linear [7].

4.4 Dark Transfer Curve (DTC)

The DTC is a log-log plot of the noise standard deviation versus dark signal used to determine parameters of an image senor's response when there is no illumination in the image sensor. These parameters are: dark shot noise, DSNU, offset FPN, read noise, dark current figure of merit D_{FM}, and conversion gain, *CG*. The type of measurements made in DTCs are very similar to those from a PTC plot with the exception that in a DTC curve all measurements are related to the dark signal. For example, in the PTC plot shown in

Figure 25, the four regimes are read noise, photogenerated shot noise, PRNU, and full-well; whereas in a DTC plot the four regimes are read noise, dark shot noise, DSNU, and full-well. An ideal PTC response from an image sensor is illustrated in Figure 29.

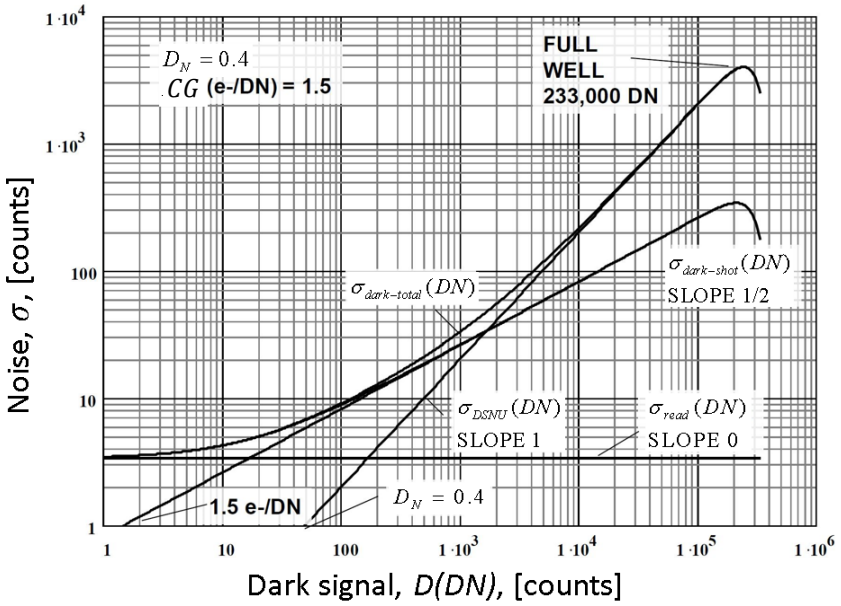

Figure 29. Ideal DTC plotted in counts [7].

For very low signal, the read noise dominates, which is the random noise measured under dark conditions. Similar to a PTC log-log plot, in a DTC log-log plot, read noise is often characterized by a line with a slope of zero. As the signal increases, the dark shot noise dominates. Dark shot noise is characterized by a slope of one-half since the dark shot noise is equal to the one-half power of the average number of dark electrons. The third regime, FPN, represents the DSNU produced by the dark signal, which is characterized with a slope of one since signal and DSNU increase at the same rate. Finally, in the fourth regime, as the signal approaches full-well, noise starts to decrease exponentially. This is because electrons start to spill into neighboring pixels and as a

result the number of noise electrons starts to decrease. It should be noted that in a DTC plot the fourth regime is rarely plotted, since dark current could take minutes or even hours to completely saturate the image sensor and will need a very long integration time to fully reach the full-well level.

The averaged bias frame is subtracted from the dark frames to remove dark offsets such as, offset FPN, and the hardware offset. Subtracting the averaged bias frame from the dark frames yields the dark signal frames equivalent to the total number of dark electrons. The average bias frame is calculated to reduce the shot and read noise to a value close to zero as illustrated in Figure 30. Thus,

$$D_{ijk}(DN) = dark_{ijk}(DN) - BIAS_{ij}(DN) \quad \text{[counts]}, \tag{82}$$

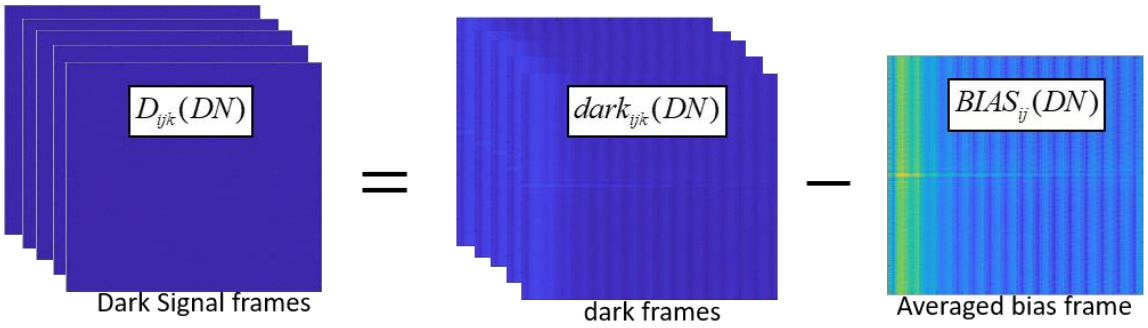

Figure 30. Illustration showing how the dark signal frames are obtained by subtracting an averaged bias frame from the dark frames.

where $D_{ijk}(DN)$ is the kth dark signal in the pixel at row and column coordinates (i,j), $BIAS_{ij}(DN)$ is the averaged bias frame based on N_F dark frames for each of the N_{pix} pixels, and $dark_{ijk}(DN)$ is the kth dark value in pixel (i,j). The full set of N_{pix} pixels' dark signal values is the dark frame. Each set of dark frames is made for the same

integration time, but the integration time is varied from set to set to cover the whole dynamic range.

To capture the bias frame's pixel values, $bias_{ijk}(DN)$, all the frames need to be obtained at zero integration time (or as close as possible) with the lens cap on. When integration time is close to zero, the dark shot noise and DSNU components are negligible, and the frames will only contain offset FPN and the hardware offset. By subtracting the averaged bias frame from the dark frame, the offset FPN and hardware offset are essentially removed from the dark signal. After removing the offset FPN and hardware offset, the mean average dark signal is calculated for each integration time to obtain the true thermally generated dark signal:

$$D(DN) = \frac{1}{N_{pix} N_F} \sum_{ij=1}^{N_{pix}} \sum_{k=1}^{N_F} D_{ijk}(DN) \quad \text{[counts]}, \tag{83}$$

where $D(DN)$ is the mean average dark signal based on N_{pix} pixels. The total dark noise is obtained by calculating the standard deviation of the pixel values from the dark signal frames calculated in Equation (82). Thus,

$$\sigma_{dark-total}(DN) = \left\{ \frac{1}{N_{pix} N_F} \sum_{ij=1}^{N_{pix}} \sum_{k=1}^{N_F} \left[D_{ijk}(DN) - D(DN) \right]^2 \right\}^{1/2} \quad \text{[counts]}, \tag{84}$$

where $\sigma_{dark-total}(DN)$ is the total dark noise (dark shot noise, DSNU, and read noise) and $D_{ijk}(DN)$ is the kth dark signal frame of pixel (*i*,*j*). This is repeated for integration times spanning the full dynamic range of the image sensor. In the plot from Figure 29, the total noise, $\sigma_{dark-total}(DN)$, has been plotted as a function of the mean average dark signal, $D(DN)$, at different signal levels (or integration times). The total dark noise is

also found by the quadrature sum of read noise, dark shot noise, and DSNU. Therefore, the total dark noise is also given by

$$\sigma_{dark-total}(DN) = \left[\sigma^2_{read}(DN) + \sigma^2_{dark-shot}(DN) + \sigma^2_{DSNU}(DN)\right]^{1/2} \text{ [counts].} \quad (85)$$

To calculate the dark shot and read noise we first must remove the DSNU from the array of pixels. This is done by differencing two identical frames taken back-to-back at the same integration time as shown in Figure 30. The dark shot plus read noise frames are given by

$$D^{shot+read}_{ijk}(DN) = dark_{ijk}(DN) - dark_{ij(k+1)}(DN) \text{ [counts],} \quad (86)$$

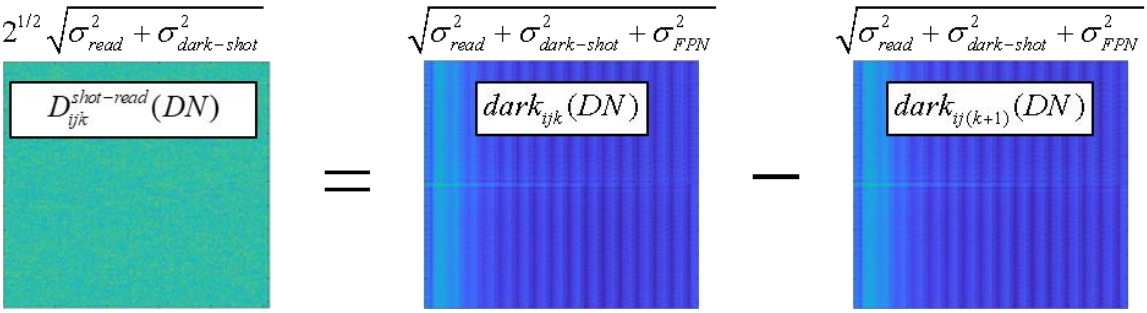

Figure 31. Illustration showing how fixed-pattern noise is removed by subtracting two consecutive frames.

where $D^{shot+read}_{ijk}(DN)$ is the kth dark shot plus read noise of the (i,j) pixel in the frame of N_{pix} pixels. By subtracting identical frames taken back-to-back, the DSNU, offset FPN and the hardware offset are removed from the output signal. Similar to the shot plus read noise calculated in Equation (76), the total dark shot plus read noise is obtained by calculating the standard deviation of the dark shot plus read noise frames from Equation (86) and then dividing by $2^{1/2}$. Thus, the dark shot plus read noise is given by

$$\sigma_{dark-shot+read}(DN)=\frac{\left\{\frac{1}{N_{pix}N_F}\sum_{ij=1}^{N_{pix}}\sum_{k=1}^{N_F}\left(D_{ijk}^{shot+read}(DN)-E\left[D_{ijk}^{shot+read}(DN)\right]\right)^2\right\}^{1/2}}{2^{1/2}}\ \text{[counts]}, \quad (87)$$

where $\sigma_{\mathrm{dark-shot+read}}(DN)$ is the standard deviation of the shot plus read noise frames' pixel values, $D_{ijk}^{shot+read}(DN)$, divided by $2^{1/2}$. If the read noise is known, from bias frame analysis or from DTC plot when slope is zero, the dark shot noise component can be isolated by subtracting the read noise. Therefore, the dark shot noise is given by

$$\sigma_{dark-shot}(DN)=\left[\sigma_{dark-shot+read}^2(DN)-\sigma_{read}^2(DN)\right]^{1/2}\ \text{[counts]}. \quad (88)$$

Once the dark shot noise has been calculated, the conversion gain from electrons to counts can be determined. The conversion gain from electrons to counts can be calculated from the dark shot noise curve and is given by

$$CG=\frac{D(DN)}{\sigma_{dark-shot}^2(DN)}\ \ [e/\text{counts}], \quad (89)$$

where $D(DN)$ is the mean average dark signal. In the same manner as dark shot noise, DSNU can be calculated by subtracting the read and dark shot noise from the total dark noise from Equation (85). The DSNU quality factor, D_N, is found from a single data point in the DSNU curve by dividing the DSNU noise with the mean average dark signal. The DSNU quality factor is given by

$$D_N=\frac{\sigma_{DSNU}(DN)}{D(DN)}. \quad (90)$$

Furthermore, if the DSNU quality factor, D_N, and the conversion gain, CG, are known, individual DTCs for shot and DSNU can be calculated. For example, by applying Equation (90), the DSNU noise is given by

$$\sigma_{DSNU}(DN) = D_N D(DN) \quad [\text{counts}], \tag{91}$$

and from Equation (89), dark shot noise is given by

$$\sigma_{dark-shot}(DN) = \left[\frac{D(DN)}{CG}\right]^{1/2} \quad [\text{counts}]. \tag{92}$$

Once the conversion gain has been calculated, the noise and signal can be converted into electron units. It should be noted that in DTC measurements integration time should be long enough to have meaningful results. For example, for a sensor with a full-well of 200,000 electrons and a dark current of 2,000 electrons per second, it will take about 100 seconds to reach full-well performance. The DTC dark current in electrons is given by

$$n_{dark} = CG \times D(DN) \quad [e], \tag{93}$$

where n_{dark} is the mean average dark signal in electrons. The dark current figure of merit, D_{FM}, is found using Equation (27) and solving for D_{FM}. Thus,

$$D_{FM} = \frac{CG \times D(DN)}{2.55 \cdot 10^{15} \Delta t A_{pix} T^{3/2} e^{-E_g/2kT}} \quad [\text{nA/cm}^2], \tag{94}$$

where Δt is the integration time (s), A_{det} is the pixel's area (cm^2), T is the temperature in Kelvin, E_g is the bandgap energy of the semiconductor (eV), k is Boltzmann's constant and D_{FM} is the dark current figure-of-merit (nA/cm^2).

The parameters obtained from the PTC and DTC plots as well as the parameters obtained from the specifications provided by the manufacturer were used in the simulation of the CMOS sensor using MATLAB. A performance comparison of the new sensor model to data collected in lab from the Phantom v12.1 and the validation of the sensor model are presented in Chapter 5.

5 Results and Discussion

The ASSET sensor model described in Chapter 3 is validated using a Vision Research Phantom v12.1 high-speed camera with a 1280 x 800 CMOS technology FPA with a 20 µm pixel size. We compare the image sensor and dark signal responses to incident light at various integration times. We also compare the noise as a function of integration time between the measured data, the improved, and the baseline sensor model. FPN evaluation demonstrates the noise characteristic similarity between the improved sensor model and the measured data.

The goal is to provide a sensor model capable of generating realistic synthetic data, representative of a wide range of systems, even with incomplete information. The purpose of this comparison was to demonstrate that ASSET can effectively model focal plane characteristics of an image sensor. The lab test quantifies how well ASSET can emulate time-varying and signal-dependent sensor characteristics, such as shot noise, FPN, and sensor non-linearity.

5.1 Validation of the Sensor Model

The parameters used in the model of the CMOS sensor are taken in part from the specifications provided by the manufacturer. The remainder are derived from photon transfer curves (PTCs) and dark transfer curves (DTCs) obtained in the lab (see Table 7). The simulated CMOS sensor covers conversion of photo-generated electrons to voltage or current and then to digital numbers. It incorporates sense node and source follower gain non-linearity, and it includes noise sources associated with the detector and electronics such as shot, thermal, 1/f, and quantization noise.

The methods used to generate the PTC and DTC measurements described in Chapter 4 were the same for both the measured data and the sensor model. In PTC and DTC plots, the RMS noises are plotted as a function of signal level. These plots can be used to estimate the read noise, shot noise, net FPN (DSNU, PRNU, and offset FPN components), and saturation level for an image sensor directly from the data. Again, read noise is defined here as the collection of noise terms (reset and source follower) that contribute random fluctuations to output signal at zero integration time. Noise measurements are obtained in digital units (counts) and converted to electrons for use as parameters in ASSET.

5.2 Sensor Response to Incident Light and Photon Transfer Curve (PTC)

The image senor response to incident light is calculated and compared to the sensor model output data. An integrating sphere forms a flat-field scene of incident light. Covering the lens provides dark frames. The model uses uniform images to represent a flat-field scene. An array of zeros mimics the image sensor with the lens cap on.

Taking images over a range of integration times covers the whole dynamic range of the photodetector. A grid of 512x512 pixels comprises each image. Two sets of 500 frames are taken (for both measured and sensor model): flat and dark frames. To reduce temporal noise (e.g. shot and read noise), we compute the mean frame for the two sets of data at each integration time, obtaining the averaged flat and dark frames. The averaged dark frame is subtracted from the flat frames to remove dark current noise such as DSNU, offset FPN, and the hardware offset. Subtracting the averaged dark from the flat frames yields the signal frames equivalent to the input photon-flux in each pixel, $S_{ijk}(DN)$.

Table 7. Phantom v12.1 Sensor's Parameters used for the simulation: Manufacturer-provided parameters (top) and experimentally derived parameters (bottom).

Manufacturer Parameters		
Sensor's Parameter	**Value**	**Comments**
Sensor Type	CMOS	The architecture type was not provided by the manufacturer
Array Size, *n* x *m*	1280 x 800	The resolution and pixel size results in a 25.6 mm x 16 mm array size
Pixel Dimension, *d*	20 µm	
Fill Factor, *FF*	56%	Light sensitive part of pixel
Well Depth, n_{fw}	23200 e	Saturation level in the sense node
Dynamic Range, *DR*	58 dB	Provided by the manufacturer
Quantum efficiency, η	31%	At 350 nm wavelength
Reference Voltage	3.3 V	Voltage that the sense node is reset to before an integration time

Experimentally derived Parameters		
Sensor's Parameter	**Value**	**Comments**
Read Noise, σ_{read}	18 *e*	Read noise RMS at 35ºC
Dark Current, i_{dark}	775 *e*/s	Average value of dark current of the whole pixel array at 35ºC
PRNU Factor, P_N	0.05	%RMS of photogenerated signal
DSNU Factor, D_N	0.4	%RMS of dark signal
Pixel FPN Factor, D_N^{pix}	0.0015	%RMS of saturation signal in volts
Column FPN Factor, D_N^{col}	0.00073	%RMS of saturation signal in volts
ADC FPN Factor, D_N^{ADC}	0.00045	%RMS of saturation signal in counts
Conversion Gain, $CG = A_{SN}A_{SF}A_{CDS}A_{ADC}$	0.35 e/count	Combined product of $A_{SN}A_{SF}A_{CDS}A_{ADC}$ gains (non-linear)
Sense Node Gain, A_{SN}		
Source Follower Gain, A_{SF}	1	Decreases with signal (non-linear)
CDS Gain, A_{CDS}	1	Linear
Source Follower Non-Linearity Error, γ	0.99	Typically, 0.95 to 1.05
Bits	16 bits	Number of bits used to quantize the signal
Hardware Offset, DN_{offset}	460 counts	Signal offset due to the load bias voltage
ADC Shared Columns	32	ADCs operate in parallel and each share 32 columns

The mean digital signal, *S(DN)*, of the resulting 512x512 signal frames' pixels, $S_{ijk}(DN)$, is calculated and plotted for integration times spanning the full dynamic range of the image sensor (estimated to be 23,200 electrons). Figure 32 shows a comparison between the measured and simulated data for the baseline and the non-linear model. The figure illustrates how the model starts linearly at low signals and introduces non-linear behavior as the signal increases. Comparing the sensor response to incident light on Figure 32, one can see that the non-linear model agrees better with the experimental data from the Phantom camera.

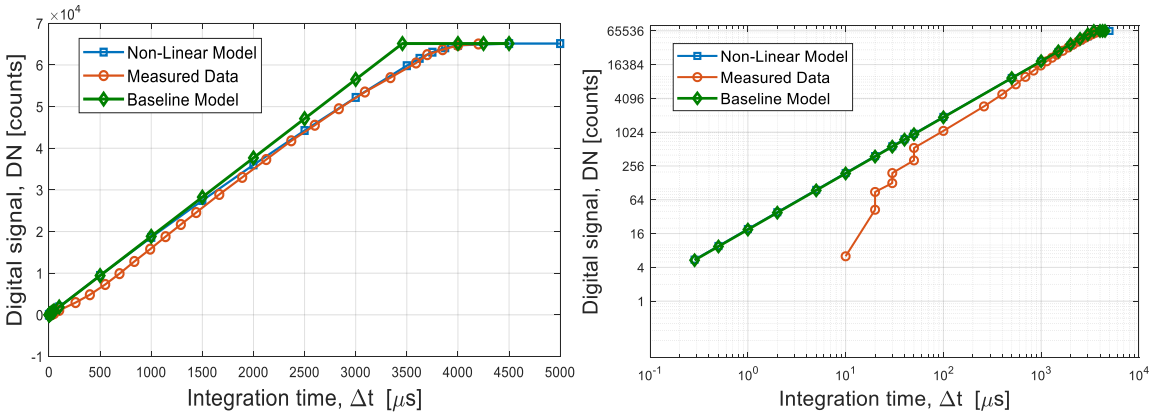

Figure 32. Sensor response to incident light for measured, baseline and non-linear models at several integration times spanning the full dynamic range for (left) linear and (right) logarithmic scales.

Although the modeled sensor response to incident light exhibits similar behavior to the Phantom v12.1, Figure 32 shows that the signal level is higher for the modeled sensor at low *integration times*. The model reproduces non-linear behavior at mid to high signals but fails to show non-linearity at low signal levels. Figure 33 shows the residual between the measured and modeled data for the baseline and non-linear. Measured data shows non-linearity at lower signal levels that is not accounted for in the model, possible due to

dark signal non-linearity at low signal levels. Such differences may also occur because the bias voltage (i.e. hardware offset) is not consistent throughout the experiment and may increase or decrease at lower integration times. Conversely, the sensor model uses a constant bias voltage for all integration times. Nonetheless, the behavior of the sensor model is consistent for most of the dynamic range. Comparing the error plots on Figure 33, one can see that the non-linear model agrees better with the experimental data as signal approaches full-well. Figure 33 also shows a maximum 92% reduction in error for the non-linear model.

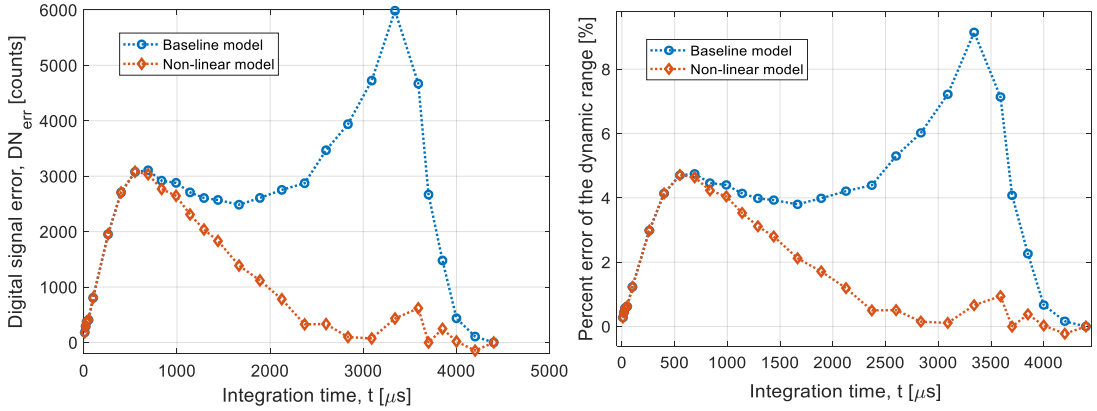

Figure 33. Signal error of the Sensor response to incident light for the baseline and non-linear model at several integration times spanning the full dynamic range for (right) the digital signal percent error of the dynamic range and (left) the signal error in counts.

Using the equations described in Chapter 4, PTCs are generated for $\sigma_{\text{total}}(DN)$, $\sigma_{\text{shot}}(DN)$, $\sigma_{\text{read}}(DN)$, and $\sigma_{\text{PRNU}}(DN)$ as a function of signal, $S(DN)$. From these plots, the conversion gain, *CG*, and the PRNU quality factor, P_N, were estimated. The methods used to generate the PTC measurements was the same for both the measured data and the sensor model. The PTC from the Phantom v12.1 is presented in Figure 34.

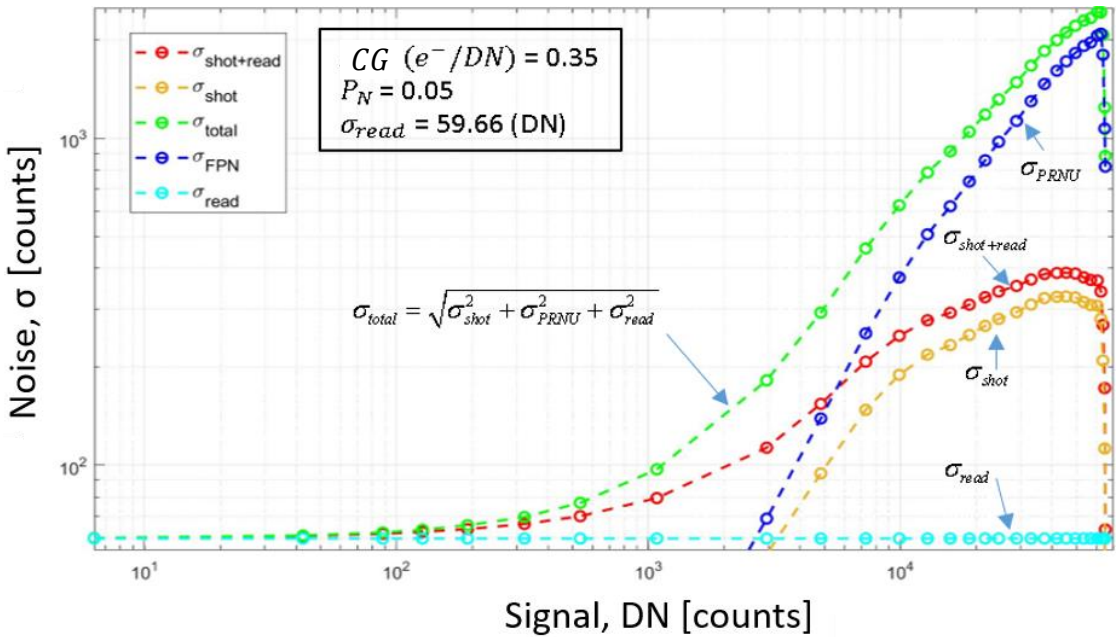

Figure 34. Experimental PTC plotted in counts of phantom v12.1. PTCs were generated for $\sigma_{total}(DN)$, $\sigma_{shot}(DN)$, $\sigma_{read}(DN)$, and $\sigma_{PRNU}(DN)$ as a function of signal, *S(DN)*. From these plots, the conversion gain, *CG*, and the PRNU quality factor, P_N, were estimated.

Although the PTC plot from the Phantom v12.1 exhibits a similar behavior compared to an ideal PTC (see Figure 27), one can note that the noise deviates from the one and one-half slopes as signal approaches full-well. This is explained by the fact that CMOS sensors exhibits non-linearity for high full-well performance. Using Equation (78), the conversion gain, CG, was estimated to be 0.35 electrons per count, which is consistent with the conversion gain provided by the manufacturer. However, this is only an estimation and is only true for low signals where non-linearity is negligible. In this system, the conversion gain varies from 0.35 [e/counts] for low signals to 0.79 [e/counts] at full-well. The PRNU quality factor, $P_N = 0.05$, was found using Equation (79).

Again using the method described in Chapter 4, PTCs were generated for $\sigma_{\text{total}}(DN)$ and $\sigma_{\text{shot+read}}(DN)$ as a function of signal for both the measured and

modeled data. Comparing the PTCs from the image sensor with the baseline and non-linear model in Figure 35, it is seen that the improved sensor model is consistent with the experimental data from the Phantom camera. Furthermore, signal noise as a function of digital count comparison in Figure 35 gives a qualitative estimate of the influence of non-linearity of the CMOS sensor. Comparing the PTCs in Figure 35, one can see that the non-linear model agrees better with the experimental data as signal approaches full-well. Figure 36 shows a noise error plot for the baseline and non-linear models for the total and shot plus read noise. For the non-linear model, in Figure 36, as signal approaches full-well, the total and shot plus read noise is reduced to 60% and 89%, respectively.

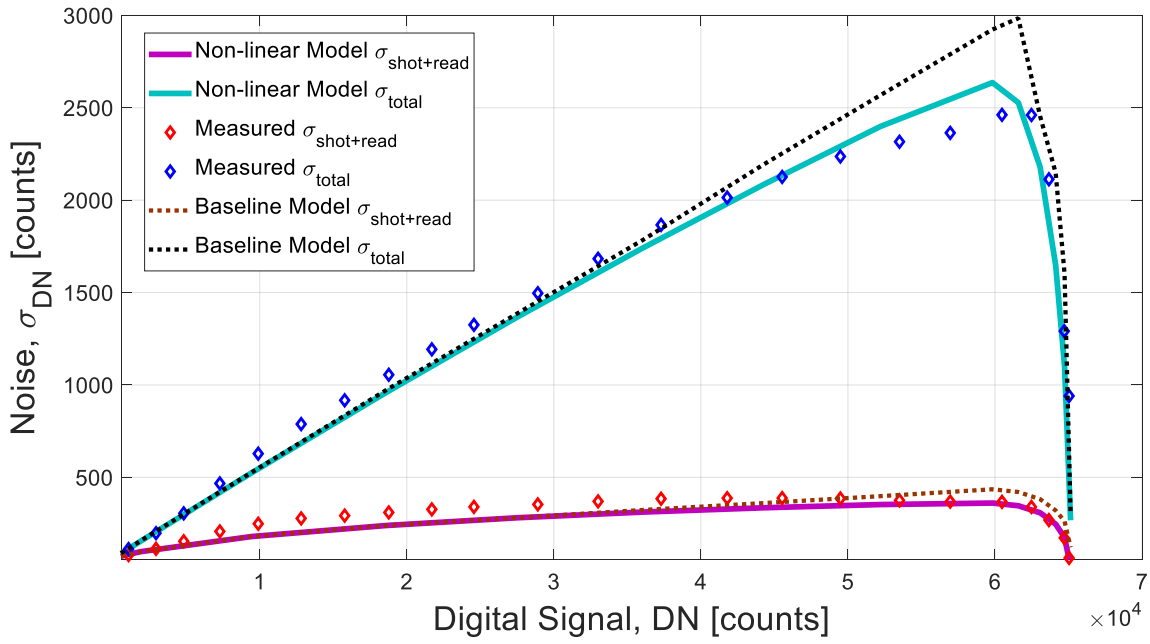

Figure 35. Photon transfer curves of Phantom v12.1 and the simulated sensor. RMS noise as a function of mean signal collected at several integration times spanning the full dynamic range.

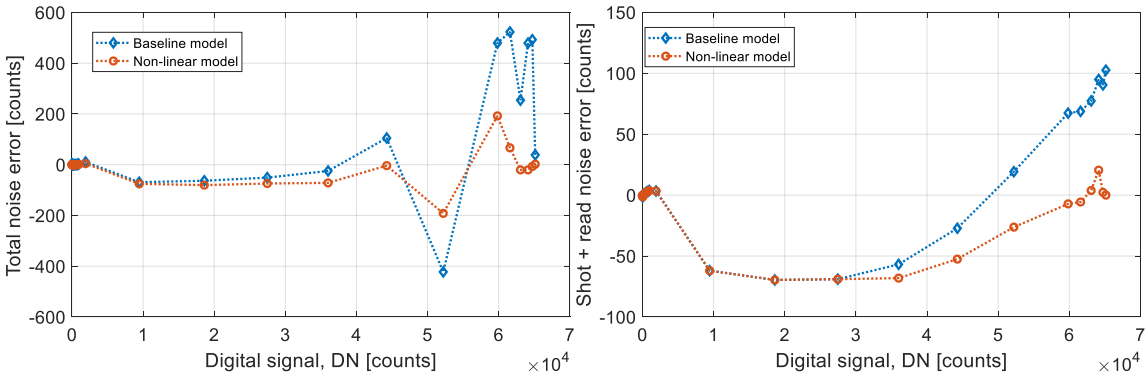

Figure 36. Noise error for the baseline and non-linear model at several integration times spanning the full dynamic range for (left) the total noise and (right) shot plus read noise in counts.

5.3 PRNU Validation

To obtain the experimental PRNU, we took 500 flat frames of 512x512 samples and averaged them to reduce the read noise and shot noise. The offset FPN, DSNU, and hardware offset were removed from the averaged flat frame values by subtracting pixel by pixel the averaged dark frame from the averaged flat frame. The resulting image only contains the PRNU noise. The method of PRNU measurements described above was the same for both the measured data and the sensor model.

For the simulated results a normal distribution was used to model the PRNU. The PRNU quality factor, P_N, was calculated using Equation (79) from the PTC. The integration time was the same for both the measured data and the model. Experimental results comparing the normal distribution to real data are shown in Figure 37, which shows a histogram of a normal distribution for both the measured and modeled data. Comparing the PRNU values from the image sensor and the modeled sensor model in Figure 37, it is shown that the sensor model is consistent with the experimental data from the Phantom v12.1.

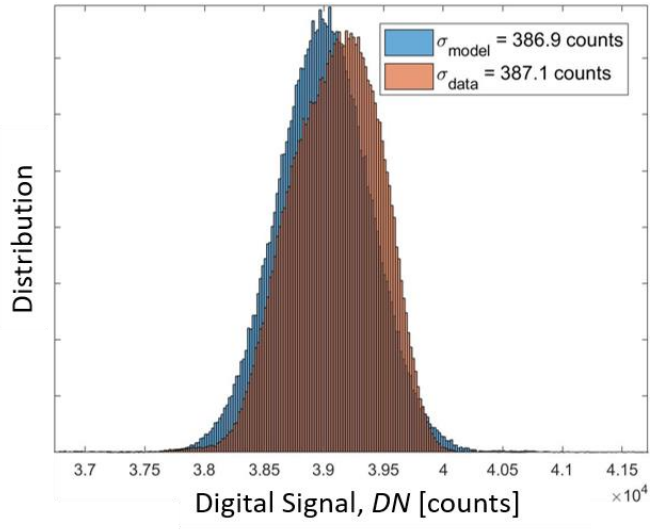

Figure 37. Measured and modeled PRNU noise levels for the integration time Δt = 15 ms seconds. Distributions of measured data and model dark frame pixels signal values have similar standard deviations: σ_{data} = 387.1 counts vs. σ_{model} = 386.9 counts.

5.4 Sensor Response in Dark Conditions and Dark Transfer Curve (DTC)

We generate 512x512 images using the parameters in Table 7 to compare our model with real measurements. The measured and modeled dark frames for the baseline and improved model are shown in Figure 38. The improved model uses a log-normal distribution for DSNU and an autoregressive process for the offset FPN (pixel, column, and ADC FPN), whereas the baseline model uses a normal distribution for DSNU and does not model the offset FPN. The figure clearly illustrates that the offset FPN introduced in the improved ASSET model better matches results of dark frames for CMOS sensors. Histograms of the measured and simulated images for the baseline and the improved model are shown in Figure 39. Even though the histogram for the baseline model also matches the histogram for the measured data, the image from the baseline model is not visually representative of real data due to differences in spatial distribution, and the offset FPN is needed to accurately model a CMOS sensor.

The measured dark frame shown in Figure 38 illustrates the effects present in CMOS sensors, such as the pixel and column offset FPN, and ADC offset FPN. Since it is difficult to separate FPN noise components, the three distributions are added in quadrature to form the total offset FPN, and the parameters were chosen to fit the data. For the DSNU, the log-normal distribution accounts for outliers (i.e. *hot pixels*) which generate much larger dark signal than the average mean value of the dark current. Combining DSNU and offset FPN results in the total FPN noise for the dark signal.

The image senor response to dark signal is calculated and compared to the sensor model output data. Covering the lens provides dark frames. The model uses an array of zeros to mimic the image sensor with the lens cap on (i.e. no input irradiance). Taking images over a range of integration times covers a fraction of the dynamic range of the photodetector. To reduce temporal noise (e.g. shot and read noise), we compute the mean dark frame at each integration time, obtaining the averaged dark frames. The averaged bias frame is subtracted from the dark frames to remove offsets such as offset FPN and the hardware offset. Subtracting the averaged bias frame from the dark frames yields the dark signal frames equivalent to the dark current in each pixel and frame, $D_{ijk}(DN)$.

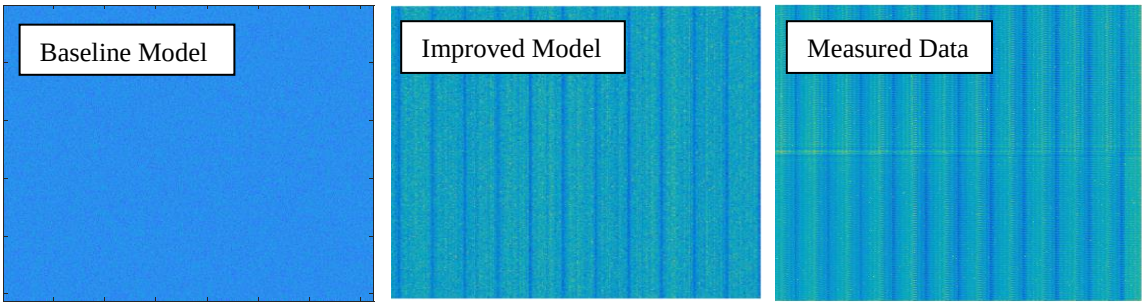

Figure 38. Comparison of a raw dark frame for the baseline model (left), the improved model (center) and the measured data (right) for integration time Δt = 30 ms.

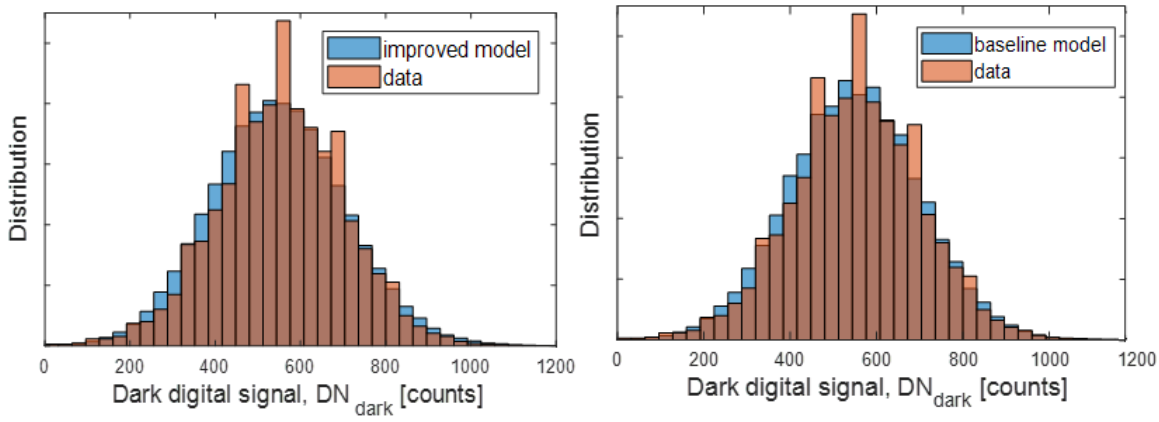

Figure 39. Distributions of measured and model data for the improved (left) and baseline (right) model have similar means: μ_{data} = 547.1 vs. $\mu_{improved}$ = 547.6 vs. $\mu_{baseline}$ = 547.5 counts; and standard deviations: σ_{data} = 151 vs. $\sigma_{improved}$ = 155 vs. $\sigma_{baseline}$ = 154 counts.

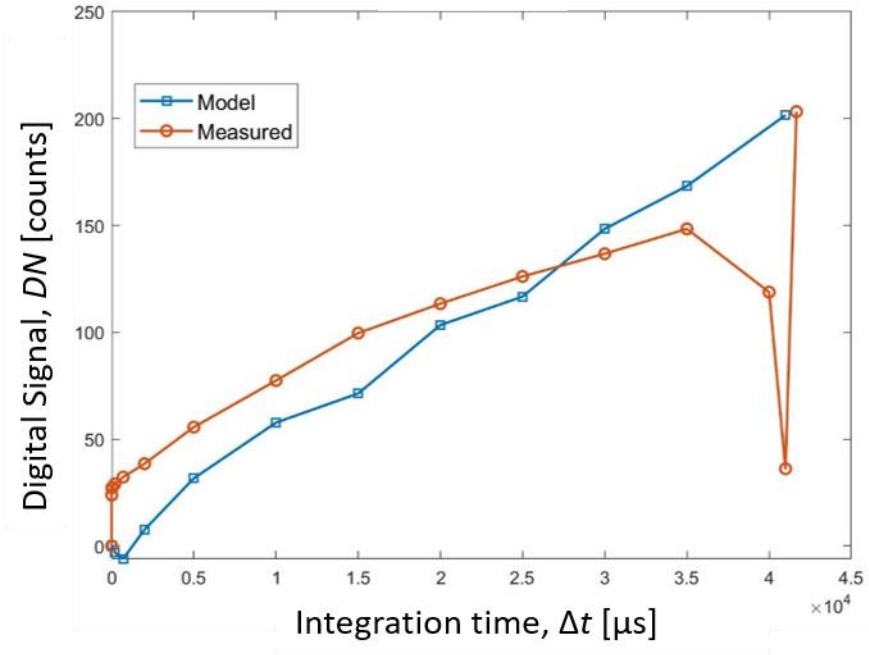

Figure 40. Sensor response in the dark for the measured and the modeled data at several integration times spanning a fraction of the dynamic range. When approaching the integration time limit of the Phantom (0.041 s at 24 frames per second) all data sets show some irregularities. This occurs in the figure, where the irregularities are visible at high integration times, around 41 ms.

The mean digital signal, *D(DN)*, of the resulting 512x512 pixels in the dark signal frames, $D_{ijk}(DN)$, is calculated and plotted for integration times spanning the full dynamic range (estimated to be 23,200 electrons). Figure 40 illustrates a comparison between the measured data and the simulated data of the sensor response in the dark.

The following discussion compares the results from the CMOS sensor and simulations for the non-linear model under dark conditions. The details of dark current, however, were not disclosed by the manufacturer. Therefore, the dark current and the noises associated with the dark signal were all estimated from the DTC plots obtained from the image sensor. Note that the DTC measurements shown below only cover a small part of the dynamic range. This is because a dark current of 774 e/s requires an integration time of at least 84 seconds to reach full-well (~23,200 electrons), while the camera is limited to a maximum integration time of 41 ms. At Δt = 41 ms, the sense node is only able to collect about 32 electrons from the dark signal, a fraction of the total dynamic range. Comparing the DTCs from the image sensor and the non-linear in Figure 41, one can see that the sensor model is generally consistent with the experimental data.

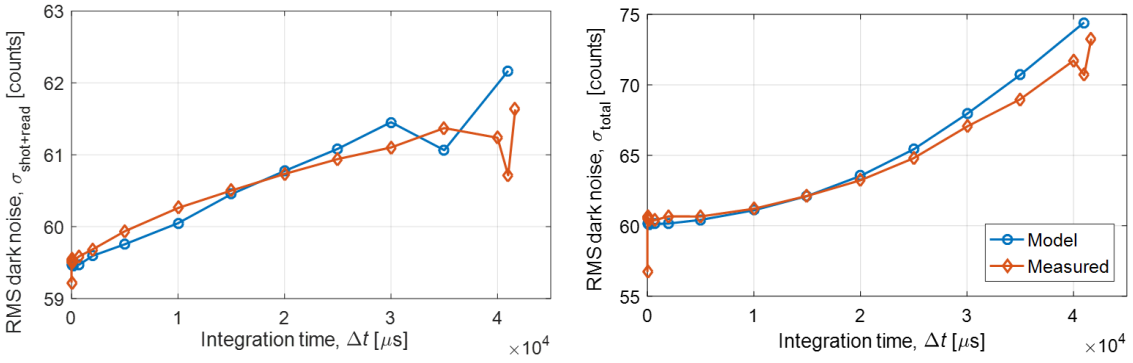

Figure 41. Dark Transfer Curves of CMOS sensor and the simulated sensor: (left) dark shot plus read noise, and (right) total dark noise. When approaching the integration time limit (0.041 s) both data sets show irregularities.

5.5 DSNU and Offset FPN Validation

In general, the FPN in the dark is divided into two categories. These categories are based on whether the FPN comes from the detector itself or the electronics in the circuit. These are DSNU and offset FPN. DSNU refers to an offset variation under dark conditions due to variations on the dark current from pixel-to-pixel. In CMOS sensors, in addition to DSNU, we have a pixel-to-pixel offset FPN due to threshold voltage differences between pixel's transistors in the sense node and source follower. Furthermore, variations in column amplifiers will cause a column-to-column offset FPN, which is very different to the noise we see in CCD sensors. Therefore, CMOS modeling requires an additional pixel-to-pixel and column-to-column offset FPN component that is not present in CCD sensors (see Section 3.6.3).

The top of Figure 42 shows a row of a raw dark frame before the offset FPN is removed from the image. The second graph is obtained from a 500 bias frame average to reduce the random noise by a factor of $500^{1/2}$. The offset FPN can now be seen more clearly since the averaging process reduces the random noise. The first and second graph are then subtracted to remove the offset FPN. The third graph is the result after the subtraction. The bottom graph is obtained from a 500 dark frame average after the offset FPN is removed from the image, which reduces the random noise leaving only the DSNU. One can note from the figure that the standard deviation of the offset FPN is much higher compared to the read, shot, and DSNU noise at low integration times.

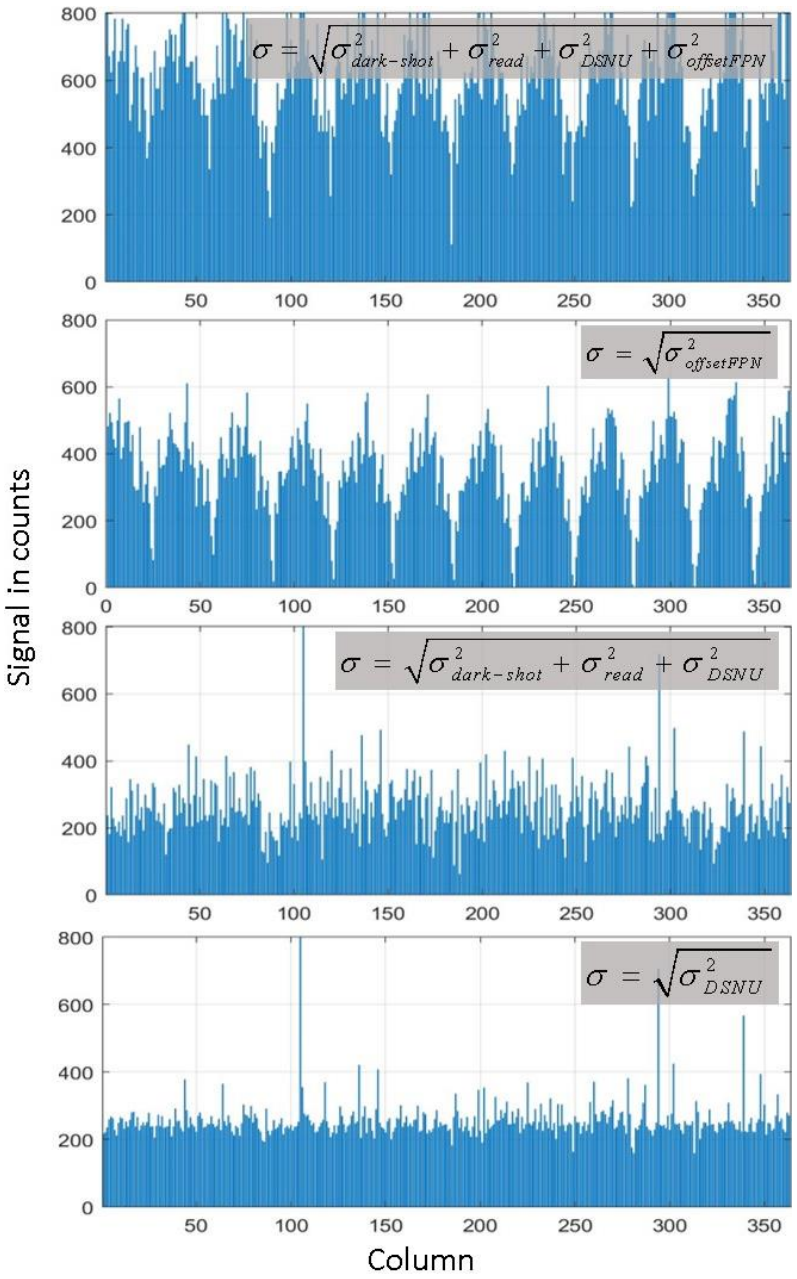

Figure 42. Phantom v12.1 array signal values (DN) for all columns of one row. From top to bottom: single dark frame at 30 ms integration time, average of 500 bias frames at 0.285 µs, difference between single dark frame and average bias frame, and average of 500 dark frames at 30 ms after offset FPN subtraction. Also shown are the associated RMS noise (σ) and its components. One can note from the figure that there are 32 columns periodic FPN present in the near-zero integration time offset (presumably due to differences in ADCs) whereas DSNU is relatively uniform across the column.

To obtain the experimental DSNU we took 500 dark frames of 512x512 samples and averaged them to reduce the read noise and shot noise. The hardware offset and offset FPN are removed from the dark frame values by subtracting pixel by pixel the averaged bias frame from the averaged dark frame. The resulting image will contain only the DSNU noise. The methods used to generate the DSNU measurements were the same for both the measured data and the sensor model. For the DSNU, the log-normal distribution accounts for outliers (i.e. hot pixels) which generate much larger dark signal than the average mean value of the dark current. Experimental results comparing the log-normal distribution to real data are shown in Figure 43. From the figure it is seen that the DSNU has only positive values and is positively skewed with a long tail (due to hot pixels).

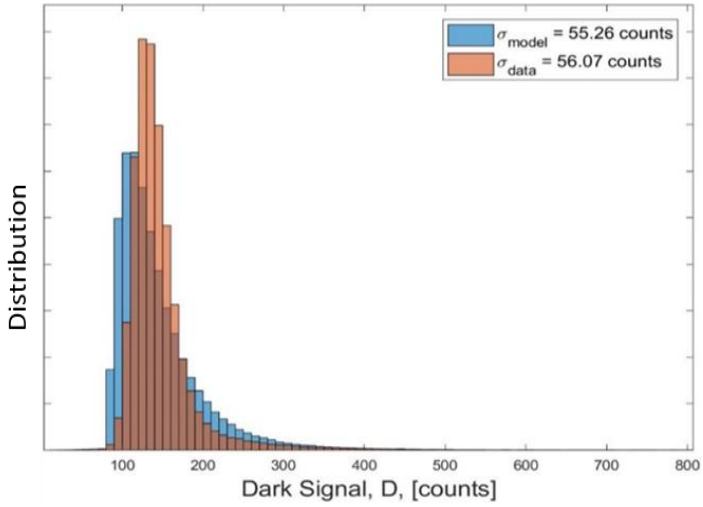

Figure 43. Comparison of measured and modeled DSNU noise levels for integration time Δt = 30 ms. Distributions of measured data and model dark frame pixels signal values have similar standard deviations: σ_{data} = 56.07 counts vs. σ_{model} = 56.07 counts.

To compare our model with the measured data we generated 512x512 pixels images using the model parameters in Table 7 for the baseline and improved model. For the baseline model a normal distribution was used to model DSNU, whereas for the

improved model, a log-normal distribution was used. A comparison of an averaged dark signal frame for the baseline model, the improved model, and the measured data is shown in Figure 44. The measurements presented in Figure 44 were also taken for integration times of 30 ms. The figure clearly illustrates the effects that are present in CMOS sensors such as the DSNU and hot pixels. The log-normal distribution describes the dark current FPN (DSNU) with good accuracy, as seen in Figure 44. Furthermore, the approximation of DSNU using a normal distribution is shown to be a poor estimate in the baseline model and does not account for hot pixels, rather the baseline used a randomly generated hot pixel mask that is not dependent on dark current.

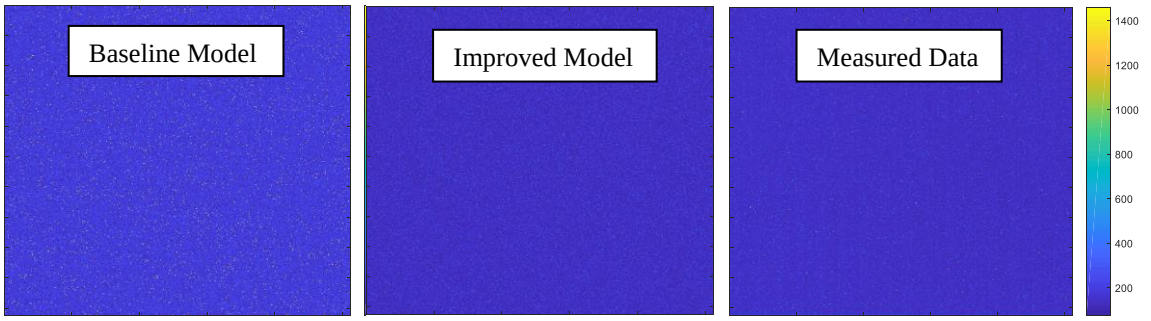

Figure 44. Comparison of an averaged dark signal frame for the baseline model with a normal distribution (left), the improved model with a log-normal distribution (center), and the measured (right) data for integration time Δt = 30 ms.

To obtain the experimental offset FPN, we took 500 bias frames of 512x512 samples and averaged them to reduce the read noise. To capture a bias frame, images need to be taken with zero integration time (or as close as possible) while covering the lens. When integration time is close to zero, the dark shot noise and DSNU components are negligible and the frames will only contain offset FPN and hardware offset. The methods used to generate the offset FPN measurements are the same for both the measured data

and the sensor model (both baseline and improved model). The offset FPN is modeled as a first order isotropic autoregressive process and is expressed as the sum of a column FPN component and a pixel FPN component (see Section 3.6.3). Furthermore, the image sensor from the Phantom camera employ a column-level ADC, where multiple ADCs operate in parallel and each share 32 columns. For this reason, an additional column offset FPN component is modeled that is associated with the sensor ADC circuit. The ADC offset FPN is also modeled as an autoregressive process but is only made of a column FPN component, which repeats every 32 columns.

The FPN offset (pixel, column, and ADC) statistical properties are also estimated for the CMOS sensor to confirm our assumption that the FPN offset can be modeled using a first order autoregressive process. However, it is difficult to distinguish between different offset FPNs (e.g. column and pixel) from the resulting images and PTC. The offset FPN factor is calculated according to $D_N^{FPN} = V_{fw}/\sigma_{FPN}$ and found to be $D_N^{FPN} = 0.0017$, where $D_N^{FPN}$is equivalent to the quadrature sum of the pixel (D_N^{pix}), column (D_N^{col}), and ADC (D_N^{ADC}) offset FPN factors. Figure 45 shows a histogram comparing the distribution of signal from measured and simulated images. As one can see in Figure 45, the offset FPN can be modeled as an autoregressive process with good accuracy.

From Figure 45 it is also evident that the averaged data bias frame and the averaged model bias frame has a pixel, a column, and an ADC offset FPN. One can see from the histogram that the approximation of offset FPN using an autoregressive normal process is consistent with the measured data. The measurements presented were taken for integration times of 0.285 µs, which is the smallest integration time possible in the Phantom camera. For integration times less than 1 µs, the DSNU and the shot noise are

less than one electron, and the output image will only contain read noise and offset FPN. By averaging multiple frames at the same integration time, the read noise is reduced and the offset FPN becomes more visible.

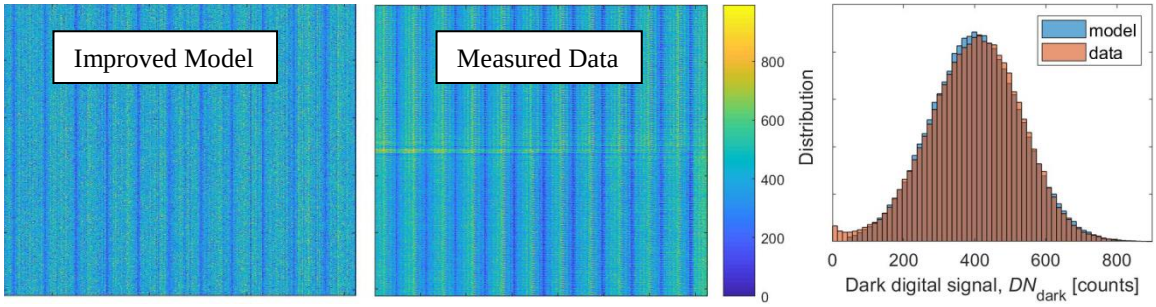

Figure 45. Comparison of an averaged dark frame for the (left) measured and (center) modeled data for integration time Δt = 0.285 μs and (right) distribution of measured and modeled dark frames. Distributions of measured data and model bias frame pixels signal values have similar means: μ_{data} = 399.94 counts vs. μ_{model} = 399.88 counts; and standard deviations: σ_{data} = 130.42 counts vs. σ_{model} = 131.61 counts.

5.6 Results Summary

Visual characteristics, signal, and noise distributions all demonstrate the ability of the improved ASSET model to produce data representative of real sensors in linear and non-linear conditions. In summary, the results presented in this section show that the improved ASSET model is consistent with the experimental data and can match single frames of the Phantom v12.1. Although the modeled sensor exhibits a similar behavior compared with the Phantom v12.1, one can observe from the data that the CMOS sensor simulation is generally inconsistent at low signal levels. Despite this limitation, ASSET is proven to be extremely useful in generating representative noise characteristics and visual effects of real hardware sensors.

6 Conclusion and Future Work

The models [5, 6] presented in this thesis were expanded for use on a larger variety of sensors. The described high-level CCD and CMOS sensor models were implemented in ASSET. The ASSET CMOS and CCD photodetector model output was tested against experimental results from hardware, showing agreement. The non-linearity introduced in the ASSET model better matches results of photon transfer curve (PTC) and dark transfer curve (DTC) estimations for CMOS sensors. Including the sense node and source follower non-linearity allows ASSET to better match the signal-dependent and time-varying properties of the Phantom v12.1. It was also demonstrated that the electronics FPN (e.g. pixel and column offset FPN) is often the limiting factor for CMOS sensors for low signal levels and has a more complicated distribution than previously discussed in the literature. This shows that ASSET can match single frames of the Phantom v12.1 under ideal and non-ideal (i.e. non-linear) conditions. Additionally, if provided with the relevant input sensor parameters, ASSET can emulate both spatially and temporally dependent sensor characteristics of CMOS hardware sensors (and presumably CCD, although not validated here), such as shot, read, and FPN as well as sensor non-linearity produced by the sense node and source follower.

The improved FPA model was developed as a component of the ASSET model and supports a large number of variables allowing a wide variety of sensors to be modeled. Although ASSET includes the ability to model scenes with realistic radiometric and optical properties, this paper focused on the process starting where photons arrive at the pixel array and through to the digital output, introducing many of the imperfections present in real systems, such as space-based sensors. This research provides an improved

ASSET model capable of generating realistic synthetic data, representative of a wide range of systems for use in algorithms supporting a broad community of academic, commercial, and military researchers.

Future development goals include: (1) improve correlated double sampling (CDS) algorithms, similar to the methods used in real systems that subtract dark images at zero integration time from signal images, eliminating offset FPN; (2) add alternative noise distributions for FPNs; and (3) add an analog to digital conversion (ADC) non-linear gain. Some time-intensive experiments using real data have been left for future work. As an example, the validation of a CCD sensor will show that ASSET can also simulate linear sensor response and FPN due only to DSNU and PRNU.

Appendix: ASSET Scene Radiance to Detector Photon Flux

This appendix provides a more detailed description of the calculations in ASSET not central to this research, i.e. scene radiometry, atmospheric effects, and the optical system.

A. Radiometry

The fundamental radiometric quantities are shown in Table 8. Radiance is the radiant flux emitted or reflected by a surface, per unit solid angle per unit projected area. In this text radiance implies integration over all wavelengths and spectral radiance is the radiance per unit wavelength. Flux or power is the amount of energy delivered per unit time and the amount of flux a source delivers per unit solid angle is called intensity. Both exitance and irradiance have units of power per unit area, but exitance is power exiting a surface and irradiance is the amount of power incident on a surface. Radiance incident on a surface can be described by three processes that occur in any material surface. These are spectral absorptance, $\alpha(\lambda)$, spectral reflectivity, $\rho(\lambda)$, and spectral transmissivity, $\tau(\lambda)$. The sum these three must equal one due to conservation of energy. Furthermore, since any material whose temperature is above 0 K emits heat, the emission of radiation must be considered. Spectral emittance, $\varepsilon(\lambda)$, is the ratio of emitted radiation (from surface) to that of a blackbody at the same temperature and is equal to the spectral absorptance, $\alpha(\lambda)$, for a material in thermal equilibrium.

Since the detectors emulated in ASSET respond directly to photons, the radiance values are converted to photon flux by multiplying the radiance at the detector with the throughput of the system $A\Omega$, where Ω is the solid angle subtended by the optics at the detector and A is the area of the detector.

Table 8. Fundamental Radiometric Units

Symbol	Quantity	Equation	Units
Q	Energy	Q	J
Φ^*	Flux	$\Phi = \frac{dQ}{dt}$	W
I	Intensity	$I = \frac{d\Phi}{d\Omega}$	W/sr
M	Exitance	$M = \frac{d\Phi}{dA}$	W/m^2
E	Irradiance	$E = \frac{d\Phi}{dA}$	W/m^2
L	Radiance	$L = \frac{d\Phi}{dA d\Omega} = \frac{dI}{dA}$	W/m^2-sr
* The conversion from Watts to photons/second is accomplished using the photon energy hc / λ			

A solid angle is an angle in a 3-D space defined as the area subtended by a surface projected onto a unit sphere at the center of the sphere, as illustrated in Figure 46. It is a measure of how large the object appears to be to an observer from the center of a sphere [1, 30]. A solid angle, Ω, has units of steradians [sr] and is the angle subtended at the center of a sphere by an area A on the surface of the sphere,

$$\Omega = \frac{A}{R^2} \quad [\text{sr}], \tag{95}$$

where A is the area on the surface of the sphere in squared meters and R is the radius of the sphere in meters. The maximum area on a spherical surface is $4\pi R^2$. Therefore, the maximum solid angle is given by $4\pi R^2 / R^2 = 4\pi$ [sr]. In addition, in a typical far-field imaging system, R is typically significantly larger than any dimension of A and the area on the surface can be assumed to be constant [1].

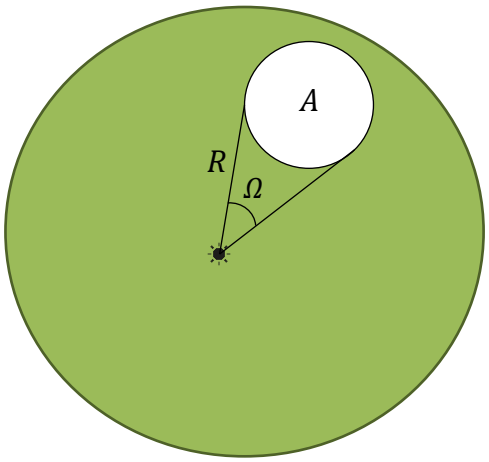

Figure 46. Solid angle. A solid angle, Ω, has units of steradians [sr] and is the angle subtended at the center of a sphere by an area A on the surface of the sphere.

Radiation from a source that is incident on a surface can be reflected in various ways depending on the characteristics of the surface [3]. In mirror-like surfaces, for example, reflectance occurs at the same angle to the surface normal as the incident angle but on the opposite side of the normal. In a Lambertian surface, radiance is independent of direction, and reflected (as well as emitted) radiance is equal in all directions; for a Lambertian surface, radiance is related to exitance (or irradiance) by

$$L = \frac{M}{\pi} \quad [\mathrm{W/m^2\text{-}sr}], \tag{96}$$

where M is the power per unit area exiting a surface. ASSET frequently uses Lambertian approximations to describe the angular distribution of radiance from the scene. A Lambertian source intensity is inversely proportional to the angle of observation and decreases as the angle moves away from the normal as shown in Figure 47. This change in intensity is compensated by an increase in the area perceived by the sensor so that the scene appears to have a constant radiance [1].

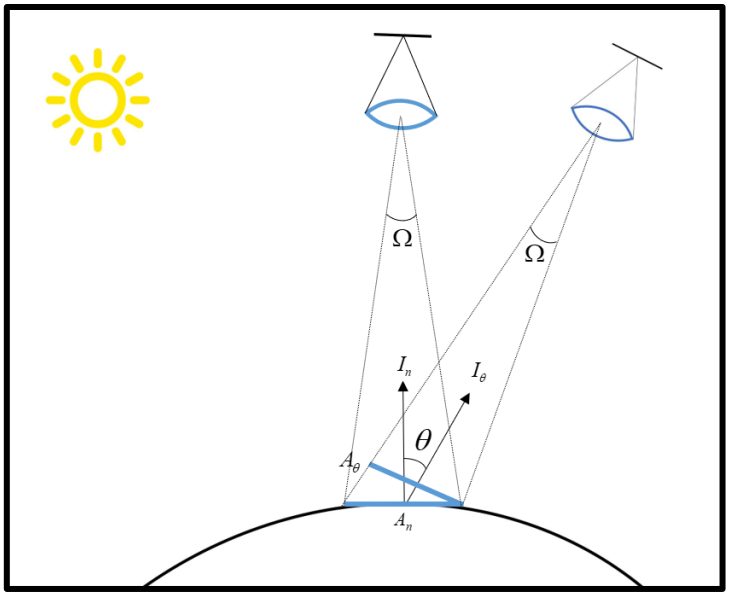

Figure 47. Lambertian scene. A Lambertian source intensity is inversely proportional to the angle of observation and decreases as the angle moves away from the normal. This change in intensity is compensated by an increase in the area perceived by the sensor so that the scene appears to have a constant radiance.

In ASSET, the throughput, also known as *etendue*, is used to convert from apparent photon radiance to photon flux falling on the detector and is given by

$$etendue = A\Omega \ [\text{m}^2\text{-sr}]. \tag{97}$$

Figure 48 illustrates the optical path for the case where the source fills the detector's field of view. A_{GSD} is the area of the detector projected to the plane of the source, A_{opt} is the area of the optics' aperture, A_{det} is the area of the detector, Ω_{GSD} is the solid angle subtended by A_{GSD} from the sensor, Ω_{optGSD} and Ω_{opt} are the solid angles subtended by the optics from the source and detector, respectively, and Ω_{det} is the solid angle subtended by the detector. For this case where the source fills the field of view of a detector, we have the following throughput relationship:

$$A_{GSD}\Omega_{optGSD} = A_{opt}\Omega_{GSD} = A_{opt}\Omega_{det} = A_{det}\Omega_{opt} \ \ [\text{m}^2\text{-sr}]. \tag{98}$$

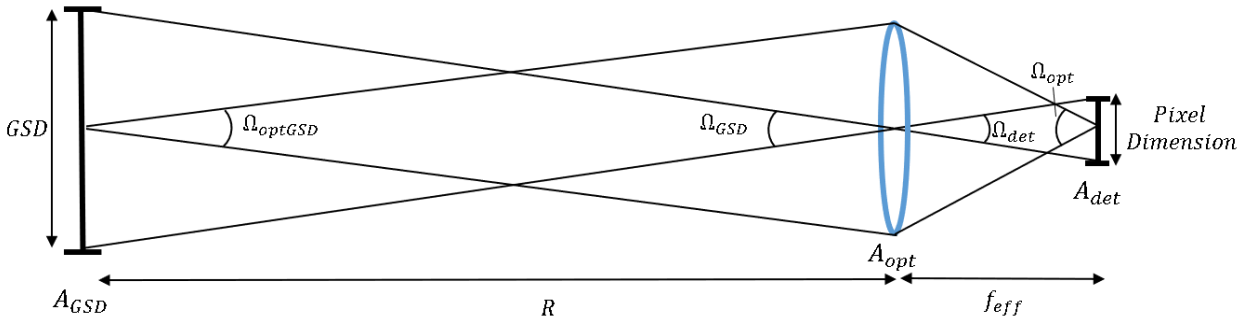

Figure 48. Optical path for the case where the source fills the detector's field of view. A_{GSD} is the area of the source in the detector's field of view, A_{opt} is the area of the optics' aperture, A_{det} is the area of the detector, Ω_{GSD} is the solid angle subtended by the source from the sensor, Ω_{optGSD} and Ω_{opt} are the solid angles subtended by the optics from the source and detector, respectively, and Ω_{det} is the solid angle subtended by the detector.

When choosing system parameters for calculation purposes it is practical to choose parameters that makes calculations easier. Since $A_{opt}\ \Omega_{det}$ and $A_{det}\ \Omega_{opt}$ products are easy to determine for any imaging system, either of these two pairs can be used for calculation purposes [30]. In ASSET the $A_{det}\ \Omega_{opt}$ product is used, as the detector size and optics are always constant.

Equation (1) in Section 2.1 shows the apparent spectral radiance as a function of wavelength in units of [ph/m^2-sr-μm] where emitted, reflected, and path radiance all contribute to the overall spectral radiance incident at the aperture. Given that a scene is viewed by a sensor within at a certain spectral bandwidth, the total radiance is computed in ASSET by integrating the spectral radiance over the band of interest. If the sensor is only responsive to certain wavelengths, which are usually specified by the sensor's relative spectral response (RSR) as shown in Figure 49, we can generally use the RSR as a weighting function and integrate from λ_1 to λ_2. The RSR is the overall relative spectral response of the system, $R(\lambda)$, peaked normalized to one.

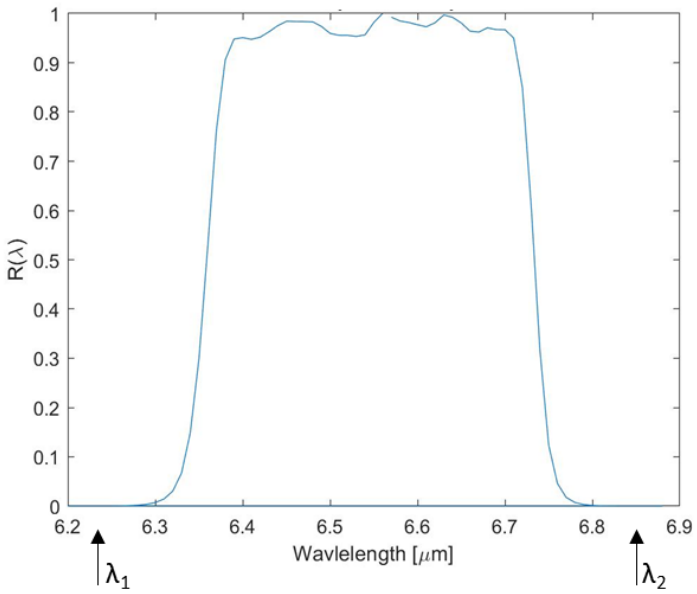

Figure 49. Example relative spectral response (RSR) of a system. The RSR represents the peak-normalized weighting of a system's response to photons as a function of wavelength which is assumed zero outside λ_1 to λ_2.

Assuming a Lambertian scene, the total band-integrated per-pixel emitted radiance measured by the detector is given by

$$L_{ems}^{det} = \tau_{sys} \int_{\lambda} \underbrace{\frac{\varepsilon(\lambda) M_{BB}(\lambda, T)}{\pi}}_{L_{ems}(\lambda, T)} \tau_{atm}^{sns}(\lambda) R(\lambda) d\lambda \quad \text{[photons / s-m}^2\text{-sr]}, \tag{99}$$

where ε(λ) is the spectral scene emissivity, $M_{BB}(\lambda, T)$ is the blackbody irradiance, $\tau_{atm}^{sns}(\lambda)$ is the atmospheric transmission from scene-to-sensor, $R(\lambda)$ is the relative spectral response of the system, and τ_{sys} is the peak transmission through the optical system; the product of τ_{sys} and $R(\lambda)$ represents the absolute, wavelength-dependent transmission through the system. Here, L_{ems}^{det} is the total emitted radiance at the detector and $L_{ems}(\lambda, T)$ is the spectral emitted radiance emitted from a scene at temperature T incident at the sensor's aperture.

Blackbody exitance, $M_{BB}(\lambda,T)$, is radiation emitted from a source with 100% emissivity at all wavelengths and is described by Planck's blackbody equation

$$M_{BB}(\lambda,T)=\frac{c_1}{\lambda^5\left[e^{\frac{c_2}{\lambda T}}-1\right]} \quad \text{[photons / s-m}^2\text{-μm]}, \tag{100}$$

where c_1 and c_2 are constants and T is temperature in Kelvin. Figure 50 shows the blackbody exitance as a function of wavelength at different temperatures.

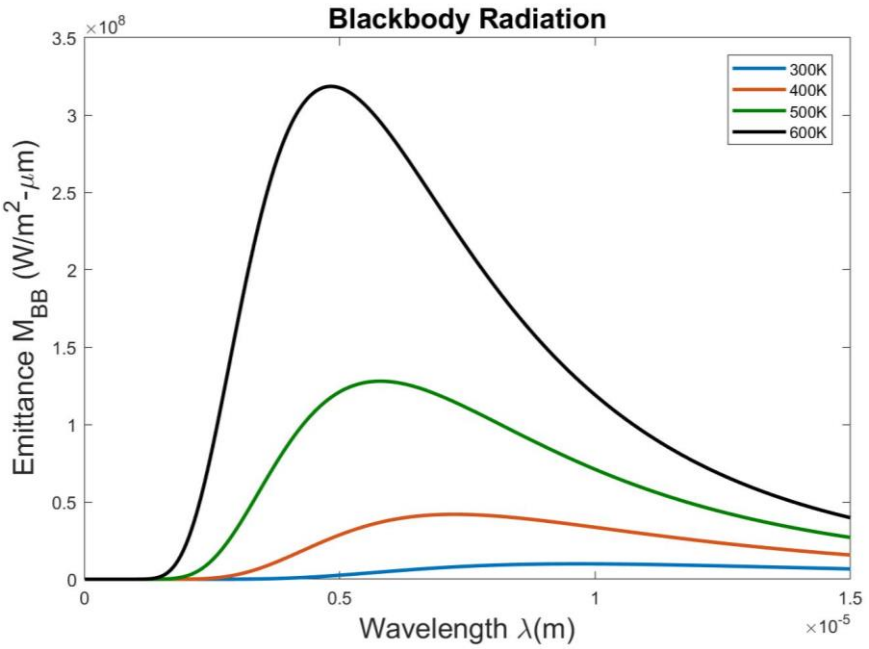

Figure 50. Spectral exitance of a perfect blackbody at several temperatures. Blackbody exitance, $M_{BB}(\lambda,T)$, is radiation emitted from a source with 100% emissivity at all wavelengths and is described by Planck's blackbody equation.

In the same manner, for a scene where all surfaces are treated as Lambertian, the band-integrated per-pixel reflected radiance measured by the detector is given by

$$L_{ref}^{det}=\tau_{sys}\int_{\lambda}\underbrace{\frac{\rho(\lambda)E_{TOA}(\lambda)\tau_{atm}^{sun}(\lambda)}{\pi}}_{L_{ref}(\lambda)}\tau_{atm}^{sns}(\lambda)R(\lambda)d\lambda \quad \text{[photons / s-m}^2\text{-sr]}, \tag{101}$$

where $\rho(\lambda)$ is the spectral scene reflectivity, $\tau_{atm}^{sun}(\lambda)$ is the atmospheric transmission from sun-to-scene, $\tau_{atm}^{sns}(\lambda)$ is the atmospheric transmission from scene-to-sensor, $R(\lambda)$ is the relative spectral response of the system, and $E_{TOA}(\lambda)$ is the seasonally-adjusted top of the atmosphere (TOA) solar irradiance for the user-specified scene location, date, and time of day [4]. The product $E_{TOA}(\lambda)\tau_{atm}^{sun}(\lambda)$ is sometimes grouped as one term and is expressed as the at-ground solar irradiance $E_{sol}(\lambda)$. L_{ref}^{det} is the reflected component of total radiance at the detector and $L_{ref}(\lambda)$ is the spectral reflected radiance at the sensor's aperture from Equation (1). The total per-pixel scene radiance measured by the detector within a spectral band is found using

$$L_{det}^{scene} = L_{ref}^{det} + L_{ems}^{det} + L_{pth}^{det} \quad \text{[photons / s-m}^2\text{-sr]}, \tag{102}$$

where L_{ref}^{det} is the total reflected radiance at the detector, L_{ems}^{det} is the total emitted radiance at the detector, and L_{path}^{det} is the total path radiance at the detector. Here, L_{det}^{scene} is the total apparent scene radiance at the detector and does not include self-emission, which will also contribute to the total radiance at the detector.

In ASSET, there are three different cases to generate scene radiance from source images. A brief description for each of these cases follows:

(1) The user may specify the bounds of scene radiance in units of [W/m^2-sr] in the configuration file (see Figure 51). Scene surface radiance is obtained by linearly scaling the source image to the minimum and maximum radiance bounds.

(2) The user may specify scene reflectivity (or emissivity) bounds in the configuration file (see Figure 51). Scene reflectivity (or emissivity) is obtained by linearly scaling the source image to the bounds specified in the configuration

file. These scene reflectivities and emissivities are used to later generate scene radiance as a combination of thermal emission and solar reflection as described in Equations (99) and (101).

(3) The user may specify reflectance, emissivity, and/or temperature maps which are used to generate scene radiance similarly to case (2), except in this case reflectivity, emissivity, and temperature may vary across the scene in a way that is not correlated with each other or with the source image. Figure 52 shows examples of emissivity and reflectivity maps used in ASSET.

For cases (2) and (3), scene radiance is computed using Equation (102) where $\tau_{atm}^{sns}(\lambda)$, $\tau_{atm}^{sun}(\lambda)$, L_{path}^{app} and $E_{sol}(\lambda)$ are obtained from a database generated using MODTRAN and based on a set of user-defined atmosphere options. If either reflectance or emissivity maps are not specified, the other can be obtained using the relation $\varepsilon(\lambda) + \rho(\lambda) = 1$ where ε(λ) is the emissivity and ρ(λ) is the reflectivity.

```
102 ; SOURCE OPTIONS
103 Rotate Image = FALSE
104 Crop Pixels = 0
105 Padding = 0
106 Sharpen Strength = 0
107 UseLandsat8 = FALSE
108 Sample Dimensions = [0.03,0.03]
109 Reflectivity = []
110 Emissivity = []
111 Radiance = [0 2]
112 Quantile = [0.001,0.999];
113 Sensor =
114 Initial Aimpoint = [0 0]
```

Figure 51. Source options in the ASSET configuration file. The user may specify the bounds of scene radiance (highlighted) in units of W/m^2-sr, emissivity, or reflectivity. The source image is scaled to the bounds and used to generate scene radiance.

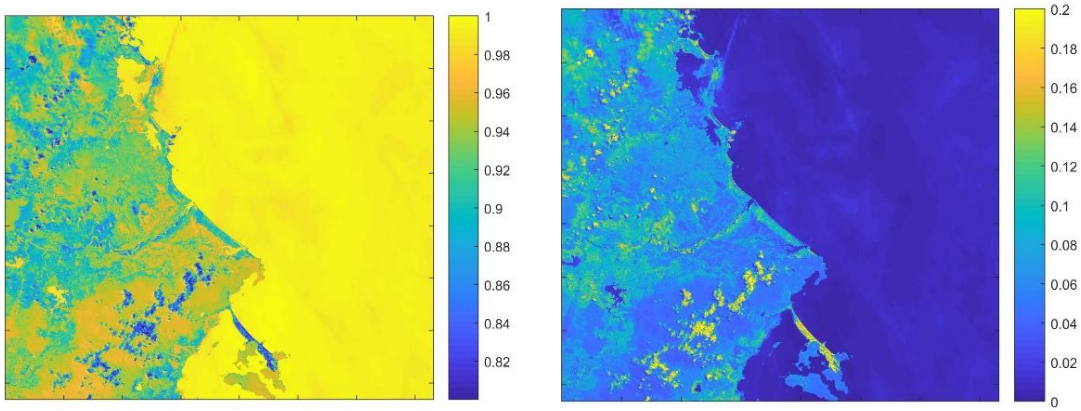

Figure 52. Examples of emissivity (left) and reflectivity (right) maps. If either reflectance or emissivity maps are not specified, the other can be obtained using the relation $\varepsilon(\lambda) + \rho(\lambda) = 1$ where $\varepsilon(\lambda)$ is the scene emissivity and $\rho(\lambda)$ is the scene reflectivity.

B. Atmospheric Effects

As radiation propagates through the atmosphere, some of the radiation is absorbed and scattered by the atmosphere resulting in reduced transmission. Both the absorption and scattering components are wavelength dependent [3, 1]. Figure 53 illustrates atmospheric transmission as a function of wavelength from the visible to the infrared spectrum.

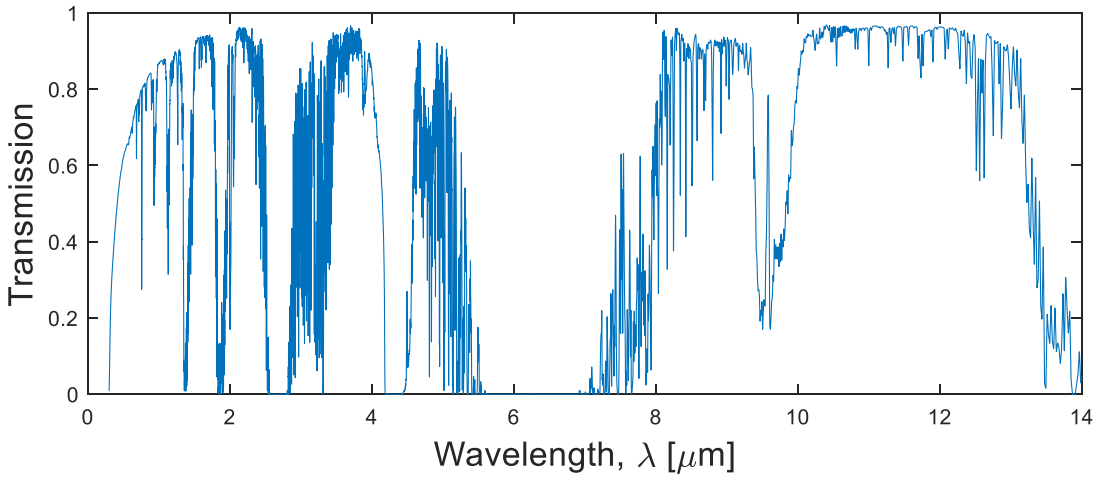

Figure 53. Wavelength dependent atmospheric transmission from the visible to infrared spectrum from ground to TOA looking straight up.

Detailed models are available that can be used to accurately model atmospheric effects for different conditions and scenarios. In ASSET atmospheric transmission, path radiance, and solar irradiance are obtained from a pre-computed database of MODTRAN standard atmospheres (Tropical, Mid-Latitude Summer, Mid-Latitude Winter, Sub-Arctic Summer, and Sub-Arctic Winter) for paths to the top of the atmosphere (TOA) sampled from a range of initial altitudes and elevation angles from 0 to 90 degrees. Paths from any (altitude, elevation) point to the top of the atmosphere are obtained by interpolating the database to the specified elevation and altitude values.

Path radiance is defined as radiance introduced by the path that contributes to the total flux on the detector and includes both the thermal radiation by atmospheric particles and radiation scattered into the optical path [1]. Currently in ASSET, path radiance only accounts for the thermal component, but future development will include an algorithm that accounts for the scattering component from sun and sky shine.

Currently there are four user-specified atmospheric options available in ASSET: ignore, uniform, scaled, and full atmosphere. *Ignore* atmosphere ignores all atmospheric effects. It is a case of *uniform* atmosphere, where both $\tau_{atm}^{sns}(\lambda)$ and $\tau_{atm}^{sun}(\lambda)$ are equal to one (therefore there is no atmospheric attenuation), and $L_{pth}(\lambda) = 0$ (i.e. no path radiance). This special case is only valid when either viewing outside the atmosphere or when the source image, clouds, and target signals already include atmospheric effects.

Both *uniform* and *scaled* atmosphere options start with a single atmospheric profile each for sun-to-scene and scene-to-sensor. These profiles are either user-provided files or obtained from the previously-described database based on the solar-scene-sensor geometry at the center of the scene. Figure 54 show an example of atmospheric profiles for a sun-scene-sensor geometry.

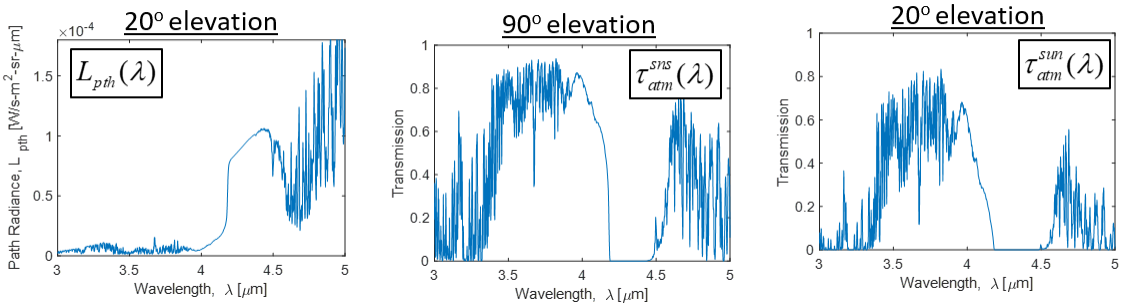

Figure 54. Examples of path radiance (left), scene-to-sensor transmission (middle), and sun-to-scene transmission (right) are shown as a function of wavelength.

Uniform atmosphere applies the sun-scene and scene-sensor atmospheric profiles across the entire scene so that atmospheric and solar quantities are constant. This is inaccurate for substantial changes in viewing geometry and therefore only valid when the atmosphere can be assumed to be the same across the scene (e.g. small FOV). The total radiance emitted and reflected within a spectral band measured by the detector are found using Equations (99) and (101), where $\tau_{atm}^{sns}(\lambda)$, $\tau_{atm}^{sun}(\lambda)$, and $E_{sol}(\lambda) = E_{TOA}(\lambda)\tau_{atm}^{sun}(T)$ are constant across the scene, or constant across all pixels; not to be confused with constant across all wavelengths. The total per pixel path radiance measured by the detector within a spectral band is found using

$$L_{pth}^{det} = \tau_{sys} \int_{\lambda} L_{pth}(\lambda) R(\lambda) d\lambda \quad \text{[photons / s-m}^2\text{-sr]}. \tag{103}$$

For a uniform atmosphere L_{pth}^{det} is used at every pixel, and the total per-pixel scene radiance measured by the detector within a spectral band is found using Equation (102).

In the case that a *scaled* atmosphere is specified by the user, a single atmospheric profile is used each for sun and sensor paths to the scene, and atmospheric and solar quantities across the scene are scaled from this *reference* path. The reference path is assumed to be the center of the scene at zero altitude, $z_0 = 0$, in the direction of the sensor (or sun) at elevation, θ_0. This case is accurate only for slight changes in altitude and elevation across the scene (i.e. accuracy decreases as deviation from the reference geometry increases) and scaling is only valid for near-surface targets, scenes with no clouds, and small FOV.

Figure 55 illustrates the scene geometry for a scaled atmosphere. In the figure, (z_i, θ_i) are the initial (original) altitude and elevation angle, (z_f, θ_f) are the final (scaled)

altitude and elevation angle, s is the distance from a point in the scene to sensor, and τ is the atmospheric transmission from a point in the scene to sensor (or sun). For the reference path, $\theta_i = \theta_0$ and $z_i = z_0 = 0$. The scaled atmospheric transmission from sun-to-scene and scene-to-sensor for every point in the scene (parameterized by z_f and θ_f) are related to the original atmospheric transmissions by

$$\tau_{atm}^{sun}(z_f, \theta_f, \lambda) = \tau_{atm}^{sun}(z_i, \theta_i, \lambda)^{\frac{\sin\theta_i}{\sin\theta_f} e^{(z_i - z_f)/z_s}} \tag{104}$$

and

$$\tau_{atm}^{sns}(z_f, \theta_f, \lambda) = \tau_{atm}^{sns}(z_i, \theta_i, \lambda)^{\frac{\sin\theta_i}{\sin\theta_f} e^{(z_i - z_f)/z_s}}, \tag{105}$$

respectively. These scaling relationships are based on the assumption of a plane parallel atmosphere and exponentially decreasing density with scale height z_s.

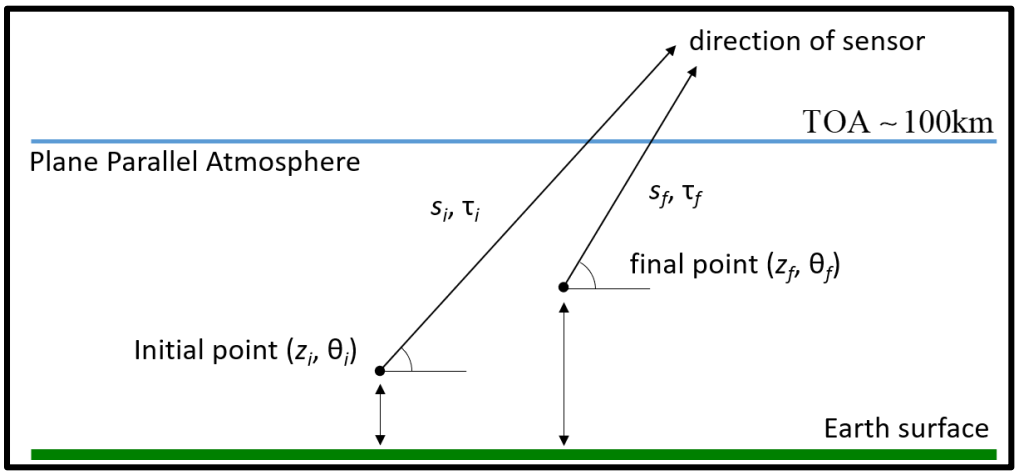

Figure 55. Scaled atmosphere scene geometry. In the figure, (z_i, θ_i) are the initial (original) altitude and elevation angle, (z_f, θ_f) are the final (scaled) altitude and elevation angle, s is the distance from a point in the scene to sensor, and τ is the atmospheric transmission from a point in the scene to sensor (or sun). For the reference path, $\theta_i = \theta_0$ and $z_i = z_0 = 0$.

The total surface emitted radiance within a spectral band for a scaled atmosphere is found by substituting Equation (105) into Equation (99),

$$L_{ems}^{det}(z_f,\theta_f)=\tau_{sys}\int_{\lambda}\frac{\varepsilon(\lambda)M_{BB}(\lambda,T)}{\pi}\tau_{atm}^{sns}(z_f,\theta_f,\lambda)R(\lambda)d\lambda \quad \text{[photons / s-m}^2\text{-sr]}, \qquad (106)$$

where $\tau_{atm}^{sun}(z_f,\theta_f,\lambda)$ is the scaled transmission from scene-to-sensor, z_f is the scaled altitude, and θ_f is the scaled elevation angle for each point in the scene. It should now be evident how the surface emitted radiance is scaled from *reference* path using a scaled atmospheric transmission.

The spectral solar irradiance is obtained by multiplying the TOA solar irradiance with the sun-to-scene atmospheric transmission given in Equation (104),

$$E_{sol}(z_f,\theta_f,\lambda)=E_{TOA}(\lambda)\tau_{atm}^{sun}(z_f,\theta_f,\lambda) \quad \text{[photons / s-m}^2\text{-μm]}. \qquad (107)$$

By substituting Equations (105) and (107) into Equation (101) the total band-integrated per-pixel radiance reflected by the scene is found,

$$L_{ref}^{det}(z_f,\theta_f)=\tau_{sys}\int_{\lambda}\frac{\rho(\lambda)E_{sol}(z_f,\theta_f,\lambda)}{\pi}\tau_{atm}^{sns}(z_f,\theta_f,\lambda)R(\lambda)d\lambda \quad \text{[photons / s-m}^2\text{-sr]}, \quad (108)$$

where $\tau_{atm}^{sns}(z_f,\theta_f,\lambda)$ and $E_{sol}(z_f,\theta_f,\lambda)$ are the scaled atmospheric transmission from scene-to-sensor and scaled solar irradiance at ground, respectively.

Finally, path radiance is scaled as the reciprocal ratio of emissivities (scaled to initial). Multiplying by emissivity ratio approximates small changes in path, replacing initial emissivity with scaled emissivity. The emissivity is defined by the relationship $\varepsilon(\lambda)=1-\tau(\lambda)$ where $\tau(\lambda)$ is the atmospheric transmission and $\varepsilon(\lambda)$ is the emissivity. Note that scattering has been ignored, which is generally a reasonable approximation in the MWIR and LWIR where thermal path radiance is most prominent. This emissivity-

transmission relationship is important to determine the total band-integrated per-pixel path radiance. Given the initial and scaled transmissions of the atmosphere, the scaled path radiance is described as

$$L_{pth}^{det}(z_f,\theta_f) = \tau_{sys}\int_{\lambda} L_{pth}(z_i,\theta_i,\lambda)\frac{1-\tau_{atm}^{sns}(z_f,\theta_f,\lambda)}{1-\tau_{atm}^{sns}(z_i,\theta_i,\lambda)}R(\lambda)d\lambda \quad \text{[photons / s-m}^2\text{-sr]}, \quad (109)$$

where $\tau_{atm}^{sns}(z_f,\theta_f,\lambda)$ and $\tau_{atm}^{sns}(z_i,\theta_i,\lambda)$ are the scaled and initial atmospheric transmissions and $L_{pth}(z_i,\theta_i,\lambda)$ is the initial spectral path radiance at the aperture. The total band-integrated per-pixel scene radiance measured at the detector for a scaled atmosphere is found using

$$L_{det}^{scene}(z_f,\theta_f) = L_{ref}^{det}(z_f,\theta_f) + L_{ems}^{det}(z_f,\theta_f) + L_{pth}^{det}(z_f,\theta_f) \quad \text{[photons / s-m}^2\text{-sr]}. \quad (110)$$

Figure 56 further illustrates how ASSET obtains the band-integrated path radiance, sun-to-scene atmospheric transmission, and scene-to-sensor atmospheric transmission across the scene for a scaled atmosphere. From this figure we see that path radiance and scene-to-sensor transmission are negatively correlated with each other; as path length from the sensor (for a sensor located directly above the center of the scene) increases, scene-to-sensor transmission decreases (towards the edge of the scene), and path radiance increases as expected. This is because thermal path radiance is a strong function of atmospheric transmission. We also see that both solar irradiance and sun-to-scene atmospheric transmission decrease as path length through the atmosphere in the direction of the sun (located to the top left corner of the scene) increases.

Full atmosphere, sometimes called *non-uniform* atmosphere in ASSET, is used when atmospheric and solar properties are calculated for all line of sight (LOS) paths from the sensor to scene points in order to obtain more accurate atmospheric effects across the scene. This is especially important for far off-nadir viewing geometries and WFOV scenes. If the user specifies the full atmosphere option, instead of using a single

atmosphere profile, ASSET returns $L_{pth}(\lambda)$, $\tau_{atm}^{sns}(\lambda)$, and $E_{sol}(\lambda)$ from its database and interpolates to altitude and elevation angle of each sample in the scene to obtain $L_{pth}(N,M,\lambda)$, $\tau_{atm}^{sns}(N,M,\lambda)$, and $E_{sol}(N,M,\lambda)$ as a function of wavelength, where (N,M) are sample indices of the source image. Note that in this case the sun-to-scene atmospheric transmission is not obtained as $E_{TOA}(\lambda)\tau_{atm}^{sun}(\lambda)$ because here $E_{sol}(\lambda)$ is obtained directly from the atmospheric database (this could have been done for uniform and scaled atmospheres too, but the database had not yet been implemented when those options were added to ASSET).

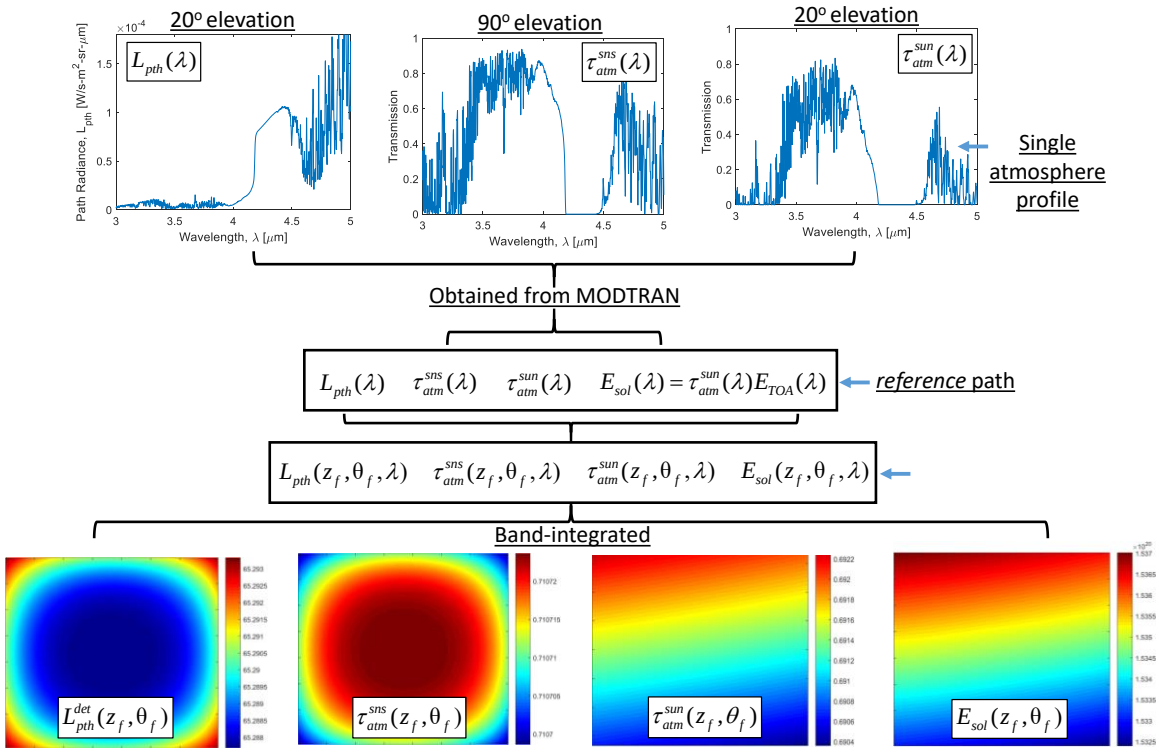

Figure 56. Diagram for path radiance, solar irradiance, and atmospheric transmission as a function of geometry for each pixel in the scene. Thermal path radiance and scene-to-sensor transmission are negatively correlated with each other; as path length from the sensor (located above the center of the scene) decreases, scene-to-sensor transmission increases, and path radiance decreases as expected.

Figure 57 shows a diagram on how ASSET obtains the band-integrated path radiance, atmospheric transmission, and solar irradiance across the scene for a non-uniform atmosphere as a function of sun-scene-sensor geometry. The figure depicts that the scene-to-sensor atmospheric transmission $\tau_{atm}^{sns}(N,M)$ and path radiance $L_{pth}(N,M)$ are negatively correlated to each other, and as path length from the sensor decreases (for a sensor located above the center of the scene), transmission decreases and path radiance increases towards the edges of the scene. Similarly, solar irradiance at each point in the scene decreases as the path through the atmosphere increases (i.e. smaller elevation angles) for the sun located in the direction of the upper left corner.

Unlike *uniform* and *scaled* atmospheres, the *full* atmosphere option cannot be obtained from a user-provided file and is instead obtained from ASSET's atmospheric database generated with MODTRAN. A full atmosphere is recommended for scenarios where atmospheric path and solar conditions vary significantly (e.g. WFOV) and where accurate scaling of target radiometry with altitude is needed. For a full atmosphere, the total band-integrated emitted and reflected radiance measured by the detector are found using Equations (99) and (101), where $\tau_{atm}^{sns}(\lambda)$, and $E_{sol}(\lambda)$ will vary across the scene as shown in Figure 57. The total per-pixel path radiance L_{pth}^{det} at the detector within a spectral band is found using Equation (103), and the total scene radiance at the detector is found using Equation (102).

In summary, both *uniform* and *scaled* atmosphere options use atmospheric profiles along paths to scene center, but for a scaled atmosphere the path radiance, solar irradiance, and atmospheric transmission are scaled from the reference profile to account for minor changes in sun-scene-sensor geometry. A more interesting comparison is

between *scaled* and *full* atmosphere options. Both are good approximations for small FOVs, as deviation from the reference path increases, accuracy rapidly decreases for a scaled atmosphere and a full atmosphere is recommended.

Figure 58 shows the total radiance at the detector for all atmospheric options. *Full* is considered truth (i.e. most correct). At first sight, measured radiance for the *ignore* and *uniform* cases look identical, but in the uniform case the magnitude is lower due to attenuation applied uniformly across the scene. *Scaled* and *full* atmospheres are also similar, but the decrease in transmission towards the lower right is exaggerated in the scaled scene.

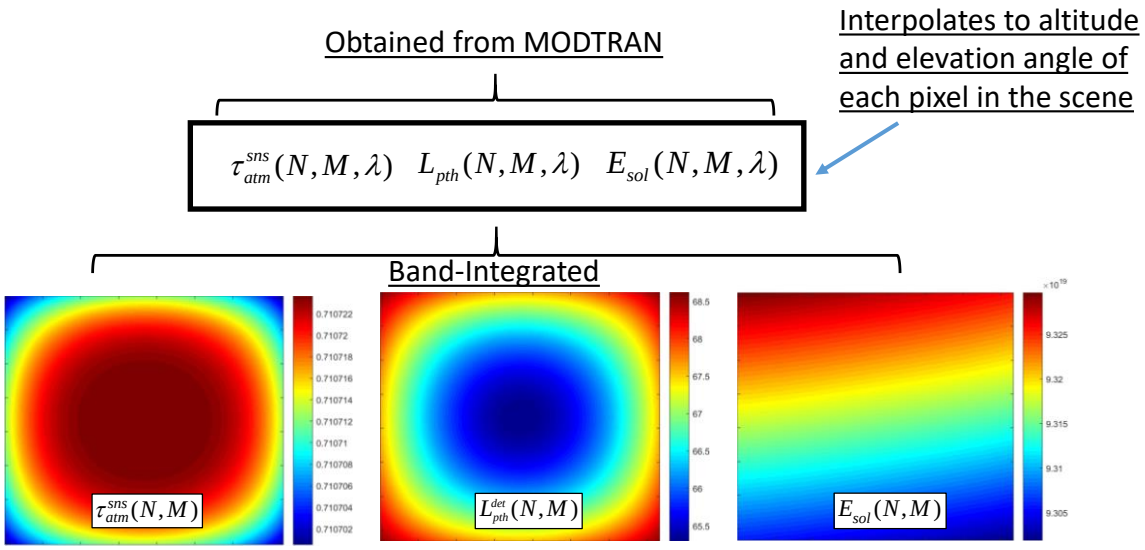

Figure 57. Diagram for path radiance, solar irradiance, and atmospheric transmission as a function of geometry for each pixel in the scene. Scene-to-sensor atmospheric transmission $\tau_{atm}^{sns}(N,M)$ and path radiance $L_{pth}(N,M)$ are negatively correlated to each other, and as path length from the sensor decreases (for a sensor located above the center of the scene), transmission increases and path radiance decreases. Similarly, solar irradiance at each point in the scene decreases as the path through the atmosphere increases (i.e. smaller elevation angles) for the sun located in the direction of the upper left corner.

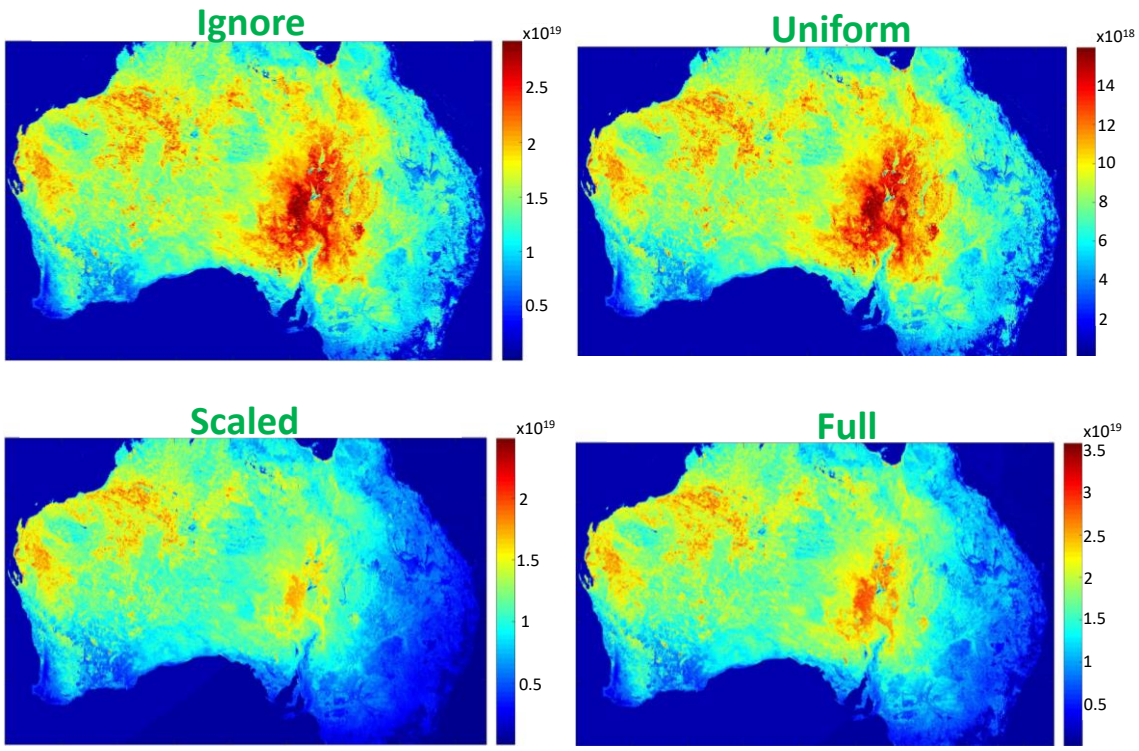

Figure 58. Radiance at the detector for all atmospheric options. *Full* is considered truth (i.e. most correct) because the atmospheric properties are calculated for all points in the scene. *Ignore* and *uniform* cases appear similar but differ in magnitude due to attenuation applied uniformly across the scene in the uniform case. *Scaled* and *full* also appear similar, but atmospheric effects towards the edge of the scene are exaggerated in the scaled case.

C. Optical System

To account for the imaging effects of the optical system, the point spread function (PSF) of the optics is convolved with the spatially resolved apparent spectral scene radiance, $L_{app}(X, Y, \lambda)$, where (X, Y) are horizontal and vertical coordinates in the detector plane. The PSF of an imaging system is the spatial impulse response of a system that accounts for diffraction (and potentially aberration) effects by the optics. The optical transfer function (OTF) of an imaging system is the Fourier transform of the PSF, and the modulation transfer function (MTF) is the absolute value of the OTF. In ASSET, the Fourier transform of the spatially resolved apparent radiance is computed and multiplied by the OTF. This is equivalent to a convolution with the PSF,

$$\begin{aligned} L_{det}^{PSF}(X,Y) &= L_{det}^{scene}(X,Y) \otimes h_{opt}(X,Y) \\ &= \tau_{sys} \int_{\lambda} \left[L_{app}(X,Y,\lambda) \otimes h_{opt}(X,Y) \right] R(\lambda) d\lambda \quad \text{[photons / s-m}^2\text{-sr]} \end{aligned} \tag{111}$$

where $h_{opt}(X,Y)$ is the PSF in the detector plane, $L_{det}^{scene}(X,Y)$ is the total scene radiance at the detector, $L_{app}(X,Y,\lambda)$ is the total apparent spectral radiance at the aperture (imaged into the detector plane), $R(\lambda)$ is the relative spectral response of the system, τ_{sys} is the peak transmission through the optical system, and $\otimes$ is the 2D spatial convolution operator. The baseline ASSET model currently uses the Gaussian function to approximate the PSF, but future development will allow the user to specify any arbitrary PSF or OTF directly [4].

At-aperture irradiance propagates through a sensor's optical system before reaching the detector array. Figure 60 depicts the optical components for an example optical system. Each of the lenses shown in the figure will attenuate the incoming radiation. In

addition, when self-emission is introduced after the first lens (L_{SE_1}) due to thermal emission from the first lens, the sum of self-emission and the attenuated at-aperture radiance $L_{app}\tau_{o1} + L_{SE_1}$ will then be attenuated by the second lens with transmission τ_{o2}.

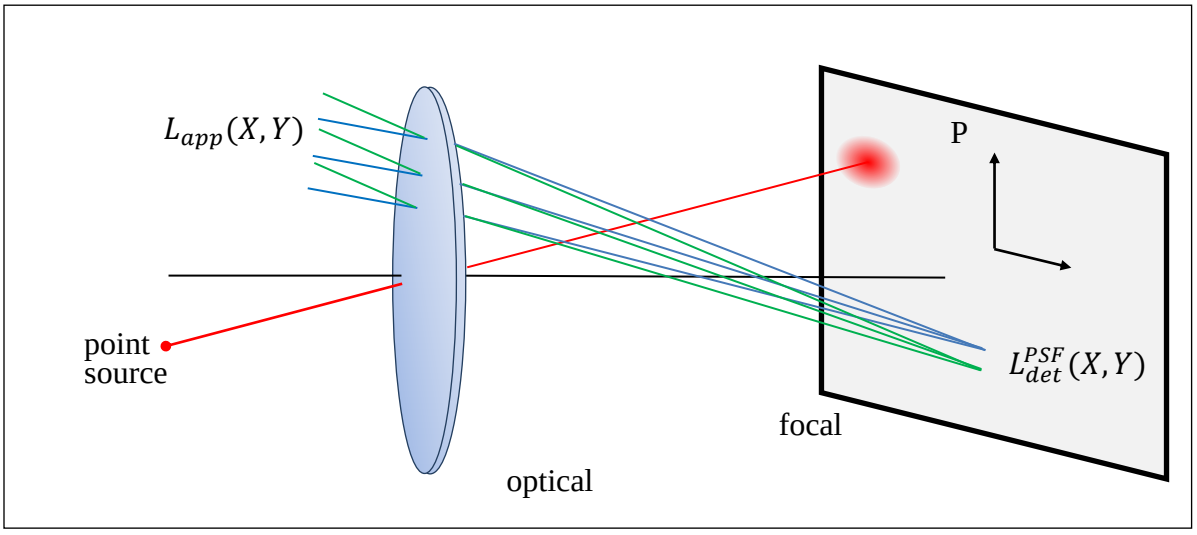

Figure 59. Radiometric quantities and geometries assumed in ASSET.

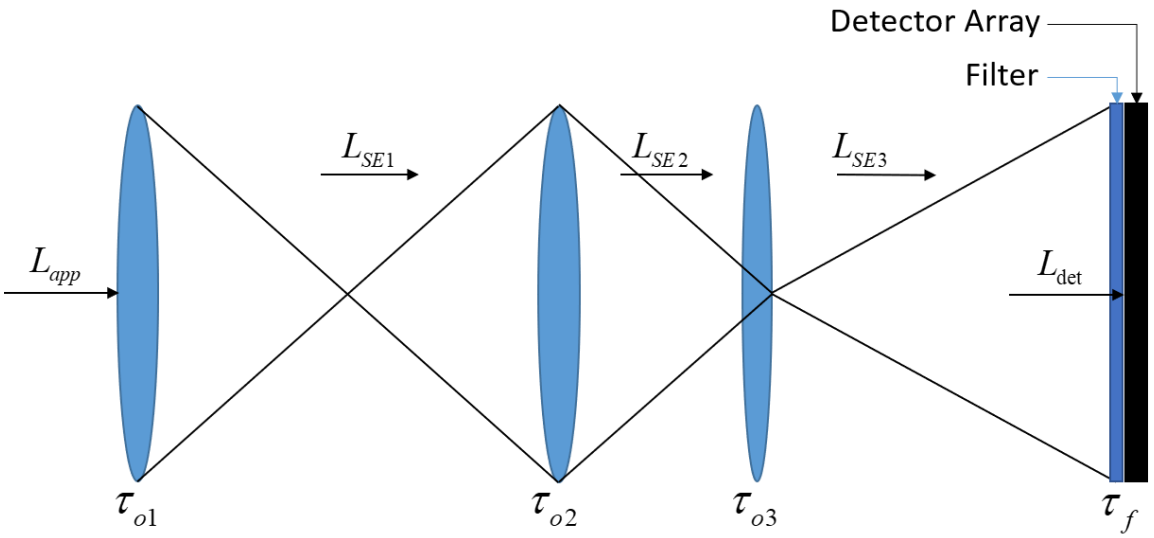

Figure 60. Optical system for an example imaging sensor. Each of the lenses shown in the figure will attenuate radiance passing through them as well as contribute thermal self-emission.

Furthermore, all radiation passing through the second lens (attenuated by τ_{o2}) plus its self-emission (L_{SE_2}) will be attenuated again by the subsequent optical components until it reaches the detector array. Self-emission for component *n* is computed as $L_{SE_n} = \varepsilon_n L_{BB}(T_n)$ where ε_n and T_n are the emissivity and temperature for the component *n*, respectively. The band-integrated radiance measured at the detector for the three-element optical system shown in Figure 60 is given by

$$L_{det} = \left(\left(\left(L_{app}\tau_{o1} + \overbrace{\varepsilon_1 L_{BB}(T_1)}^{L_{SE1}}\right)\tau_{o2} + \overbrace{\varepsilon_2 L_{BB}(T_2)}^{L_{SE2}}\right)\tau_{o3} + \overbrace{\varepsilon_3 L_{BB}(T_3)}^{L_{SE3}}\right)\tau_f \quad \text{[photons / s-m}^2\text{-sr]}, \quad (112)$$

where τ_{o_n} is the optical transmission of the *nth* component and τ_f is the filter transmission that is in front of the detector (note that this filter was not included in previous descriptions of the optical system). L_{app} is the at-aperture scene radiance and L_{det} is the total radiance at the detector including self-emission. If we assume uniform temperature across the optical path then $L_{BB}(T_1) = L_{BB}(T_2) = L_{BB}(T_3)$ and by expanding Equation (112) and grouping like terms we get:

$$L_{det} = L_{app}\tau_{o1}\tau_{o2}\tau_{o3}\tau_f + L_{BB}(T)(\varepsilon_1\tau_{o2}\tau_{o3}\tau_f + \varepsilon_2\tau_{o3}\tau_f + \varepsilon_3\tau_f) \quad \text{[photons / s-m}^2\text{-sr]}. \quad (113)$$

The first term represents scene radiance attenuated by all optical elements, and the second term is the total radiance emitted by the optical system that reaches the detector (assuming the optics to have zero reflectivity $\rho(\lambda) = 0$). If we simplify the equation using a change of variables $\tau_o = \tau_{o_1}\tau_{o_2}\tau_{o_3}$ and making use of conservation of energy, $\tau_o = 1 - \varepsilon_o$ (again with the assumption that the optics have zero reflectivity), we obtain

$$L_{\text{det}} = \tau_o \left(L_{app} \otimes h_{opt}(X,Y) \right) + L_{BB}(T)\varepsilon_o = L_{\text{det}}^{scene} + L_{SE} \quad \text{[photons / s-m}^2\text{-sr]}, \quad (114)$$

where L_{SE} is the overall self-emission that reaches the detector and τ_o is the net optical transmission through the system (expressed as $\tau_o(\lambda) = \tau_{sys} R(\lambda)$ in Section 2.1). The baseline ASSET model generates the spectral self-emission in the optical system as a Planckian at temperature *T* with emissivity ε_o which is then band-integrated to obtain the total self-emission as a function of focal plane coordinate (*X*,*Y*):

$$L_{SE}(X,Y) = \int_{\lambda} L_{SE}(X,Y,\lambda) d\lambda \quad \text{[photons / s-m}^2\text{-sr]}, \quad (115)$$

where $L_{SE}(X,Y,\lambda)$ is the spectral self-emission as a function of focal plane coordinate. The band-integrated radiance measured at the detector is therefore given by

$$L_{det}(X,Y) = L_{det}^{scene}(X,Y) + L_{SE}(X,Y) \quad \text{[photons / s-m}^2\text{-sr]}. \quad (116)$$

Note that Equations (112) and (113) neglected the PSF of each lens, and instead the net PSF of the system is used in Equation (114) to blur the scene radiance at the detector.

Since the detectors emulated in ASSET respond directly to photons, the total per-pixel radiance at the detector – from both scene and self-emission – is converted to photon flux. Throughput, $A\Omega$, also known as *etendue*, is used to convert from photon radiance to photon flux falling on the detector, where Ω is the solid angle subtended at the source by an area *A*. In ASSET, the $A_{det}\Omega_{opt}$ product is used, since the detector size and the solid angle subtended by the optics at the detector are nearly constant and easy to determine for any imaging system. Thus, the total photon-flux at the detector is given by

$$\phi_{det}(X,Y) = A_{det}\Omega_{opt} L_{det}(X,Y) \quad \text{[photons / s]}, \quad (117)$$

where Ω_{opt} is the solid angle subtended by the optics at the detector with area A_{det}.

In addition to the PSF, the detector response function (DRF), $h_{det}(X,Y)$, also affects the response of the sensor to spatially extended irradiance incident at the focal plane. The DRF represents the effects of spatial integration by the finite-size detectors, and in ASSET the DRF is a 2D rectangle function of normalized dimension *d*. Instead of being calculated directly, it is defined in ASSET as the Fourier transform of a 2D rectangle function, i.e. a 2D sinc function,

$$H_{det}\left(f_X, f_Y\right) = \Im\{h_{det}\left(X,Y\right)\} = \Im\left\{\text{rect}\left(X/d, Y/d\right)\right\} = d^2\,\text{sinc}(Xd, Yd), \tag{118}$$

representing the modulation transfer function (MTF) of a 2D rectangular pixel. The detector MTF is multiplied by the Fourier transform of the incident photon flux at the detector (which already includes convolution by the PSF to account for optical blurring), $P_{det}\left(f_X, f_Y\right) = \Im\left\{\phi_{det}\left(X,Y\right)\right\}$. This product is the frequency response of the detector array to the incident photon flux, and taking the inverse Fourier transform the frequency response results in an oversampled representation of the detected photon flux that includes blurring and spatial integration effects,

$$\phi_{det}^{over}(X,Y) = \Im^{-1}\left\{P_{det}(f_X, f_Y) \times H_{det}(f_X, f_Y)\right\} \text{ [photons / s].} \tag{119}$$

This is an oversampled representation of the photon flux at horizontal and vertical detector coordinates (*X*,*Y*), which is referred to in ASSET as the *oversampled array*. Figure 61 illustrates how the oversample array is obtained by convolving the incident photon flux with the DRF [31, 32].

The array $\phi_{det}^{over}(X,Y)$ is considered oversampled because every point (*X*,*Y*) represents the spatial summation of all photon flux over an area equal in size to a detector (due to convolution by the DRF). This oversampling is convenient because it provides the

photon flux as a function of sub-pixel coordinates across the scene. To obtain the photon flux in each pixel, $\phi_{det}(x,y)$, the array $\phi_{det}^{over}(X,Y)$ is sampled at the coordinates corresponding to pixel centers for all pixels in the FPA. Note that we have chosen the convention that (X,Y) are sub-pixel coordinates in the FPA and (x,y) are the subset of coordinates corresponding to pixel centers; (X,Y) is fixed but (x,y) may change from frame to frame as the focal plane move across the scene due to drift, jitter, or other pointing motion.

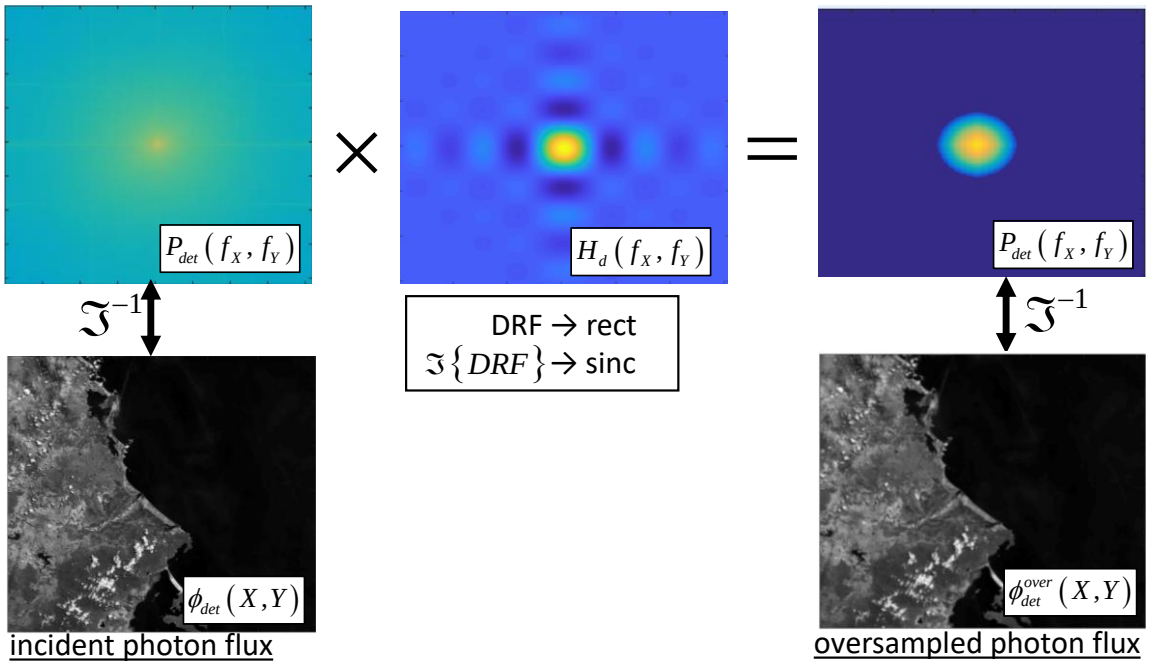

Figure 61. An example of the detector response function (DRF) used to obtain the oversampled photon flux. The Fourier Transform of the incident photon flux is multiplied by the detector MTF yielding the frequency response of the detector array to the incident flux. The inverse Fourier transform of this frequency response results in an oversampled representation that includes blurring and spatial integration effects.

Bibliography

[1] R. G. Driggers, M. H. Friedman and J. M. Nichols, Introduction to Infrared and Electro-Optical Systems, Boston: Artech House, 2013.

[2] S. R. Young, "Improving Detection of Dim Targets: Optimization of a Moment-Based Detection Algorith," Disseration, Air Force Institute of Technology, WPAFB, OH, 2018.

[3] S. C. Cain, Direct-Detection LADAR Systems, Washington: SPIE Press, 2010.

[4] S. R. Young, B. J. Steward and K. C. Gross, "Development and Validation of the AFIT Sensor and Scene Emulator for Testing (ASSET)," in *Proceedings of SPIE. 10178, 101780A*, Anaheim, CA, 2017.

[5] M. Konnik and J. Welsh, "High-Level Numerical Simulations of Noise in CCD and CMOS Photosensors: Review and Tutorial," in *arXiv:1412.4031 [astro-ph.IM] arXiv:1412.4031,* 2014.

[6] C. D. Willers and M. S. Willers, "Staring Array Sensor Model for Simulation Implementation," in *Proceeding of SPIE 10036, Fourth Conference on Sensors, MEMS, and Electro-Optic Systens*, Shukuza, Kruger National Park, South Africa, 2017.

[7] J. R. Janesick, Photon Transfer, Washington: SPIE Press, 2007.

[8] E. J. Ientilucci and S. D. Brown, "Advances in Wide-Area Hyperspectral Image Simulation," in *Proceedings of SPIE 5075, Targets and Backgrounds IX: Characterization and Representation*, Orlando, FL, 2003.

[9] B. J. Steward, *Instructor Notes, ASSET Legacy Brief, OENG 699,* Air Force Institute of Technology, WPAFB OH, 2018.

[10] J. E. Nelson, "Infrared Methods for Daylight Acquisitions of LEO Satellites," Thesis, Air Force Institute of Technology, 2004.

[11] G. C. Holst and T. S. Lomheim, CMOS/CCD Sensors and Camera Systems, Florida and Washington: JCD Publishing and SPIE Press, 2007.

[12] R. S. Wright, "An Astrophotographer's Gentle Introduction to Noise," SKY & Telescope, 15 April 2018. [Online]. Available: http://www.skyandtelescope.com/astronomy-blogs/imaging-foundations-richard-wright/astrophotography-gentle-introduction-noise/. [Accessed 1 06 2018].

[13] E. L. Dereniak and G. D. Boreman, Infrared Detectors and Systems, New York: John Wiley & Sons, 1996.

[14] A. M. Catarius, "Static Scene Statistical Non-Uniformity Correction," Thesis, Air Force Institute of Technology, WPAFB, OH, 2015.

[15] J. Otha, Smart CMOS Image Sensors and Applications, Boca Raton, FL: CRC Press, 2008.

[16] Z. Mei, N. Chen and L.-b. Yao, "Analysis of Pixel Circuits in CMOS Image Sensors," in *Proceeding of SPIE 9522, Selected Papers from Conferences of the Photoelectronic Thechnology Committee of the Chinese Society of Astronautics*, China, 2014.

[17] P. Megan, "Detection of visible photons in CCD and CMOS: A comparative view," *Nuclear Instruments and Methods in Physics Reasearch,* vol. 504, no. Section A: Accelerators, Spectrometers, Detectors and Associated Equipment, pp. 199-212, 2003.

[18] B. Sapoval and C. Herman, Physics of Semiconductors, New York: Springer-Verlag, 1995.

[19] A. El Gamal, B. Fowler, H. Min and X. Liu, "Modeling and Estimation of FPN Components in CMOS Image Sensors," in *Proceeding of SPIE. 3301, Solid State Sensor Arrays: Development and Applications II,* 1998.

[20] H. Tian, "Noise Analysis in CMOS Image Sensors," Dissertation, Stanford University, Stanford, CA, 2000.

[21] J. Nakamura, Image Sensors and Signal Processing for Digital Still Cameras, Boca Raton, FL: CRC Press, 2016.

[22] R. Crisp, "Introduction to CCD and CMOS Imaging Sensors and Applications," SPIE Short Course SC504, Lecture Notes, 2018.

[23] L. M. Simms, "Hybrid CMOS SIPIN Detectors as Astronomical Imagers," Dissertation, Standford University, Standford, CA, 2009.

[24] K. M. Yap, "Gain and Offset Error Correction for CMOS Image Sensors Using Delta-Sigma Modulation," Thesis, Boise State University, Boise, ID, 2010.

[25] C. A. de Moraes Cruz, "Simplified Wide Dynamic Range CMOS Image Sensor with 3T APS Reset-Drain Actuation," Dissertation, Universide Federal de Minas Gerais, Brazil, 2014.

[26] Y. M. Wang, H. Wang and T.-C. Kim, "Reset Noise Reduction for Pixel Readout with Pseudo Correlated Double Sampling". USA Patent US20150036035A1, 02 04 2014.

[27] M. F. Snoeij, A. J. P. Theuwissen, K. A. A. Makinwa and J. H. Huijsing, "A CMOS Imager With Column-Level ADC Using Dynamic Column Fixed-Pattern Noise Reduction," *IEEE Journal of Solid-State Circuits,* vol. VOL. 41, no. NO. 12, pp. 3007-3015, 2006.

[28] J. Jablonski, C. Durell, B. Schulman and K. Clifford, "Vision Systems," 1 January 2005. [Online]. Available: ttps://www.vision-systems.com/articles/print/volume-10/issue-1/features/component-integration-integrating-spheres-calibrate-sensors.html. [Accessed 13 October 2018].

[29] D. Gardner, "Characterizing Digital Cameras with the Photon Transfer Curve," Summit Imaging.

[30] J. M. Palmer and B. G. Grant, The Art of Radiometry, Washington: SPIE Press, 2010.

[31] B. J. Steward, *Instructor Notes, ASSET Legacy Brief, OENG 699,* Air Force Institute of Technology, WPAFB OH, 2018.

[32] S. C. Cain, "Instructor Notes - Introduction to LiDAR," Air Force Institute of Technology, 2018.

REPORT DOCUMENTATION PAGE

Form Approved
OMB No. 074-0188

PLEASE DO NOT RETURN YOUR FORM TO THE ABOVE ADDRESS.

1. REPORT DATE *(DD-MM-YYYY)*	**2. REPORT TYPE**	**3. DATES COVERED** *(From – To)*
21-03-2019	Master's Thesis	October 2017 – March 2019

TITLE AND SUBTITLE

A Focal Plane Array and Electronics Model for CMOS And CCD Sensors in the AFIT Sensor and Scene Emulation Tool (ASSET)

5a. CONTRACT NUMBER

5b. GRANT NUMBER

5c. PROGRAM ELEMENT NUMBER

6. AUTHOR(S)

Fernandez, Fernando D., Civilian, USAF

5d. PROJECT NUMBER

5e. TASK NUMBER

5f. WORK UNIT NUMBER

7. PERFORMING ORGANIZATION NAMES(S) AND ADDRESS(S)

Air Force Institute of Technology
Graduate School of Engineering and Management (AFIT/ENG)
2950 Hobson Way, Building 640
WPAFB OH 45433-8865

8. PERFORMING ORGANIZATION REPORT NUMBER

AFIT-ENG-MS-19-M-026

9. SPONSORING/MONITORING AGENCY NAME(S) AND ADDRESS(ES)

Space and Missile Systems Center, Remote Sensing Exploitation Division
483 North Aviation Blvd, El Segundo, CA 90245
ATTN: 2Lt Lei Zhu, lei.zhu@us.af.mil, 310-653-4707

10. SPONSOR/MONITOR'S ACRONYM(S)

SMC/RSX

11. SPONSOR/MONITOR'S REPORT NUMBER(S)

12. DISTRIBUTION/AVAILABILITY STATEMENT

DISTRUBTION STATEMENT A. APPROVED FOR PUBLIC RELEASE; DISTRIBUTION UNLIMITED.

13. SUPPLEMENTARY NOTES

14. ABSTRACT

Electro-optical and infrared (EO/IR) sensor models are useful tools that can facilitate understanding a system's behavior without expensive and time-consuming testing of an actual system. EO/IR models are especially important where truth data is required but is sometimes impractical to obtain through experimentation due to expense or difficulties in procuring hardware. This work describes implementation of a focal plane array (FPA) model of CCD and CMOS photodetectors as a component in the AFIT Sensor and Scene Emulation Tool (ASSET). The FPA model covers conversion of photo-generated electrons to voltage and then to digital numbers. It incorporates sense node, source follower, and analog-to-digital converter (ADC) components contributing to gain non-linearities and includes noise sources associated with the detector and electronics such as shot, thermal, 1/f, and quantization noise. This thesis describes the higher fidelity FPA and electronics model recently incorporated into ASSET, and it also details validation of the improved model using EO/IR imager data collected with laboratory measurements. The result is an improved model capable of generating realistic synthetic data representative of a wide range of systems for use in new algorithm development and data exploitation techniques supporting a broad community of academic, commercial, and military researchers.

15. SUBJECT TERMS

FPA model, electro-optical, infrared, detector, ASSET, sensor model, non-linearity, FPN

16. SECURITY CLASSIFICATION OF:			**17. LIMITATION OF ABSTRACT**	**18. NUMBER OF PAGES**	**19a. NAME OF RESPONSIBLE PERSON**
a. REPORT	**b. ABSTRACT**	**c. THIS PAGE**			Dr. Bryan Steward, AFIT/ENP
U	**U**	**U**	**UU**	153	**19b. TELEPHONE NUMBER** *(Include area code)* 937-255-3636 x4639 Bryan.Steward@afit.edu

Standard Form 298 (Rev. 8-98)
Prescribed by ANSI Std. Z39-18